UNIVERSITÄT BAYREUTH

DISSERTATION

Experiments on Granular Monolayers — Tuning Shape, Interaction and Analysis

SIMEON VÖLKEL

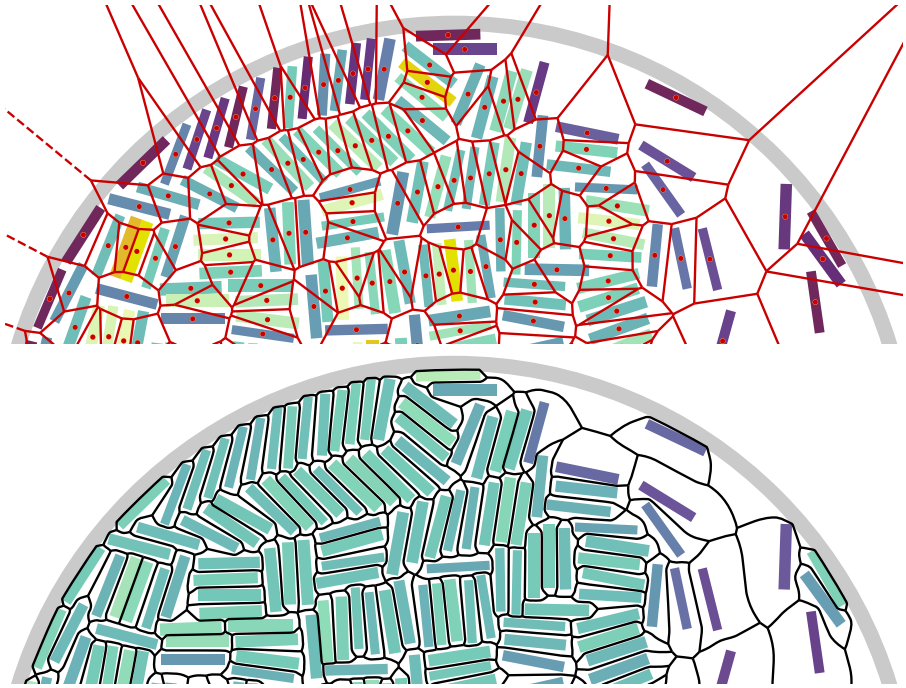

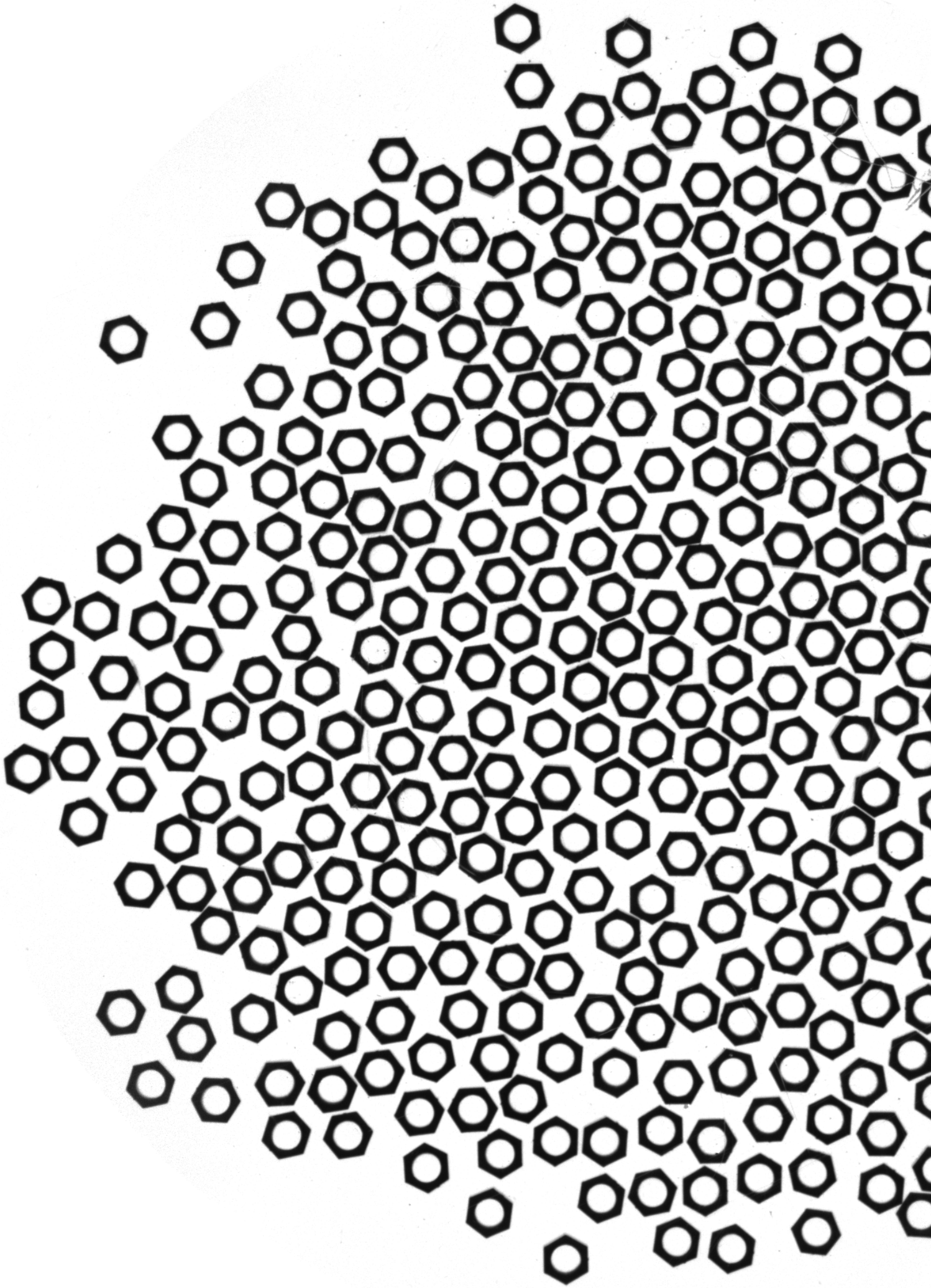

Experiments on Granular Monolayers — Tuning Shape, Interaction and Analysis

Von der Universität Bayreuth
zur Erlangung des Grades eines
Doktors der Naturwissenschaften (Dr. rer. nat.)
genehmigte Abhandlung

von

SIMEON VÖLKEL

geboren in Naila

1. Gutachter: Prof. Dr. Kai Huang
2. Gutachter: Prof. Dr. Axel Enders

Tag der Einreichung: 15. September 2021
Tag des Kolloquiums: 17. Dezember 2021

Kurzdarstellung

Die vorliegende Arbeit beschäftigt sich experimentell mit granularer Materie, wobei der Fokus auf Monolagen liegt.

Die Experimente beleuchten im ersten Schritt das Verhalten eines einzelnen Teilchens in Abhängigkeit von dessen Partikelform. Hierbei werden Scheiben in einem flachen Container unter vertikaler Anregung betrachtet, deren Umriss als reguläres Polygon mit drei bis acht Ecken systematisch variiert wird. Dabei zeigen sich qualitativ verschiedene Winkelgeschwindigkeitsverteilungen für gerade und ungerade Eckenzahl, sowie eine Kopplung zwischen lateraler Bewegung und Rotation. Die charakteristische Winkelgeschwindigkeit wird näherungsweise mit einem mathematischen Modell beschrieben, welches kontinuierliche Präzession annimmt und die stetige Abhängigkeit von der Containerhöhe im Experiment erfasst. In der Translation zeigt sich eine sprunghafte Mobilitätszunahme oberhalb einer kritischen Containerhöhe, welche das Modell allerdings nicht zu erklären vermag. Die Scheiben legen zudem ein „Gedächtnis“ bezüglich ihrer Rotationsrichtung an den Tag, welches von ihrer Form abhängt.

Das kollektive Verhalten wird im zweiten Schritt anhand einer horizontalen Monolage von regulären Sechskantscheiben experimentell untersucht. Dabei werden zwei stationäre Nichtgleichgewichtszustände näher betrachtet, welche an die Rotator-Phase eines plastischen Kristalls bzw. an eine Flüssigkeit erinnern. Zwischen diesen zeigt sich in Abhängigkeit von der Anregungsfrequenz ein abrupter Übergang. Es deutet sich an, dass unter Umständen auch das Steigern der Vibrationsamplitude zum „Schmelzen“ führen kann. Zu dessen Quantifizierung wird eine verbesserte Version des *bond orientational order parameter*s sowie die Paarverteilungsfunktion herangezogen.

Ein besonderes Augenmerk liegt auf zwei Strategien, die Interaktion in einem Granulat gezielt über die reine Kontaktwechselwirkung zwischen den Teilchen hinaus auszudehnen. Für den Ansatz des teilweise nassen Granulats wird untersucht, inwieweit ein handelsüblicher Tintenstrahldruckkopf eine präzise Kontrolle der Wasserverteilung ermöglicht. Für den Ansatz eines magnetischen Granulats wird ausblickend demonstriert, wie sich eine besonders schnell abfallende magnetische Interaktion technisch realisieren lässt, indem die Teilchen aus je acht Kugelmagneten geformt werden.

Abschließend wird ein Schlaglicht auf vier bemerkenswerte Auswertetechniken geworfen. Drei Interpolationsalgorithmen für die Ergebnisse einer diskreten Fouriertransformation werden anhand von Messdaten verglichen. Für die Darstellung von Wahrscheinlichkeitsdichten wird der optimale Einsatz eines Kerndichteschätzers diskutiert. Im Fall der Kreisdetektion in Kamerabildern mittels der Hough Transformation wird ein Fallstrick bei der Leistungsoptimierung hervorgehoben. Für die konsistente Auswertung lokaler Größen wird die Bedeutung der Mengen-Voronoi-Zerlegung am Beispiel eines stäbchenförmigen Granulats illustriert. Darüber hinaus wird die im Rahmen der vorliegenden Arbeit entstandene Software-Bibliothek vorgestellt, welche die Berechnung der Mengen-Voronoi-Zerlegung für den experimentell besonders häufigen zweidimensionalen Fall ermöglicht.

Abstract

This thesis is concerned with experiments on granular matter and focuses on monolayers.

The experiments examine in the first step the behavior of a single particle in dependence on its shape. Disks, whose shape is varied systematically as regular polygon with three to eight edges, are confined to a flat container and subjected to vertical vibrations. Qualitatively distinct distributions of the angular velocity are found for even and odd numbers of edges as well as a coupling between lateral translation and rotation. The characteristic angular velocity is approximated using a mathematical model which assumes constant precession and captures the continuous dependence on the container height found experimentally. For the translation an abruptly increased mobility is observed above a critical container height which can not be explained by the model. The disks exhibit a "memory" regarding their direction of rotation which depends on their shape.

The collective behavior is investigated experimentally in the second step using a horizontal monolayer of regular hexagon disks. A closer look is taken at two non-equilibrium stationary states which resemble the rotator phase of a plastic crystal and a fluid, respectively. Between them, an abrupt transition in dependence on the excitation frequency appears. In some circumstances increasing the vibration amplitude can lead to a "melting" as well. For the quantification, an improved bond orientational order parameter and the radial distribution function are used.

Particular attention is given to two strategies for extending the interaction in a granulate beyond pure contact forces. For the approach of a partially wet granulate, it is investigated to which extend a common inkjet printhead offers precise control of the water distribution. For the approach of a magnetic granulate, it is demonstrated how an eminently fast decay of the magnetic interaction can be realized technically by forming particles of eight spherical magnets each.

Finally, four remarkable analysis techniques are highlighted. Three interpolation algorithms for the results of a discrete Fourier transform are compared based on measured data. For the visualization of probability densities, the optimal usage of a kernel density estimator is discussed. For the circle detection in camera images by means of the Hough transform, a pitfall in the performance optimization is pointed out. For a consistent analysis of local properties, the significance of Set Voronoi tessellation is illustrated using the example of a rod-like granulate. Furthermore, a software library developed in the course of the present work is presented which facilitates the calculation of the Set Voronoi tessellation in the experimentally particularly common two dimensional case.

Contents

Part I

Outline of Results

1 Introduction

Even though non-equilibrium systems are ubiquitous — all life happens far from thermal equilibrium —, to unveil universal concepts for describing them is still a major challenge (Cross & Greenside, 2009).

To tackle this problem experimentally, granular matter has emerged as a model system in the last decades. With particle sizes on the macroscale, it became experimentally easily accessible thanks to nowadays high resolution digital imaging techniques (Amon *et al.*, 2017). Furthermore, it has proven to be helpful for studying collective behavior (Aranson & Tsimring, 2006). In this context tuning the two essential ingredients, namely single particle behavior and particle-particle interaction, is desired.

This work considers two fundamentally different approaches to tune the particles' interaction: introducing a wetting liquid between granules and letting the particles interact via magnetic fields.

Adding water introduces an interaction which can be isotropic in case of round particles. Moreover, it might allow the realization of a patchy interaction if the particle shape is chosen accordingly. The interaction can be influenced by controlling the added liquid volume (Baur & Huang, 2017, and references therein).

Magnetism on the other hand is intrinsically anisotropic, as the basic building blocks are dipoles. Thus, achieving patchy interaction is straightforward. By creating magnetic clusters (see, e. g., Taheri *et al.*, 2015) of several dipoles, higher order interactions can be achieved (publication 4). Here, tuning the interaction requires a change of the internal arrangement within one cluster.

Restricting experiments to a monolayer is favorable for practical reasons. A two-dimensional system requires significantly less particles than a three-dimensional one for becoming accessible to continuum descriptions. Furthermore, the individual particle remains experimentally directly accessible even for hundreds of particles. These experimental advantages have already enabled a variety of insights. For example, an analogue of surface melting has been found in a two-dimensional granular "crystal" of wet spheres (May *et al.*, 2013). Optical contact force measurements in a monolayer of cylindrical disks (Majmudar & Behringer, 2005; Daniels *et al.*, 2017) allowed to verify predicted scalings in the vicinity of the jamming transition (Majmudar *et al.*, 2007). In addition, the launch of interdisciplinary conferences such as *Traffic and Granular Flow* in 1995 emphasizes the benefits of transferring techniques developed for granular monolayers to socioeconomic systems (Zuriguel *et al.*, 2020).

2 Single Particle Behavior of a Vibrated Polygonal Disk

Aiming at experiments with monolayers, disks are an obvious choice as particle. A single circular disk, e. g., a coin, spun on a table, already exhibits very intriguing dynamics (Olsson, 1972; Leine, 2008) and has become known as Euler's disk (Moffatt, 2000).

Disks on a vertically vibrating surface tend to tilt and exhibit a behavior reminiscent of the settling motion of an Euler's disk. Apart from the vibrated container, the systematic departure from rotational symmetry is a second notable difference of the experiments presented here to the settling coin problem. Regular polygons with n corners (n-gons) are chosen as disk outline, as they offer a systematic deviation from a circle with a natural step size. In publication 1, particles with $3 \leq n \leq 8$ have been investigated. This range includes disks with regular hexagons ($n = 6$) as outline, as used by Baur & Huang (2017). Before studying their collective behavior in the next chapters, this chapter outlining publication 1 concentrates on the behavior of a single particle. Here, we briefly summarize the control parameters tuning the dynamics of a single disk and a comparison to equilibrium systems.

As shown in publication 1, *shape* is a crucial parameter for the dynamics of a vibrated polygonal disk. The "memory" of a single particle regarding its direction of rotation decreases with decreasing n, even if the incircle diameter is kept constant, as revealed by Fig. 8 of publication 1. Furthermore, the particle's behavior sensitively depends on whether its number of corners is even or odd, as illustrated by Figs. 3 and 4 of publication 1.

Another important control parameter for the particle's dynamics is the vertical *confinement*, which is employed to guarantee a quasi two-dimensional situation in the many particle case discussed in the next chapters. It influences the characteristic angular velocity of the particle in a monotonous and continuous fashion, as shown in Fig. 5 of publication 1. In addition, the coupling between translation and rotation changes abruptly, depending on the vertical confinement. A steep increase of translational mobility above a critical confinement height is found (Fig. 6 of publication 1). Furthermore, this abrupt change is accompanied by a jump in the relative phase of rotational and translational motion, as shown in Fig. B1 of publication 1.

A question often associated with non-equilibrium systems inquires about equivalents of principles known from equilibrium thermodynamics, such as equipartition. No equipartition is found for rotational and translational degrees of freedom, as expected due to the strong dissipative character of the system. An interesting relation appears nevertheless temporarily in Fig. 6 of publication 1: The energy contributions in the observed degrees of freedom (two translational and one rotational) tend to equal each other for low container heights in the first half of a vibration period.

Remarkably, different fixed ratios between rotational and translational kinetic energy contributions have been reported for two previous experiments on granular rods, although for different numbers of observed degrees of freedom in each case. While Daniels *et al.* (2009) reports almost equipartition, Harth *et al.* (2013) reports a ratio from translational to rotational energy of 2:1. In contrast, we temporarily find the ratio 1:2. Harth *et al.* (2013) supposes that stronger coupling between rotation and translation, due to a substantially higher filling fraction and 2D confinement, causes equipartition in the experiment of Daniels *et al.* (2009). Publication 1 shows that a 2D confinement can lead to strong coupling between rotation and translation already for a single particle. Even though we tune the coupling via the confinement height, we do not find equipartition.

Phenomenologically, the angular velocity distribution of a single vibrated polygonal disk can be captured by a sum of multiple Gaussians symmetrically arranged with respect to zero, as illustrated in Fig. 4 of publication 1. Here, clockwise and counter-clockwise rotation are a priori equally likely due to the achirality of both, a regular polygon itself and the driving through vibration.

Breaking this symmetry in a controlled way could be a focus of future investigations. Figure 2.1 shows two chiral disks that were derived from a regular hexagon of edge length l. Its edges have been replaced by radial straight lines and arcs starting in tangential direction. By varying the curvature radius ρ of the arcs, the deviation from a regular polygon and the level of chirality can be tuned systematically. This way, the gap to the so-called "vibrots" popularized by Altshuler *et al.* (2013) could be closed, which are sophisticated particles with chirally arranged legs. They are designed to preferably rotate in a fixed direction upon vibration. Their angular velocity distribution has the shape of a single Gaussian with non-zero mean (Scholz & Pöschel, 2017) and they are reported to self-organize (Scholz *et al.*, 2018).

(a) (b) (c)

Figure 2.1: (a) Photograph and (b) camera image from the experimental setup after background removal of chiral, gear shaped disks with a regular hexagon as convex hull. (c) Illustration of the construction defining the parameters. Edge length $l = 5\,\mathrm{mm}$, curvature radius $\rho = 8.66\,\mathrm{mm}$ and core hole diameter $d = 6\,\mathrm{mm}$. Apart from the outline, physical properties are the same as for the particles in publication 1.

3 Collective Behavior of Dry Polygonal Disks

A particle's shape is an important control parameter for the single particle behavior, as discussed in the preceding chapter. Even though for all regular polygons the moment of inertia is isotropic along axes perpendicular to the symmetry axis as detailed in section 7.6, their shape is anisotropic. For convex anisotropic particles in thermal equilibrium, their favored crystal lattice for dense packings can be predicted based on a scalar sphericity measure and their coordination number in a dense fluid (Damasceno *et al.*, 2012). Furthermore, the broken rotational symmetry allows new mesophases to emerge, as known from liquid crystals. Far from thermal equilibrium, nematic order has been demonstrated in a monolayer of granular rods (Müller *et al.*, 2015). This raises the question to which extent universal aspects exist that apply to thermal and athermal systems alike (Müller, 2015).

Extracting meaningful local information from arrangements of anisotropic particles requires special care. Publication 2 points out that classical Voronoi tessellation based on a single point per particle is insufficient for obtaining consistent information on an arrangement of anisotropic particles. Using a monolayer of granular rods as an illustrative example, it clarifies that even supposedly simple order parameters like the local packing fraction (given by the area of a particle to the are area accounted to the particle) are impacted severely by the shortcomings of the classical Voronoi tessellation (Figs. 4 and 5 of publication 2). A Set Voronoi approach, as put forward by Schaller *et al.* (2013), resolves these issues reliably. To conduct Set Voronoi tessellations in 2D efficiently, a Python library has been developed in the course of the present work which is discussed in section 7.5 in detail.

The polygonal disks discussed in the preceding chapter become asymptotically isotropic as their number of corners n approaches infinity. For almost isotropic particles, Damasceno *et al.* (2012) predict hexagonal packing upon crystallization in three dimensions. For thermal equilibrium in two dimensions, a hexatic phase has been predicted for isotropic particles (Halperin & Nelson, 1978). Remarkably, Baur & Huang (2017) report a non-equilibrium stationary state with hexagonal structure for a vibrated monolayer of wet hexagonal disks. This raises the question whether the observed ordering is unique to a wet granulate, which is the focus of the rest of this chapter.

To quantify hexatic order in two dimensions, Halperin & Nelson (1978) propose an order parameter which correlates the angles between lines joining the centers of neighboring particles. Steinhardt *et al.* (1983) suggest a generalization which has become known as the q_l bond orientational order parameter (BOOP). Mickel *et al.* (2013) point out that the traditional BOOP has severe shortcomings arising from the discrete nature of the neighborhood concept and a free choice of its definition.

They advocate to weight the contributions of neighboring particles (as defined by Delaunay edges) based on the common Voronoi cell border and introduce an improved BOOP q_l'. To account as well for the particle's anisotropy, we choose as weight the fraction of the Set Voronoi cell perimeter A separating the particle of interest from its neighbor i, denoted as $\frac{A_i}{A}$. This yields

$$q_l' = \sqrt{\frac{4\pi}{2l+1} \sum_{m=-l\ldots l} \left| \sum_{\text{neighbors } i} \frac{A_i}{A} \cdot Y_{lm}\left(\frac{\pi}{2}, \phi\right) \right|^2}. \tag{3.1}$$

Here, $Y_{lm}(\theta, \phi)$ denotes the spherical harmonics of the "bonds" (Delaunay edges) and it has been exploited that all bonds lie within the monolayer, resulting in a fixed polar angle $\theta = \frac{\pi}{2}$.

With these analysis tools at hand, the collective behavior of a monolayer of regular hexagonal disks upon vertical vibration is investigated experimentally. The following results have been presented in talks at the Spring Meeting 2018 of the German Physical Society (DPG) in Berlin (Völkel & Huang, 2018) as well as the Sino-German symposium 2019 on granular "phase transitions" in Kloster Banz (Völkel & Huang, 2019) and are in preparation for publication.

The collective behavior of $N = 420$ hexagonal disks (parameters $n = 6$, $h = 2\,\text{mm}$, $D = 6\,\text{mm}$, and $d = 4\,\text{mm}$ in the nomenclature of publication 1) is investigated using the experimental setup of publication 1. The container is subjected to vertical vibrations. The particles arrange differently depending on container height H and vibration frequency f, provided sufficiently strong vibration that allows the particles to be lifted off. The frontispiece and the inner side of the back cover each feature a background removed snapshot with the disks exhibiting hexagonal order or not.

To highlight the transition from a hexagonally ordered state to a liquid-like state without order, the improved BOOP is rescaled to

$$\tilde{q}_6' = \frac{q_6' - q_{6,\text{rnd}}'}{q_{6,\text{hex}}' - q_{6,\text{rnd}}'} \tag{3.2}$$

using the values obtained for a perfect planar hexagonal lattice, $q_{6,\text{hex}}' \approx 0.7408$, and for points in a plane drawn from a homogeneous random distribution, $q_{6,\text{rnd}}' = 0.5$. Consequently, melting a perfect hexagonal lattice to a random arrangement is expected to result in $\tilde{q}_6'$ declining from unity to zero.

As the bulk behavior is of interest, only the central region is considered. The central region is found by discarding the outermost shells of particles. All particles whose Set Voronoi cell contains points outside the convex hull of all particle centers are defined to belong to the outermost shell $k = 0$. The $k+1$-outermost shell then consists of all particles which are not part of the $0, 1, \ldots, k$-outermost shells but share an Set Voronoi cell border with an particle belonging to the k-outermost shell. For the following analysis, shells up to $k = 5$ were discarded. This results in a central region of interest (ROI) of approximately half the diameter of the convex hull (mimicking the ROI choice of Müller *et al.* (2015), which is a concentrical circle of half the container's radius) and on average 85 particles for which $\tilde{q}_6'$ is evaluated.

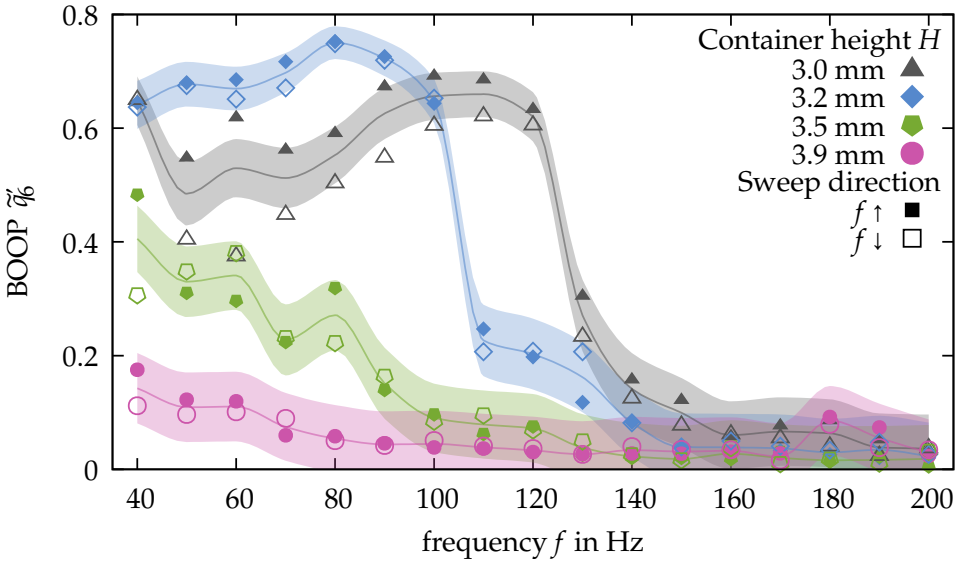

Figure 3.1: Transition between hexagonally ordered and liquid-like state as measured by the improved BOOP $\tilde{q}_6'$. The average for all sweeps with increasing frequency (filled symbols) and decreasing frequency (empty symbols) and the over-all average (solid lines) are displayed respectively. The standard deviation is indicated by the shaded regions. As a guide to the eye, monotone piecewise cubic interpolation (Fritsch & Carlson, 1980) is used between the data points. For $H = 3.0\,\mathrm{mm}$, three sweeps, for $H = 3.9\,\mathrm{mm}$, two sweeps per direction are averaged.

Figure 3.1 shows frequency sweeps in the range $f = 40\,\mathrm{Hz}$ to $200\,\mathrm{Hz}$ for different container heights. The shaded regions indicate the standard deviation of the distribution. A driving signal of constant amplitude is applied, resulting in a dimensionless acceleration of $\Gamma = 5$ to 9 (see section 7.2 for a detailed discussion of the frequency response curve of the setup). No hysteresis is found, indicating that the waiting time of one minute is sufficient for the system to rearrange after a 10 Hz step. The systematically lower $\tilde{q}_6'$ value for decreasing frequency at $H = 3.0\,\mathrm{mm}$ can be attributed almost completely to a single sweep deviating significantly from the others.

Similar to the preceding chapter, the vertical confinement height proves to have a strong influence. For the two lower container heights, $H = 3.0\,\mathrm{mm}$ and $3.2\,\mathrm{mm}$, a clear and sharp transition from a hexagonally ordered state to an unordered, "liquid-like" phase is found. The background removed snapshots on the frontispiece and on the inner side of the back cover correspond to $f = 120\,\mathrm{Hz}$ and $130\,\mathrm{Hz}$ respectively for $H = 3.0\,\mathrm{mm}$. For this confinement height the transition occurs between these two frequencies, for $3.2\,\mathrm{mm}$ it occurs between 100 and 110 Hz.

For the two larger container heights, $H = 3.5\,\mathrm{mm}$ and $3.9\,\mathrm{mm}$, the situation is less clear. As the hexagonal ordering is always significantly less pronounced, a transition is definitely far less incisive. For the largest container height, the maximum

encountered $\tilde{q}_6'$ value barely reaches the level of the unordered state above the clear transition for the low container heights. If the transition still occurs, Fig. 3.1 suggests that the critical frequency continues to decline with increasing container height to $\lesssim 85\,\mathrm{Hz}$ and $< 40\,\mathrm{Hz}$ respectively.

The peak acceleration seems to be of minor influence in the case of dry particles, provided that the particles are sufficiently agitated to reach the container lid. No striking differences between experiments with Γ fixed at 4 and 8 were found, nor in preliminary tests exploring the range up to $\Gamma = 20$. Mechanical resonances of the setup should not play a significant role in the frequency range investigated here either, as discussed in section 7.2. This indicates that an intrinsic timescale determines the transition from the hexagonally ordered to the liquid-like state in the dry case.

Qualitatively speaking, a dependence of the transition frequency on the container height could be reasoned as follows: With increasing container height, the free flying height of a particle increases. An increased free flying height is paralleled by an increased free flying time. If the observed order-disorder transition arises from the free flying time exceeding a certain fraction of the vibration's period time, this would explain the observed trend qualitatively. However, the measurements still defy a quantitative prediction. For a quantitative understanding, further investigation is required, possibly taking into account different modes of motion below and above the transition (as suggested by Figs. 7 and B1 of publication 1).

To conclude, even dry hexagonal disks can self-assemble into a non-equilibrium stationary state which resembles a rotator crystal (Zhao & Mason, 2009). For consistent quantitative results, it is imperative to account for the anisotropy of particles, e. g., by using Set Voronoi based measures. An order-disorder transition that depends on the vertical confinement is found when varying the vibration frequency and thus a characteristic time scale.

An additional energy scale is introduced in the problem if a wetting liquid is added into the container, which will be the focus of the following two chapters.

4 Collective Behavior of Wet Polygonal Disks

Adding a wetting liquid, such as water, to granular matter allows liquid bridges to be formed. These extend the interaction between a particle and its neighbors (or the container) beyond pure contact forces (Herminghaus, 2005). The forces mediated by the liquid are attractive, as the wetting liquid tries to minimize its surface area and thus induces cohesion, at least in the so-called pendular and funicular regime (Mitarai & Nori, 2006). Here, the surface tension of the wetting liquid gives rise to an energy barrier that must be overcome by an individual particle in order to rupture a liquid bridge (Fisher, 1926).

Agitated wet granular matter can exhibit an analogous behavior to melting, if the energy injection per vibration cycle exceeds the rupture energy of the capillary bridges (May *et al.*, 2013). Similarly, Baur & Huang (2017) show that the force balance between driving, gravity, and liquid mediated adhesion to the container bottom determines the acceleration needed to excite wet hexagonal disks so that they can form a rotator crystal. Above this first critical acceleration, they report no qualitative change of the particle order within their experimental range. This raises the question, whether a second critical acceleration exists above which the rotator crystal "melts", comparable to the frequency threshold discussed in the preceding chapter.

A classical technique to detect positional order, that is conceptually simpler than the locally acquired $\tilde{q}_6'$ BOOP, is the radial distribution function $g(r)$, also known as pair correlation function. In a perfect lattice, only distinct distances are found between two sites. In this case, $g(r)$ exhibits distinct peaks at characteristic particle-particle distances r, that can be used to discriminate crystal-like from fluid-like or gas-like granulate (Straßburger & Rehberg, 2000). For a fluid of rigid spheres, $g(r)$ jumps from zero to a finite value at the particle radius and rapidly decays with oscillations to unity for increasing r (Kirkwood *et al.*, 1950).

Figure 4.1a features the radial distribution function for a monolayer of $N = 600$ wet M2.5 hexagon plain brass nuts (ISO 4032, Würth 0300 25, as shown in Fig. 4.1b). They differ from a disk with parameters $n = 6$, $D = 5\,\mathrm{mm}$, $d = 2.5\,\mathrm{mm}$, and $h = 2\,\mathrm{mm}$ only by slightly rounded corners and a thread in the central drilling. This makes them a readily available substitute for hexagonal disks with halved lateral extent of the specifically produced particles of Baur & Huang (2017). For their particles with $D = 10\,\mathrm{mm}$, they report the radial distribution function of $N = 150$ hexagonal disks to be essentially independent of acceleration in the range $20 < \Gamma < 43$. To match their experimental conditions, $H = 3\,\mathrm{mm}$ is chosen and 211 µL purified water (LaboStar TWF, conductivity $\kappa = 0.055\,\frac{\mu\mathrm{S}}{\mathrm{cm}}$) is added as wetting liquid which corresponds to 1 % of the total particle volume. The number of particles is chosen such that they occupy the same area fraction of the container, $\phi \approx 46\,\%$.

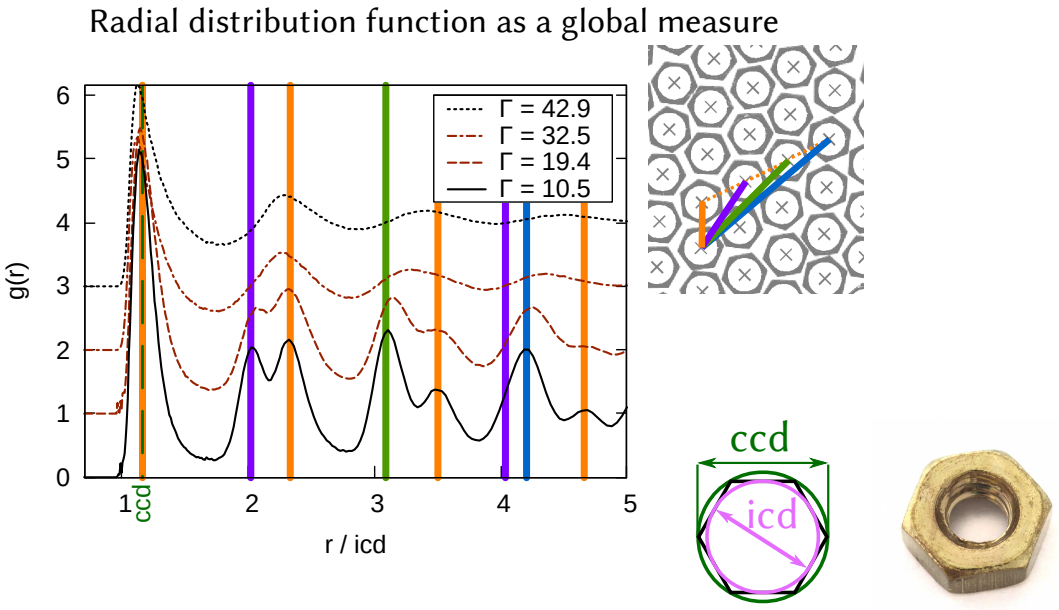

(a) (b)

Figure 4.1: (a) Screenshot of the talk presented at the Spring Meeting 2017 of the German Physical Society in Dresden (Völkel *et al.*, 2017) showing the radial distribution function $g(r)$ for an increasing Γ sweep at $f = 60\,\mathrm{Hz}$ (for clarity, the vertical offset is increased by one for each line) and (b) photograph of a hexagon nut used as particles here.

For low acceleration, the peaks of the radial distribution function clearly coincide with the distances expected in a perfect hexagonal lattice with a lattice constant equal to the first peak. Comparable to Baur & Huang (2017), this first peak coincides with the circumcircle diameter of the screw nuts.

In Fig. 4.1a, showing data for a vibration frequency of $f = 60\,\mathrm{Hz}$, the violet-orange and green-orange double peak structure vanishes for $\Gamma > 30$. This indicates that the hexagonal order is lost and that a melting of a rotator crystal through stronger vibrations might be possible. However, repeating the sweep with $f = 40\,\mathrm{Hz}$, $50\,\mathrm{Hz}$, and $70\,\mathrm{Hz}$ offers an inconclusive picture: Either no significant decay of the crystalline structure is found at all for large accelerations or significant hysteresis between increasing and decreasing the acceleration is found despite otherwise identical experimental parameters or the structure of $g(r)$ decays within the container radius only for the measurement of maximum acceleration.

In conclusion, additional investigation is clearly required in order to clarify under which conditions a rotator crystal of wet polygonal disks can be "molten" by increasing the vibration amplitude.

However, these preliminary experiments reveal three substantial challenges for in-depth investigations: Repeatability demands high precision control of the added volume and distribution of the wetting liquid. The sealing of the container must

remain tight for prolonged durations (up to several hours) and even for driving accelerations up to $\Gamma = 44.7$. Due to the continuous particle impact coupled with the presumably required very high driving accelerations, the wear of the container can become non-negligible, as it is sandblasted by the vibrated particles over time.

The following chapter discussing publication 3 addresses the first challenge and an experimental solution to it in detail.

5 Controlling Liquid Content and Distribution

Mixing sand and water for building sandcastles is very easy, as no precise recipe is needed to obtain a pasty compound. A granular pile can store a significant amount of water, up to about 36 % of its volume (Herminghaus, 2005). The volume fractions which allow building sandcastles span about two orders of magnitude, ranging roughly from 2 ‰ to 20 % (Pakpour *et al.*, 2012). As shown by Scheel *et al.* (2008), it is possible to vary the liquid volume fraction of a wet granulate within a range spanning one order of magnitude without varying its tensile strength more than 10 %. With increasing liquid content, "granular polymers" emerge, which, seen individually, are in the funicular regime as their "pores" are filled by the wetting liquid. As a consequence of this particular self-organized distribution of the wetting liquid, mechanical properties of the three-dimensional sandpile are remarkably consistent (Scheel *et al.*, 2008).

A granular monolayer, however, is largely affected by its supporting boundary. Here, liquid bridges between particles are as important as the bridges between the particles and the bottom of the container (Baur & Huang, 2017). The latter are often undesired. With liquid bridges merely between particles, only a significantly reduced liquid volume can be stored in a 2D granulate. For a rough estimation, it is expedient to consider the volume that can be kept in a single bridge. Semprebon *et al.* (2016) report that 5 % of the spherical volume can be kept in a single bridge using monodisperse spheres with a contact angle of 5°. With three bridges per particle in a hexagonal 2D lattice, a sphere can hold at most about 15 % of its volume. This fraction is also known as liquid content in quasi-2D configurations (May *et al.*, 2013). A conversion to a total volume fraction as in the 3D case is somewhat arbitrary, as it is unclear how the total volume of the monolayer should be defined. Using the diameter of the sphere as the height of the layer results in a maximum total volume fraction of 9 %.

On a microscopic level, liquid mediated forces between individual particles show a rich variety (Semprebon *et al.*, 2016): Already for three equally sized spheres at fixed positions and for a fixed volume of wetting liquid, four different liquid morphologies resembling local energy minima have been found in simulations. Changing the morphology of the wetting liquid (i. e. wetting or dewetting of a neighboring particle) is a discrete event, accompanied by a typically abrupt change of the liquid-air interface. As each morphology results in a different force between the wetted particles, the exact distribution of the wetting liquid plays an important role.

Consequently, experiments on the level of individual particles require suitable tools for precise control and gentle injection of additional liquid volume. The

capillary length scale resulting from the competition between gravity and surface tension limits experiments to length scales of at most a few millimeters (Liu & Kim, 2017). Therefore reproducible volume control in the sub-microliter range is required, which makes experiments very challenging with standard laboratory equipment (Francz *et al.*, 2020).

Publication 3 explores the possibility of employing a standard inkjet printhead to achieve the required resolution in experiments. Using this approach, a volume resolution more than three orders of magnitude finer than standard manual microliter pipettes is achieved.

Figure 5.1 demonstrates the experimental manipulation of an individual liquid bridge by injecting a stream of droplets of (22.4 ± 1.1) pL average volume, produced by a single nozzle of a commercial inkjet printhead. A detailed investigation needs to take into account contact angle hysteresis and surface roughness (cf. Fig. 4 of publication 3), which lead to an asymmetric shape of the bridge in Fig. 5.1. Such experiments address the pendular regime in the nomenclature of Mitarai & Nori (2006).

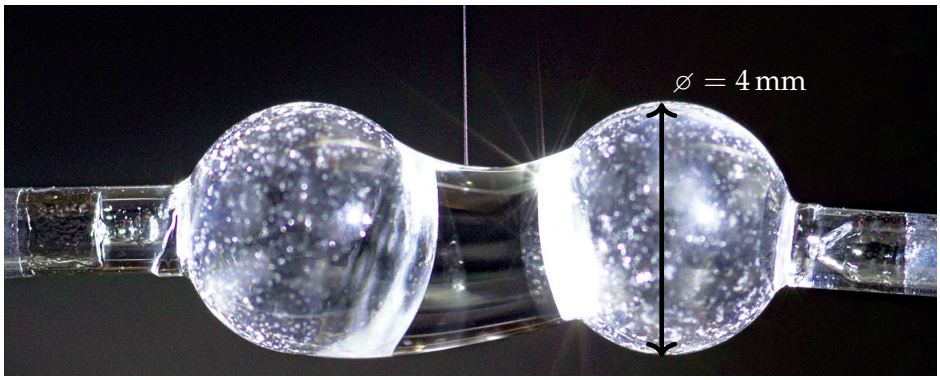

Figure 5.1: Adding liquid to a single liquid bridge between two glass spheres using an inkjet printhead. The bright vertical stripe above the liquid bridge results from the stream of (22.4 ± 1.1) pL droplets produced by the inkjet print head above.

Publication 3 investigates the quasistatic advancing and receding of a wetting front. In the case of a monolayer of glass spheres residing on a glass slide (Fig. 6 of publication 3), this corresponds to experiments addressing the capillary regime (Mitarai & Nori, 2006). If not fully constrained by neighbors, the individual particles are able to reorganize during wetting and dewetting due to the moving liquid-air interface exerting capillary forces on them. The evolution of the liquid-air interface in turn depends on the order in which neighboring particles are wetted. As this is determined by the particular arrangement of the spheres, a very complex and sensitive system emerges. Nevertheless, the printhead's drop rate is sufficiently well controlled and the tiny drop size allows for very gentle injection, yielding high repeatability.

Excellent repeatability and fine volume resolution makes the setup of publication 3 a very promising candidate for creating and manipulating individual liquid bridges

in a granular monolayer. Combining it with a motorized linear stage should allow to tackle the initial wetting liquid distribution challenge, as touched on in the preceding chapter, successfully. However, creating an exceedingly scattered liquid distribution might require substantial further engineering and fine-tuning or the use of multiple printheads. Based on the figures of publication 3, evaporation rates are expected to be an important issue that needs to be addressed for covering the whole container of chapters 2 to 4.

Instead of introducing an additional wetting liquid that resides *between* the particles, the following chapter discussing publication 4 considers extending their interaction beyond pure contact forces by embedding *in* each particle a remarkable cluster of permanent magnets.

6 Exotic Magnetic Interaction for Particles

A way of enabling particles to interact without requiring contact — possibly mediated by an interstitial liquid — is to make them magnetic. While the interaction of magnetic dipoles can be repulsive or attractive depending on their relative orientation, an effective central attraction is achieved if they are allowed to reorient, as the ensemble tries to minimize the magnetic field energy. Magnetic granulate therefore agglomerates, exhibiting interesting dynamics (Kögel *et al.*, 2018).

Magnetic agglomeration is of interest on very different length scales and in various environments. They range from astronomic ones, where magnetic grains are considered to play a decisive role for the formation of certain planet types (Nuth *et al.*, 1994; Kruss & Wurm, 2018), to particles at the nanoscale, colloidally suspended to form ferrofluids (Papell, 1965). Magnetic particles can self-assemble into fascinatingly regular shapes (Taheri *et al.*, 2015). Moreover, magnetic clusters can have surprising equilibrium solutions which are infinitely degenerate (Schönke *et al.*, 2015).

Publication 4 investigates a magnetic cluster with exceptional properties. For eight point dipoles placed at the corners of a cube, the ground state is an example of such an infinitely degenerate equilibrium (Schönke *et al.*, 2015). Publication 4 derives analytically that this exotic ground state is a dotriacontapole (32-pole) whose far-field decays with the inverse seventh power of the distance. As the force on a dotriacontapole depends on the fifth derivative of the magnetic field (see, e. g., Torres del Castillo & Méndez Garrido, 2006), the mutual attraction of two dotriacontapoles decays with the inverse twelfth power of the distance, impacting the time scale for agglomeration severely (appendix C of publication 4).

Figure 6.1 sketches the magnetic flux density in z-direction along a face diagonal in the x-y-plane passing through the center of the cube, as given by Eq. 6 of publication 4. With r denoting the distance to the center of the cube, the magnetic field strength first increases with r^4, reaches its maximum close to the cube's surface and decreases proportional to r^{-7} for large distances.

This remarkably steep decay of the magnetic field strength is confirmed experimentally (Fig. 2 of publication 4) using spherical neodymium magnets with a diameter of 19 mm arranged to a cube with edge length $L = 39.5\,\mathrm{mm}$. For granular experiments, miniaturized versions are clearly favorable, preferably embedded in spherical enclosures, as shown in Fig. 4 of publication 4.

Assembling miniaturized dotriacontapole particles and fixing them in their magnetic ground state proves to be a particular challenge (Braun, 2019): First, all magnets must have the same magnetic moment. Second, for small magnetic spheres, static friction easily exceeds their mutual torque which makes it hard to reach the ground state. Permanent lubrication, however, defies the goal of fixing the spheres' orien-

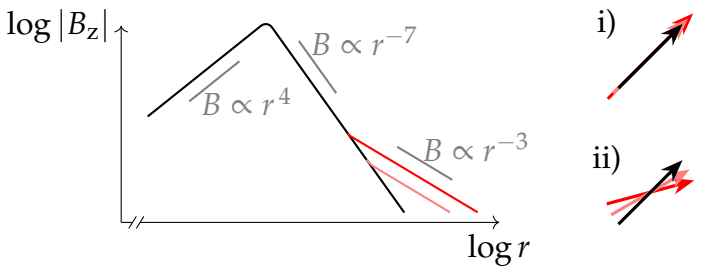

Figure 6.1: Magnetic flux density along one axis $|B_z|$ as a function of the distance r to the center of a dotriacontapole for the ideal case (black) and for a single dipole deviating (pink and red). The r^{-3}-tail can originate, e. g., from (i) one magnetic moment being larger than the ideal one (black), or (ii) being misoriented.

tation once the ground state is reached. In both cases, a single deviating magnet leads to a r^{-3}-tail of the magnetic flux density, as sketched in red in Fig. 6.1. The non-vanishing total dipole moment then dominates the field strength for large distances and effectively limits the range in which the cluster acts as a dotriacontapole.

Concerning future magneto-granular experiments, the successful experimental realization of dotriacontapoles poses the question how they interact collectively. As their name implies, they would provide a particularly patchy granulate. This feature could lead to interesting dynamics beyond slow agglomeration in the dilute case as discussed above.

Finally, publication 4 allows to envision a special kind of magnetic granulate realizing design goals exactly opposite to those discussed at the beginning of this chapter: Particles interacting with each other (almost) exclusively through collisions that can nevertheless be driven by external magnetic fields. Small embedded dotriacontapoles could be dimensioned such that they barely contribute to the mutual interaction. Ideally, the magnetic drive would then be realized using highly inhomogeneous external fields with non-vanishing fourth or even fifth derivative, leading to a torque or force on an ideal dotriacontapole. Relying only on a dipole tail due to imperfections as discussed above would give no advantage over simple permanent magnets in the far field. Preparatory work towards exciting a monolayer of spheres with embedded dotriacontapoles magnetically has already been started by Weber (2019).

7 Technical Details and Supplements

In this chapter, the most notable algorithmic tools which have been used, adapted or developed during this thesis are introduced and explained briefly. Furthermore, additional technical details of the experimental setup are given.

7.1 Improving Amplitude Estimation using DFT Interpolation

To achieve the desired peak acceleration independent of the load on the electromagnetic vibrator and the power amplifier's frequency response curve, the experimental setup used in publication 1 features a control loop. The function generator setting is readjusted according to the acceleration signal, which is sampled using a digital multimeter. The multimeter's sampling frequency is set only indirectly via the integration time configuration. Therefore, the time scale of the function generator is used as reference. As the function generator and digital multimeter are not phase-locked, they are expected to use slightly different time units and drift. The measured acceleration curve therefore appears to have a frequency slightly differing from the set value f_{vib}. Details are provided in the top panel of Fig. 7.1, where f_{vib} is compared to the apparent frequency f_{fit}, obtained as described below.

For extracting the amplitude of the sinusoidal driving from the noisy acceleration signal, a standard technique is least squares fitting. Here, however, as the apparent frequency of the signal is unknown, the fit has to be nonlinear. Convergence is thus not guaranteed, especially for adverse initial values, and the runtime is not constant. Consequently, the least squares approach is disadvantageous for a control loop. Striving for a substitute with constant runtime, this chapter compares three algorithms based on the deviation of their result from a least squares fit's result.

The discrete Fourier transform (DFT) permits finding an unknown frequency in constant time. In the general case, increasing the resolution in the frequency domain comes at the cost of increasing the recording duration unless additional assumptions can be made. Here, it is known that the excitation contains a single frequency. In this case, interpolation approaches have been discussed for more than four decades (Penhune & Martin, 1965; Rife & Vincent, 1970; Jain *et al.*, 1979; Grandke, 1983; Quinn, 1994, 1997). With the DFT result given, only the ratios of the largest absolute value (the *maximizer*) to its two neighboring values need to be considered. To estimate the frequency with sub-bin resolution, the common strategy is to determine the direction of the detuning relative to the maximizer and the detuning modulus in units of the DFT bin spacing.

Quinn (1994) suggests an estimator based solely on the neighbor to maximizer ratios' *real part*. Remarkably, the asymptotic mean standard error of this estimator is

reported to scale with the same power of the sample size as a least squares fit.

Quinn (1997) discusses an algorithm, based solely on the neighbor to maximizer ratios' *modulus* (i. e. absolute value), he refers to as "the estimator of Rife & Vincent". This attribution surprises, as Rife & Vincent (1970) investigate three different interpolation methods and their "method 2" leads to the estimator discussed by Quinn merely for the parameter choice $M = 0$. Furthermore, Rife & Vincent (1970) explicitly acknowledge that this special case had been derived and applied by Penhune & Martin (1965) before. Concededly, this presumably first publication is not publicly available. The technical report number 378 containing the article ESD-TDR-65-41 cited by Rife & Vincent (1970) is left out in the list of unclassified publications of Lincoln Laboratory (Hudson, 1966) and appears to be still classified more than half a century later. Quinn (1997) points out that this established estimator can exhibit a suboptimal performance in terms of asymptotic variance under certain conditions (irrational frequency, the modulus of detuning being very small).

Finally, Quinn (1997) introduces a new estimator combining the two preceding approaches. The direction of the detuning is estimated based on the neighbor to maximizer ratios' real parts and the absolute value is used additionally for estimating the modulus of the detuning. This estimator is consequently referred to as *real part & modulus* in the following.

The performance of these three estimators is compared using experimentally acquired acceleration data as test case in the middle panel of Fig. 7.1. The model $A \sin(2\pi f t) + B \cos(2\pi f t)$ is fitted via frequency f and the parameters determining the amplitude of the sinusoidal vibration, A and B. The result of this nonlinear least squares fit, f_{fit} and $Y_{\text{fit}} = \sqrt{A^2 + B^2}$ respectively, is used as reference for judging the DFT interpolation estimators. The values indicated by the maximizer without any interpolation are added for comparison. Due to the experimental parameters, the spacing between adjacent DFT bins is $\Delta f_{\text{DFT}} = 5\,\text{Hz}$. Without interpolation, the closest frequency evaluated by the DFT differs by roughly $\frac{1}{10}\Delta f_{\text{DFT}}$ from the apparent vibration frequency, as indicated by squares. When comparing the three different interpolation techniques based on either the neighbor to maximizer ratios' modulus (○), real part (△) or modulus and real part (▽), they perform all equally well and determine the detuning to a permille level of the DFT bin spacing. In fact, the first two estimators give nearly indistinguishable results in this test.

The long established estimator, based solely on the neighbor to maximizer ratios' modulus, is used in the control loop of the experimental setup, as it is slightly simpler than the other two. The interpolation is conducted between the maximizer of the DFT Y_m, and its immediate neighbor of larger magnitude Y_l. The detuning modulus is estimated using (Rife & Vincent, 1970, Eq. 109):

$$\delta = \frac{|Y_l|}{|Y_l| + |Y_m|} = \frac{|\frac{Y_l}{Y_m}|}{1 + |\frac{Y_l}{Y_m}|} \,. \tag{7.1}$$

Scalloping loss (see, e. g., Lyons, 2010, chap. 3.10) describes the amplitude underestimation of the DFT maximizer with respect to the signal's true amplitude and occurs if the signal's frequency does not coincide with a frequency sampled by the

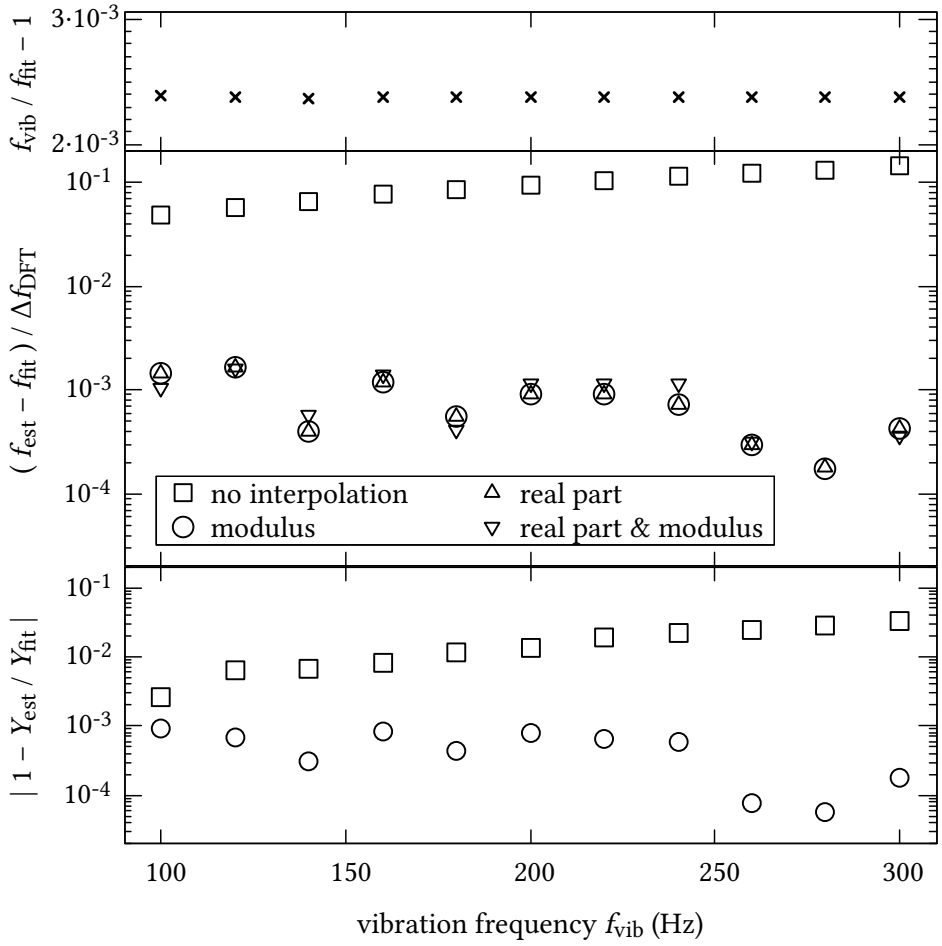

Figure 7.1: Comparison of three DFT interpolation techniques, based on the neighbor to maximizer ratios' modulus, real part or both. Experimental parameters: 3 V peak-to-peak, 50 % gain, $f_{sampling} = 10\,\text{kHz}$, $N = 2000$ samples.

DFT. The squares in the bottom panel of Fig. 7.1 indicate a scalloping loss on the percentage level for the test case if no interpolation is applied. With the detuning δ determined, the scalloping loss can be countered using the sinc-shaped magnitude response curve of a DFT bin. The true amplitude of the sinusoidal vibration is estimated using (Rife & Vincent, 1970, Eq. 113):

$$Y_{est} = \frac{2\,|Y_m|\,\pi\,\delta}{N\,\sin(\pi\,\delta)}\,, \tag{7.2}$$

where N is the number of samples. This reduces the difference between the least squares result and the amplitude estimated via DFT interpolation by typically more than one order of magnitude to a sub-permille level. The estimated amplitude primarily depends on the preceding frequency estimation. Thus only a single interpolation result is shown in the bottom panel for the sake of clarity, representative for all three estimators discussed here.

Note, that in addition to frequency and amplitude, phase can be inferred as well in constant time using DFT interpolation (Jain *et al.*, 1979; Rehberg, 1983). Under certain conditions, these results can be even extended to multitone signals (Jain *et al.*, 1979). DFT interpolation is thus an extremely valuable tool, especially for control loops with strict requirements regarding the runtime.

7.2 Mechanical Resonances

The electromagnetic vibrator setup used in the experiments presented in publication 1 and chapters 3 and 4, is shown in detail in Fig. 7.2. The container consisting of a lid and bottom plate, each made from 1 cm thick polycarbonate (Bayer Makrolon), sandwiching a spacer ring which sets the container height H. A diffusing film is taped to the bottom from below. This sandwich sits on an aluminum base keeping the LEDs for stroboscopic background illumination at a constant distance. On the rim of this base plate, the accelerometer (Dytran 3035B2) is screwed. The aluminum base is mounted on the electromagnetic vibrator's shaft using an adapter plate made from 2 cm thick polyvinyl chloride.

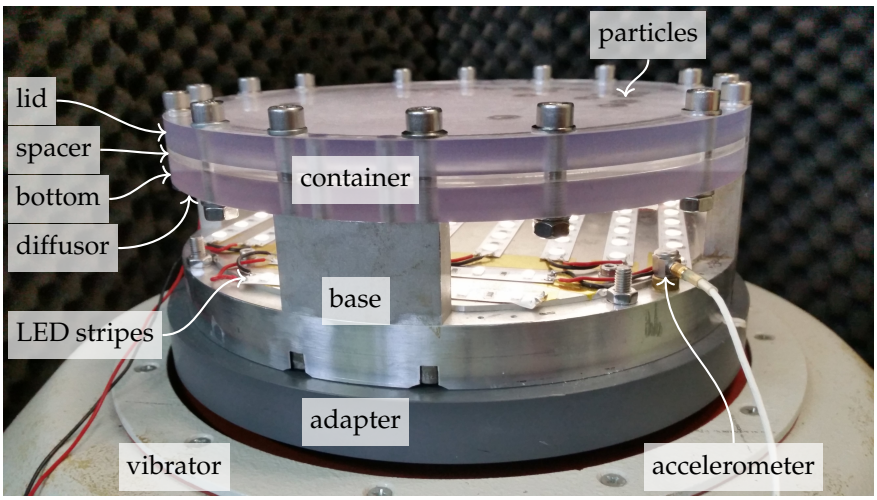

Figure 7.2: Detail view of a container mounted on the vibrator setup

For obtaining the frequency response curve of the experimental setup, a sinusoidal input signal with constant amplitude of 0.1 V is applied to the vibrator's driving circuit, whose power amplifier is set to 50 % gain. The resulting dimensionless acceleration Γ is measured as a function of the vibration frequency f. Figure 7.3a shows the result for an empty container. Two clear peaks are found.

The measured frequency response curve can be captured fairly well by considering the mass-spring-damper model shown in Fig. 7.3b. The adapter, base, and container are each modeled by a point mass m_i ($i \in 1, 2, 3$) connected by a spring with constant k_i and a linear dashpot providing damping λ_i to the next mass respectively the shaft of the vibrator. With their coordinates denoted as x_i respectively x_s for the shaft, this

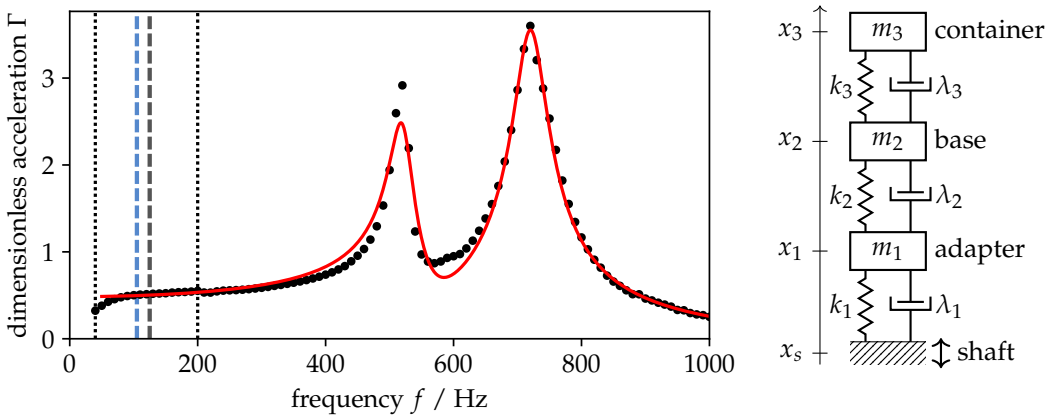

(a) (b)

Figure 7.3: Frequency response curve (a) of the experimental setup for a sinusoidal input signal of constant amplitude and mass-spring-damper model (b) used for the fit (red solid line). The order-disorder transition frequency discussed in chapter 3 (dashed lines) and the frequency range investigated there (dotted lines) are given as reference.

yields as equations of motion

$$\begin{aligned} m_1\,\ddot{x}_1 &= -k_1(x_1 - x_s) - k_2(x_1 - x_2) - \lambda_1(\dot{x}_1 - \dot{x}_s) - \lambda_2(\dot{x}_1 - \dot{x}_2) \\ m_2\,\ddot{x}_2 &= -k_2(x_2 - x_1) - k_3(x_2 - x_3) - \lambda_2(\dot{x}_2 - \dot{x}_1) - \lambda_3(\dot{x}_2 - \dot{x}_3) \\ m_3\,\ddot{x}_3 &= -k_3(x_3 - x_2) \qquad\qquad - \lambda_3(\dot{x}_3 - \dot{x}_2) \qquad . \end{aligned} \tag{7.3}$$

The particular solution to the above set of differential equations for a sinusoidal driving yields the desired frequency response curve. To shorten the notation, the ratios $\omega_i^2 = \frac{m_i}{k_i}$, $\delta_i = \frac{\lambda_i}{k_i}$, $p = \frac{k_2}{k_1}$, and $q = \frac{k_3}{k_2}$ are used in the following. For a sinusoidal drive $x_s(t) = \hat{x}_s \exp(\mathrm{i}\omega\, t)$ of frequency ω and amplitude $|\hat{x}_s|$, the ansatz $x_i(t) = \hat{x}_i \exp(\mathrm{i}\omega\, t)$ suggests itself. Hence, finding the frequency response boils down to solving

$$\boldsymbol{M} \begin{pmatrix} \hat{x}_1 \\ \hat{x}_2 \\ \hat{x}_3 \end{pmatrix} = \begin{pmatrix} \hat{x}_s(1 + \mathrm{i}\omega\,\delta_1) \\ 0 \\ 0 \end{pmatrix}, \text{ where} \tag{7.4}$$

$$\boldsymbol{M} = \begin{pmatrix} 1 + p - \frac{\omega^2}{\omega_1^2} + \mathrm{i}\omega(\delta_1 + \delta_2\, p) & -(1 + \mathrm{i}\omega\,\delta_2)\, p & 0 \\ -(1 + \mathrm{i}\omega\,\delta_2) & 1 + q - \frac{\omega^2}{\omega_2^2} + \mathrm{i}\omega(\delta_2 + \delta_3\, q) & -(1 + \mathrm{i}\omega\,\delta_3)\, q \\ 0 & -(1 + \mathrm{i}\omega\,\delta_3) & 1 - \frac{\omega^2}{\omega_3^2} + \mathrm{i}\omega\,\delta_3 \end{pmatrix}, \tag{7.5}$$

for the (complex) amplitudes $\hat{x}_i$ of each mass m_i.

As the model maps the bending of container, base and adapter to the springs k_i, the accelerometer is attached to m_1 in the model, as it is screwed into the rim of the aluminum base close to a screw connecting it to the adapter. Applying Cramer's

rule (Cramer, 1750, pp. 656–659) yields

$$\hat{x}_1 = \frac{\hat{x}_s(1+\mathrm{i}\omega\,\delta_1)\,\left(\left(1+q-\frac{\omega^2}{\omega_2^2}+\mathrm{i}\omega(\delta_2+\delta_3\,q)\right)\left(1-\frac{\omega^2}{\omega_3^2}+\mathrm{i}\omega\,\delta_3\right)-(1+\mathrm{i}\omega\,\delta_3)^2\,q\right)}{\det(\boldsymbol{M})} \tag{7.6}$$

with $\det(\boldsymbol{M})$ additionally depending on ω_1 and p.

In principle, the absolute value of Eq. (7.6) can be fitted directly to the measured frequency response curve to obtain all nine parameters ω_i, δ_i (with $i \in 1, 2, 3$ each), p, q, and $\hat{x}_s$. In practice, reasonable convergence requires good initial values.

The value of ω_1 is determined in an relatively simple independent experiment. For this purpose, the container and base are removed and the accelerometer gets attached directly to the rim of the adapter. In the mass-spring-damper model, this corresponds to $m_2 = m_3 = 0$, $k_2 = k_3 = 0$, and $\lambda_2 = \lambda_3 = 0$, yielding the standard driven harmonic oscillator. The parameter ω_1 is thus derived from the frequency response of this reduced top, which shows a single resonance around 1000 Hz. To reduce the influence of approximations inherent to the linear point mass model, the fit is carried out only in the range ≤ 910 Hz, where the resulting amplitude remains below ten times the driving amplitude, yielding $f_1 = \frac{\omega_1}{2\pi} = (946 \pm 2)$ Hz.

Figure 7.3a shows the result of a least square fit of Eq. (7.6), with ω_1 fixed to the independently determined value and $\delta_1 = \delta_2 = 0$. This supposes that all damping happens in the container. As without this restriction the fit returns clearly unphysical negative damping values for δ_1 and δ_2, the limits of the simple mass-spring-damper model are reached. However, the model still correctly predicts the most prominent resonance peak to be around 600 Hz with no container mounted on the base (i. e. m_3, k_3, and λ_3 removed).

The frequency range covered in the experiments in chapter 3 is marked by dotted black lines in Fig. 7.3a. Towards its lower limit at 40 Hz, the frequency response of the electromagnetic vibrator falls off slightly. This is no mechanical resonance of the top, as this feature remains if only the accelerometer is mounted (directly) on the shaft. To compensate the falloff, the control loop described in the preceding section has been developed and employed for the experiments in publication 1. The critical frequency, at which the transition between an hexagonally ordered and liquid-like random distribution of the particle occurs, is indicated by the dashed lines respectively. No mechanical resonances can be identified in the vicinity of these frequencies.

7.3 Fast, Accurate and Sub-pixel Resolving Circle Hough Transform

In this section, some additional details concerning the fast, accurate and sub-pixel resolving circle Hough transform discussed in the methods part of publication 1 are given.

The circle Hough transform (Duda & Hart, 1972; Kimme *et al.*, 1975) is a generalization of the original Hough transform (Hough, 1959, 1962) developed for the

recognition and analysis of straight lines. Their common idea is to transform patterns in an image to features in parameter space in such a way that a computationally expensive global detection problem in image space is converted to a simpler local peak detection task in parameter space (Illingworth & Kittler, 1988).

This parameter space is also known as *Hough space* and traditionally represented by an accumulator array (Duda & Hart, 1972) whose dimensionality matches the number of parameters of the object to be found. During the transform, each cell gathers *votes* (Illingworth & Kittler, 1988, and references therein): Its value is incremented for every image pixel that can be explained when assuming that the searched object has the parameters represented by the respective accumulator cell.

For the problem of finding circles of unknown radius, the corresponding Hough transform can be phrased as convolution (Merlin & Farber, 1975; Ballard, 1981) of an edge image with circles of various radii or, when sorting these circles according to their radius along the third dimension, a (possibly truncated) right circular cone (Duda & Hart, 1972; Ballard, 1981).

Hollitt (2012) advances the convolutional approach and suggests to exploit the associativity of convolution by incorporating the edge detection step into a single convolution kernel. Using computationally efficient 3D FFT algorithms this approach promises high performance.

However, it is important to note that the inherent restriction to linear edge filters (otherwise the edge detection step can not be incorporated into the kernel) makes accurate parameter estimation infeasible: A defining characteristic of a *linear* edge filter is that a rising edge and a falling edge (cf. Fig. 7.4c) give exactly opposite responses, as sketched in Fig. 7.4e. After convolution with the Hough cone, the left edge countervails the contribution of the right edge at the circle's center in Hough space. This cancellation of votes leads to a *vanishing* vote density at the circle's center for an ideal setup. It remains a pronounced feature in experiments, highlighted by the green dotted circle in Fig. 7.4f, which is nevertheless inexpedient for accurate parameter estimation, as it is particularly susceptible to noise. In other words, following the proposal of Hollitt (2012) and using only a linear edge filter when analyzing images of nearly undisturbed circles defies the original idea of the Hough transform which is converting the problem of searching a spatially extended pattern to a local maximum search.

To summarize, an accurate parameter estimation using the Hough transform requires the usage of a non-linear edge filter, as illustrated in Fig. 7.4g. The typically more expensive part of the transform can still be performed efficiently using convolution via FFT, but it must necessarily be preceded by a separate edge detection step. The distinct vote density maximum then makes the correct parameters (to within the resolution of the accumulator array) evident, cf. Fig. 7.4h.

Sub-pixel resolution can be achieved when using a Hough cone consisting of blurred circles and subsequently performing a refinement step, as described in publication 1. Using synthetic images of particles with $r = 20.5\,\mathrm{px}$ and 21 px which are shifted systematically between positions with integer coordinates as test case, the average error in the x- or y-coordinate is $8.3 \cdot 10^{-3}\,\mathrm{px}$ and the maximum error remains below 0.13 px.

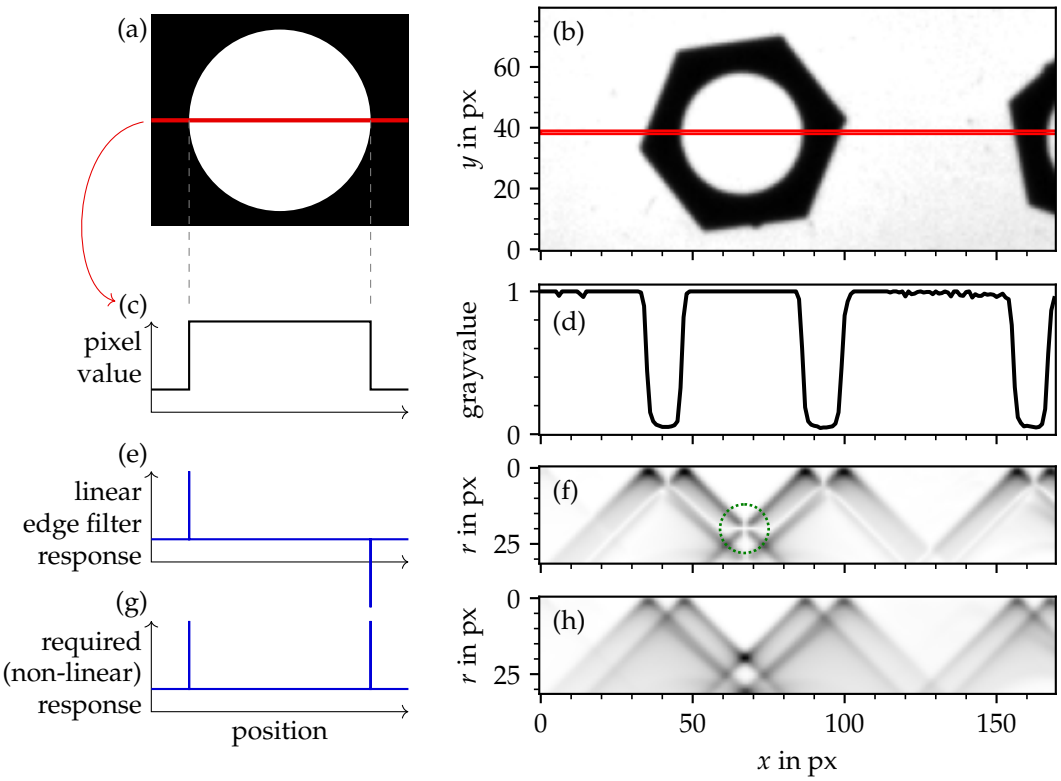

Figure 7.4: Schematic sketch (a) and sample image (b) containing a circle to be found, together with the brightness (c) and (d) along a line (marked in red) passing through the circle's center. Using a linear edge filter (e), the Hough space slice (f) along that line exhibits a vanishing vote density (white) due to the cancellation of votes from opposite edges for the circle's parameters ($x = 67\,\text{px}$, $r = 20\,\text{px}$, highlighted by the green dotted circle). A non-linear edge filter response (g) is required for obtaining in the Hough space slice (h) a vote density maximum (black) for the correct parameters.

7.4 Optimal Kernel Density Estimation with Varying Bandwidth

Kernel density estimation infers a continuous probability density from a finite number of observations. Roughly speaking, this is achieved by convolving a sum of delta-distributions centered at the data points with a window function of chosen bandwidth. The shape of the window function has only a minor effect on the efficiency of the estimation in the asymptotic mean integrated square error (AMISE) sense (Epanechnikov, 1969; Scott, 2015). For many practical applications the main question is thus how to choose the width optimally. This section discusses the different strategies used in the figures of publications 1 and 2, starting with a pragmatic approach and advancing to current state of the art techniques.

Figure 3 of publication 1 employs a kernel density estimate for conveying the local density of data points in crowded regions of the scatter plot. By coloring the symbols accordingly, structures can be visualized not only in dilute parts where individual symbols of reasonable size are still separable, but even in very dense regions where a continuous patch is formed. This enables an intuitive exploration of the dataset and highlights striking features such as multimodality. Here, the kernel density estimate is used primarily to indicate a qualitative trend and not for quantitative analysis. Optimizing for best visual appearance by manually adjusting the bandwidth is absolutely sufficient in this case. This pragmatic approach is arguably quicker than carefully choosing a very sophisticated method if neither quantitative rigor nor automation is required. A fully automatic procedure must take care not to obscure features in complicated distributions by oversmoothing the data.

For very "simple" unimodal and approximately Gaussian distributions, such as the probability density of the local packing fraction obtained with Set Voronoi depicted in Fig. 4 of publication 2, easy rules of thumb can be used for calculating the bandwidth that minimizes the AMISE (Scott, 2015). However, the underlying assumption of known shape has severe implications: With correct a priori knowledge about the shape of the distribution, a fit converges at a faster rate than the nonparametric estimate (Scott, 2015). With an incorrect assumption, an inherent flaw arises. The implications range from an internally inconsistent procedure to arbitrarily bad estimates in adverse cases, e. g., for a mixture of two clearly separable distributions (Devroye *et al.*, 1997).

Multimodal distributions, as found, e. g., in Fig. 4 of publication 1, clearly require a different approach. For a robust method, the dependence on assumptions about the shape of the distribution needs to be relaxed. The "plug-in" procedures put forward by Park & Marron (1990) and Sheather & Jones (1991) achieve this to some degree. They assume a specific distribution merely where the second derivative of the to-be-estimated density is required. While this reduces the impact of the distribution choice on the optimal bandwidth estimate, it still inherits the same flaw (Devroye *et al.*, 1997; Botev *et al.*, 2010). A better solution to this chicken-and-egg problem has been suggested by Botev *et al.* (2010): By numerically finding a self-consistent solution, their Improved-Sheather-Jones (ISJ) algorithm avoids the issues inherent in assuming a specific distribution completely.

While the methods discussed above select a fixed bandwidth with optimal properties, varying the kernel's bandwidth can improve the estimate further (Breiman *et al.*, 1977). To produce an optimal estimate even in regions of low probability, the width should be adapted depending on the local density. Adapting the bandwidth inversely proportional to the square root of the to-be-estimated density is optimal (Abramson, 1982). A straightforward solution is to obtain an optimal pilot estimate using a kernel of fixed bandwidth (Agarwal & Aluru, 2010). Then only the proportionality constant remains to be optimized. It is advisable to use the ISJ algorithm for obtaining the optimal pilot estimate and leave-one-out maximum-likelihood cross-validation (LOO MLCV) for subsequently finding the optimal hyperparameter (Z. Botev, private communication). LOO MLCV (Duin, 1976) gives an optimal result in the sense that it returns the estimate with the highest likelihood to be the density underlying the observations (Silverman, 1986). Kernel density estimation

with optimally varying bandwidth allows for smooth estimates over several orders of magnitudes. This is especially helpful if the tail of a distribution is of interest, like in Fig. A1 of publication 1. All in all, this approach is recommended if there is no prior knowledge about the underlying distribution that can be taken advantage of.

Finally, it is important to note that considering the support (and thus the boundaries) of the estimated probability density is at least as important as the bandwidth choice for an optimal result (Botev *et al.*, 2010; Z. Botev, private communication). To give an example, the local packing fraction in Fig. 4 of publication 2 is non-negative per definition. This lower bound at zero can be easily accounted for using the reflection method (Silverman, 1986). As a symmetric kernel is used, this treatment of the boundary manifests itself in the derivatives vanishing at the vertical axis. For the case of finite support, Botev *et al.* (2010) construct a precise solution, while Silverman (1986) offers a pragmatic approach including an extension to periodic boundary conditions.

7.5 Application Example of Set Voronoi in Two Dimensions

In this section, a minimal application example is given that calculates and displays a Set Voronoi tessellation in two dimensions. The `python` source code in listing 7.1 employs the 2D Set Voronoi implementation `setvoronoi2d.py` which is covered by publication 2 and has been released as free open source software (Völkel, 2020). As a test case, a **Scene** consisting of particles of different size, orientation and shape is constructed: two straight lines, two rectangles, two regular triangles ($n = 3$), three circles and a "wedge"-style particle. The graphical output is shown in Fig. 7.5.

Listing 7.1: Application example of setvoronoi2d.py

```
1  import numpy as np
2  from setvoronoi2d import *
3  scene = Scene(samplingdistance = 10)
4  scene.add_lines(np.array([[105,0,120,30],[-100,200,-50,150]]))
5  scene.add_rectangles(np.array([[100,100], [100,150]]),
       np.array([np.pi/6, 0]), np.array([10, 20]), np.array([5, 7]),
       0)
6  scene.add_regularNgons(np.array([[120,-75], [120,75]]),
       np.array([0, np.pi/2]), np.array([20,21]), 3)
7  scene.add_circles(np.array([[0,0]]), 100)
8  scene.add_circles(np.array([[0,200],[100,220]]), 50)
9  scene.add_points_as_single_particle(np.array([[-100,100],[-90,95],[-80,100]]))
10
11 setvoronoi = Setvoronoi(*scene.dispatch())
12
13 import scipy.spatial
14 import matplotlib.pyplot as plt
15 fig, ax = plt.subplots(1,1)
16 ax.set_aspect(1)
```

```
17 scipy.spatial.voronoi_plot_2d(setvoronoi.circumferencevoronoi,
       ax=ax, show_vertices=False, point_size=1.65, line_width=1.5,
       show_points=True)
18 plt.show()
```

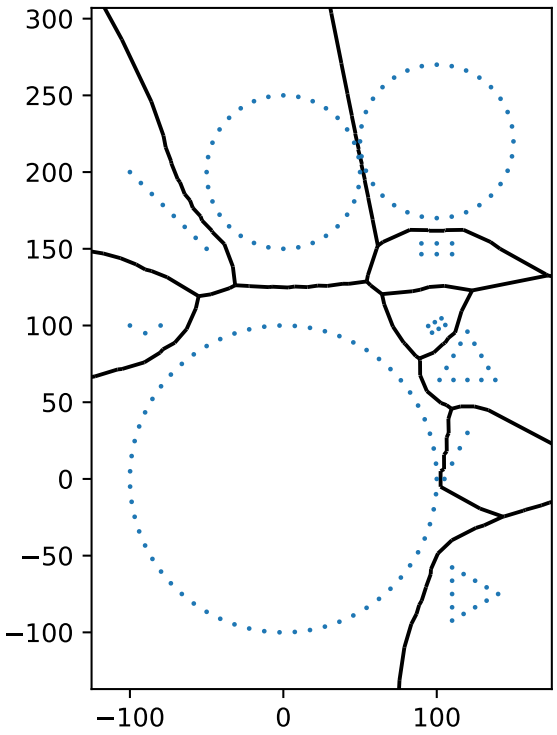

Figure 7.5: Graphical output of listing 7.1 showing the Set Voronoi cell borders (black) alongside with the points (blue) used for obtaining the tessellation.

For convenience, a short discussion of the classes and functions used in listing 7.1 is presented below. For completeness, listing 7.2 at the end of this section details how to access the full documentation of `setvoronoi2d.py`.

Scene

A **Scene** is used to accumulate the points forming the (possibly eroded) circumferences of particles (possibly of different shapes) such that the Set Voronoi tessellation can be calculated easily.

Scene(samplingdistance) is the constructor of the class. **samplingdistance** must be a scalar, indicating the maximum distance between two neighboring points along an edge. For precise interpolation the minimum distance is **samplingdistance**/2. To force this feature, several functions support an optional argument **interpolatePrecisely=True**. Details can be found in the full documentation (see listing 7.2).

The **add_*(...)** functions are offered for conveniently composing a **Scene** by subsequently adding common and even arbitrary types of particles.

add_lines(linesX1Y1X2Y2) adds multiple straight lines by specifying their endpoints. The argument **linesX1Y1X2Y2** must be a **np.array** of shape (**nLines**, 4) and contain along its last axis the coordinates of the endpoints in the order X1 Y1 X2 Y2.

add_rectangles(particlecenters, orientation, l, w, erosiondepth) adds rotated rectangles by specifying their center, orientation and extent. **particlecenters** must be a **np.array** of shape (**nParticles**, 2) and contain along its last axis the coordinates in the order X Y. **orientation**, **l** and **w** must be **np.arrays** of compatible length and of shape (**length**,), i. e. one-dimensional. **orientation** is measured in radians against the +x axis and describes the angle of the edges of length **l**. **l** and **w** indicate the length and width of the rectangles respectively and if applicable before erosion. **erosiondepth** is expected to be a scalar. If **erosiondepth** is positive, the rectangles effectively feature rounded corners with **erosiondepth** as radius. Note, that it is assumed that every rectangle requires all four corners, i. e. **all(l - erosiondepth $>$ 0)** and **all(w - erosiondepth $>$ 0)** evaluate to **True**.

add_regularNgons(particlecenters, orientation, ccr, ncorners) adds regular n-gons by specifying their centers, orientation, circum-circle-radius and number of corners. For **particlecenters** and **orientation**, the same requirements apply as described for **add_rectangles** above, however **orientation** indicates the location of a corner. **ccr** indicates the circum-circle-radius of the regular n-gon and can be either scalar or a **np.array** of compatible length. **ncorners** must be a scalar.

add_circles(particlecenters, erodedradius, ncorners=None) adds circles specified by their center and radius (after erosion). For **particlecenters** the same requirements apply as for the two preceedingly described functions. **erodedradius** (as well as **ncorners** if specified) must be a scalar. If **ncorners** is not set or is **None**, the circles are approximated by a regular n-gon, such that along the arc there is at least one point per **samplingdistance**.

add_points_as_single_particle(circumferencepoints, appendCenter=True) is available for adding a particle of arbitrary shape and interpolation by directly specifying all points lying on the (possibly eroded) circumference. **circumferencepoints** must be a **np.array** of shape (**nPoints**, 2) and contain along its last axis the coordinates in the order X Y. If this function is used for manually adding a particle, **appendCenter** must not be **None**; if a **np.array** is passed, it must be of shape (1, 2) and is directly used as **particlecenter**, otherwise the center is calculated as mean of all **circumferencepoints**.

dispatch() renders the composed **Scene** and returns the data structures required by the constructor of the **Setvoronoi** class.

Setvoronoi

The class **Setvoronoi** implements the algorithms required for performing the actual Set Voronoi tessellation.

Setvoronoi(points, particlecenters, particle2points, point2particle) is the constructor of the class. These mandatory arguments must have the shape of the respective return value of **dispatch()** of a **Scene** instance. The recommended usage

is thus **setvoronoi = Setvoronoi(*scene.dispatch())**. For a description of the optional arguments of the constructor, the reader is referred to the full documentation (cf. listing 7.2).

Listing 7.2: Accessing the full documentation of setvoronoi2d.py

```
1 import setvoronoi2d
2 help(setvoronoi2d)
```

7.6 Moment of Inertia for Special Cases

In this appendix, the moment of inertia is derived for particles in the style of the regular n-gon disks discussed in publication 1.

7.6.1 n-fold Symmetry

The fact that the inertia tensor describes an ellipsoid makes it easy to verify that particles with n-fold symmetry with $n \geq 3$ are a symmetric top:

Lemma 1. *If there are at least three different axes lying in one plane and intersecting in a common point C and for these axes the moment of inertia J is equal, it is identical for all axes lying in this plane and passing through that common point.*

Every (unique) axis with equal moment of inertia contributes two points of equal distance to the origin through which the inertia ellipsoid must pass. From this argument follows that n-fold symmetry for $n = 3$ and $n \geq 5$ is sufficient to have a symmetric top. For $n = 4$ the above argument gives only two distinct or unique axes. Thus a slightly different argument is needed here:

Lemma 2. *If for at least two different pairs of perpendicular axes lying in the same plane and intersecting in one common point it is known that within each pair of axes the moment of inertia is equal, it is identical for all axes lying in this plane and passing through the common point.*

We then obtain two sets of four points through which the inertia ellipsoid has to pass. Due to the symmetry constraints, the only possible solution requires the eight points to lie on a circle. The spinning top is thus symmetric. Note that the prerequisite is obviously fulfilled for 4-fold symmetry. Alternatively we could exploit knowledge about the direction and perpendicularity of the principal axes:

Lemma 3. *If it is known for a pair of perpendicular axes that the moment of inertia is equal and one of these axes is known to be a principal axis, e.g. for symmetry reasons, all axes lying in the plane of these axes and passing through their crossing point have an identical moment of inertia.*

Thus for particles with n-fold symmetry along z passing through C follows for $n \geq 3$:

$$J_{x,C} = J_{y,C} \,. \tag{7.7}$$

7.6.2 Flat Disk

For flat disks (infinitesimal height in z direction) one of the three triangle inequalities for the principal moments of inertia degenerates to an equality:

$$J_\mathrm{x} + J_\mathrm{y} = J_\mathrm{z} \,. \tag{7.8}$$

Thus for flat disks with n-fold symmetry with $n > 3$ follows:

$$J_\mathrm{x} = J_\mathrm{y} = \frac{1}{2} J_\mathrm{z} \,. \tag{7.9}$$

Analogous statements hold for the second moment of area I (replace all J by I in sections 7.6.1 and 7.6.2).

7.6.3 Right Prism

For right prisms of height h (along z-direction) and homogeneous density ϱ, the second moment of area I and the area A of the base can be used to calculate the moment of inertia J:

$$\begin{aligned} J_\mathrm{x,prism} &= \int_{-h/2}^{h/2} \mathrm{d}J_\mathrm{x,prism}(z) \\ &= \int_{-h/2}^{h/2} \left[I_\mathrm{x} \varrho \mathrm{d}z + z^2 \underbrace{A \varrho \mathrm{d}z}_{\mathrm{d}m} \right] \\ &= \varrho I_\mathrm{x} \int_{-h/2}^{h/2} \mathrm{d}z + \varrho A \int_{-h/2}^{h/2} z^2 \mathrm{d}z \\ &= \varrho I_\mathrm{x} h + \frac{1}{12} \varrho A h^3 \\ &= \underbrace{\varrho h}_{\varrho_\mathrm{area}} \left(I_\mathrm{x} + \frac{h^2}{12} A \right) , \end{aligned} \tag{7.10}$$

or if the axis has the distance r from the center of mass:

$$J_\mathrm{x,prism}(r) = \varrho h \left[I_\mathrm{x} + \left(\frac{h^2}{12} + r^2 \right) A \right] . \tag{7.11}$$

For an axis parallel to y the calculation is analogous (replace all subscript x by y). For an axis parallel to z and with the distance r to the center of mass, the result is even slightly simpler:

$$J_\mathrm{z,prism}(r) = \varrho h [I_\mathrm{z} + r^2 A] \,. \tag{7.12}$$

7.6.4 Flat Regular n-gon

For regular polygons with n vertices, the second moment of area along the axis of symmetry z can be obtained by considering n isosceles triangles (Morin, 2008,

pp. 320f). Using the incircle diameter D as characteristic length:

$$I_{\mathrm{z},n\text{-gon}} = \frac{n}{32} D^4 \left(\tan\frac{\pi}{n}\right) \left(\cos\frac{\pi}{n}\right)^{-2} \left(1 - \frac{2}{3}\sin^2\frac{\pi}{n}\right). \tag{7.13}$$

Considering that n-fold symmetry implies a symmetric top and using relation (7.8), we obtain for axes in the plane of the polygon and passing through the centroid:

$$I_{\mathrm{x},n\text{-gon}} = \frac{1}{2} I_{\mathrm{z},n\text{-gon}} = \frac{n}{64} D^4 \left(\tan\frac{\pi}{n}\right) \left(\cos\frac{\pi}{n}\right)^{-2} \left(1 - \frac{2}{3}\sin^2\frac{\pi}{n}\right). \tag{7.14}$$

7.6.5 Regular n-gon Particle with Central Drilling

The prevalent shape of particles used in this work are right prisms of regular n-gons and with a central drilling of diameter d. Along the axis of symmetry z, the moment of inertia can be written as:

$$\begin{aligned} J_{\mathrm{z},n\text{-disk}} &= \varrho h \left[I_{\mathrm{z},n\text{-gon}} - I_{\mathrm{z,circle}} \right] \\ &= \varrho h \left[\frac{n}{32} D^4 \left(\tan\frac{\pi}{n}\right) \left(\cos\frac{\pi}{n}\right)^{-2} \left(1 - \frac{2}{3}\sin^2\frac{\pi}{n}\right) - \frac{\pi}{32} d^4 \right] \end{aligned} \tag{7.15}$$

using the incircle diameter D and particle height h. For an axis lying on the base and intersecting the axis of symmetry we obtain:

$$\begin{aligned} J_{\mathrm{x},n\text{-disk,base}} &= \varrho h \left[I_{\mathrm{x},n\text{-gon}} - I_{\mathrm{x,circle}} + \left(\frac{h^2}{12} + \frac{h^2}{4}\right) \cdot \left(A_{n\text{-gon}} - A_{\mathrm{circle}}\right) \right] \\ &= \varrho h \left[\frac{n}{64} D^4 \left(\tan\frac{\pi}{n}\right) \left(\cos\frac{\pi}{n}\right)^{-2} \left(1 - \frac{2}{3}\sin^2\frac{\pi}{n}\right) - \frac{\pi}{64} d^4 \right. \\ &\qquad \left. + \frac{h^2}{12} \left(n D^2 \tan\frac{\pi}{n} - \pi d^2 \right) \right]. \end{aligned} \tag{7.16}$$

Mass

Using the area of the base $A_{\mathrm{base}} = A_{n\text{-gon}} - A_{\mathrm{circle}} = \frac{1}{4}\left(n D^2 \tan\frac{\pi}{n} - \pi d^2\right)$, the mass of such a particle can be written as:

$$\begin{aligned} m_{n\text{-disk}} &= \varrho h A_{\mathrm{base}} \\ &= \varrho h \frac{1}{4} \left(n D^2 \tan\frac{\pi}{n} - \pi d^2 \right). \end{aligned} \tag{7.17}$$

Radius of Gyration

When dividing the moment of inertia by the mass of the particle, a purely geometric quantity remains. The result is the square of the radius of gyration and independent

of the particle density:

$$
\begin{aligned}
r^2_{\mathrm{g},z,n\text{-disk}} &= \frac{J_{\mathrm{z},n\text{-disk}}}{m_{n\text{-disk}}} \\
&= \frac{\frac{n}{8}D^4\left(\tan\frac{\pi}{n}\right)\left(\cos\frac{\pi}{n}\right)^{-2}\left(1-\frac{2}{3}\sin^2\frac{\pi}{n}\right)-\frac{\pi}{8}d^4}{nD^2\tan\frac{\pi}{n}-\pi d^2} \\
r^2_{\mathrm{g},x,n\text{-disk,base}} &= \frac{J_{\mathrm{x},n\text{-disk,base}}}{m_{n\text{-disk}}} \\
&= \frac{\frac{n}{16}D^4\left(\tan\frac{\pi}{n}\right)\left(\cos\frac{\pi}{n}\right)^{-2}\left(1-\frac{2}{3}\sin^2\frac{\pi}{n}\right)-\frac{\pi}{16}d^4}{nD^2\tan\frac{\pi}{n}-\pi d^2}+\frac{h^2}{3}\,.
\end{aligned}
\tag{7.18}
$$

According to the model used in publication 1, the dynamics of a regular n-gon disk under vertical vibrations is primarily dependent on geometry in general and the particle's radius of gyration in particular. The above equations therefore pave the way for tuning the dynamics of a single regular n-gon disk via tuning its shape.

Bibliography

ABRAMSON, I. S. (1982) *On Bandwidth Variation in Kernel Estimates-A Square Root Law*. The Annals of Statistics **10** (4), 1217–1223. DOI 10.1214/aos/1176345986.

AGARWAL, N. & ALURU, N. R. (2010) *A data-driven stochastic collocation approach for uncertainty quantification in MEMS*. International Journal for Numerical Methods in Engineering **83** (5), 575–597. DOI 10.1002/nme.2844.

ALTSHULER, E., PASTOR, J. M., GARCIMARTÍN, A., ZURIGUEL, I. & MAZA, D. (2013) *Vibrot, a Simple Device for the Conversion of Vibration into Rotation Mediated by Friction: Preliminary Evaluation*. PLoS ONE **8** (8), e67838. DOI 10.1371/journal.pone.0067838.

AMON, A., BORN, P., DANIELS, K. E., DIJKSMAN, J. A., HUANG, K., PARKER, D., SCHRÖTER, M., STANNARIUS, R. & WIERSCHEM, A. (2017) *Preface: Focus on imaging methods in granular physics*. Review of Scientific Instruments **88** (5), 051701. DOI 10.1063/1.4983052.

ARANSON, I. S. & TSIMRING, L. S. (2006) *Patterns and collective behavior in granular media: Theoretical concepts*. Reviews of Modern Physics **78** (2), 641–692. DOI 10.1103/RevModPhys.78.641.

BALLARD, D. H. (1981) *Generalizing the Hough transform to detect arbitrary shapes*. Pattern Recognition **13** (2), 111–122. DOI 10.1016/0031-3203(81)90009-1.

BAUR, M. & HUANG, K. (2017) *Dynamics of wet granular hexagons*. Physical Review E **95** (3), 030901. DOI 10.1103/PhysRevE.95.030901.

BOTEV, Z. I., GROTOWSKI, J. F. & KROESE, D. P. (2010) *Kernel density estimation via diffusion*. The Annals of Statistics **38** (5), 2916–2957. DOI 10.1214/10-aos799.

BRAUN, F. (2019) *Herstellung und Untersuchung magnetischer Dotriakontapole*. Bachelor's thesis, Universität Bayreuth.

BREIMAN, L., MEISEL, W. & PURCELL, E. (1977) *Variable Kernel Estimates of Multivariate Densities*. Technometrics **19** (2), 135–144. DOI 10.1080/00401706.1977.10489521.

TORRES DEL CASTILLO, G. F. & MÉNDEZ GARRIDO, A. (2006) *Torques on quadrupoles*. Revista Mexicana de Física **52** (6).

CRAMER, G. (1750) *Introduction à l'analyse des lignes courbes algébriques*. Geneva: Les frères Cramer et Cl. Philibert.

CROSS, M. & GREENSIDE, H. (2009) *Pattern Formation and Dynamics in Nonequilibrium Systems*. Cambridge University Press. ISBN 9780521770507, DOI 10.1017/cbo9780511627200.

DAMASCENO, P. F., ENGEL, M. & GLOTZER, S. C. (2012) *Predictive Self-Assembly of Polyhedra into Complex Structures*. Science **337** (6093), 453–457. DOI 10.1126/science.1220869.

DANIELS, K. E., KOLLMER, J. E. & PUCKETT, J. G. (2017) *Photoelastic force measurements in granular materials*. Review of Scientific Instruments **88** (5), 051808. DOI 10.1063/1.4983049.

DANIELS, L. J., PARK, Y., LUBENSKY, T. C. & DURIAN, D. J. (2009) *Dynamics of gas-fluidized granular rods*. Physical Review E **79** (4). DOI 10.1103/PhysRevE.79.041301.

DEVROYE, D., BEIRLANT, J., CAO, R., FRAIMAN, R., HALL, P., JONES, M. C., LUGOSI, G., MAMMEN, E., MARRON, J. S., SÁNCHEZ-SELLERO, C., DE UÑA, J., UDINA, F. & DEVROYE, L. (1997) *Universal smoothing factor selection in density estimation: theory and practice*. Test **6** (2), 223–320. DOI 10.1007/bf02564701.

DUDA, R. O. & HART, P. E. (1972) *Use of the Hough Transformation to Detect Lines and Curves in Pictures*. Communications of the ACM **15** (1), 11–15. DOI 10.1145/361237.361242.

DUIN (1976) *On the Choice of Smoothing Parameters for Parzen Estimators of Probability Density Functions*. IEEE Transactions on Computers **C-25** (11), 1175–1179. DOI 10.1109/TC.1976.1674577.

EPANECHNIKOV, V. A. (1969) *Non-Parametric Estimation of a Multivariate Probability Density*. Theory of Probability & Its Applications **14** (1), 153–158. DOI 10.1137/1114019.

FISHER, R. A. (1926) *On the capillary forces in an ideal soil; correction of formulae given by W. B. Haines*. The Journal of Agricultural Science **16** (3), 492–505. DOI 10.1017/s0021859600007838.

FRANCZ, B., UNGAI-SALÁNKI, R., SAUTNER, É., HORVATH, R. & SZABÓ, B. (2020) *Subnanoliter precision piezo pipette for single-cell isolation and droplet printing*. Microfluidics and Nanofluidics **24** (2). DOI 10.1007/s10404-019-2317-8.

FRITSCH, F. N. & CARLSON, R. E. (1980) *Monotone Piecewise Cubic Interpolation*. SIAM Journal on Numerical Analysis **17** (2), 238–246. DOI 10.1137/0717021.

GRANDKE, T. (1983) *Interpolation Algorithms for Discrete Fourier Transforms of Weighted Signals*. IEEE Transactions on Instrumentation and Measurement **32** (2), 350–355. DOI 10.1109/tim.1983.4315077.

HALPERIN, B. I. & NELSON, D. R. (1978) *Theory of Two-Dimensional Melting*. Physical Review Letters **41** (2), 121–124. DOI 10.1103/PhysRevLett.41.121.

HARTH, K., KORNEK, U., TRITTEL, T., STRACHAUER, U., HÖME, S., WILL, K. & STANNARIUS, R. (2013) *Granular Gases of Rod-Shaped Grains in Microgravity*. Physical Review Letters **110** (14). DOI 10.1103/physrevlett.110.144102.

HERMINGHAUS, S. (2005) *Dynamics of wet granular matter*. Advances in Physics **54**, 221–261. DOI 10.1080/00018730500167855.

HOLLITT, C. (2012) *A convolution approach to the circle Hough transform for arbitrary radius*. Machine Vision and Applications **24** (4), 683–694. DOI 10.1007/s00138-012-0420-x.

HOUGH, P. V. C. (1959) *Machine Analysis of Bubble Chamber Pictures*. Proceedings of International Conference on High Energy Accelerators and Instrumentation **590914**, 554–558.

HOUGH, P. V. C. (1962) *Method and Means for Recognizing Complex Patterns*. US Patent 3069654.

HUDSON, F. C. (1966) *Unclassified Publications of Lincoln Laboratory*. AD803845, M.I.T. Lincoln Labs., Lexington, Mass.

ILLINGWORTH, J. & KITTLER, J. (1988) *A survey of the hough transform*. Computer Vision, Graphics, and Image Processing **44** (1), 87–116. DOI 10.1016/s0734-189x(88)80033-1.

JAIN, V. K., COLLINS, W. L. & DAVIS, D. C. (1979) *High-Accuracy Analog Measurements via Interpolated FFT*. IEEE Transactions on Instrumentation and Measurement **28** (2), 113–122. DOI 10.1109/tim.1979.4314779.

KIMME, C., BALLARD, D. & SKLANSKY, J. (1975) *Finding circles by an array of accumulators*. Communications of the ACM **18** (2), 120–122. DOI 10.1145/360666.360677.

KIRKWOOD, J. G., MAUN, E. K. & ALDER, B. J. (1950) *Radial Distribution Functions and the Equation of State of a Fluid Composed of Rigid Spherical Molecules*. The Journal of Chemical Physics **18** (8), 1040–1047. DOI 10.1063/1.1747854.

KRUSS, M. & WURM, G. (2018) *Seeding the Formation of Mercurys: An Iron-sensitive Bouncing Barrier in Disk Magnetic Fields*. The Astrophysical Journal **869** (1), 45. DOI 10.3847/1538-4357/aaec78.

KÖGEL, A., SÁNCHEZ, P. A., MARETZKI, R., DUMONT, T., PYANZINA, E. S., KANTOROVICH, S. S. & RICHTER, R. (2018) *Coarsening dynamics of ferromagnetic granular networks—experimental results and simulations*. Soft Matter **14** (6), 1001–1015. DOI 10.1039/c7sm00796e.

LEINE, R. I. (2008) *Experimental and theoretical investigation of the energy dissipation of a rolling disk during its final stage of motion*. Archive of Applied Mechanics **79** (11), 1063–1082. DOI 10.1007/s00419-008-0278-6.

LIU, T. ". & KIM, C.-J. ". (2017) *Contact Angle Measurement of Small Capillary Length Liquid in Super-repelled State*. Scientific Reports **7** (1). DOI 10.1038/s41598-017-00607-9.

LYONS, R. G. (2010) *Understanding Digital Signal Processing*, 3rd edition. Prentice Hall. ISBN 9780137027415.

MAJMUDAR, T. S. & BEHRINGER, R. P. (2005) *Contact force measurements and stress-induced anisotropy in granular materials*. Nature **435** (7045), 1079–1082. DOI 10.1038/nature03805.

MAJMUDAR, T. S., SPERL, M., LUDING, S. & BEHRINGER, R. P. (2007) *Jamming Transition in Granular Systems*. Physical Review Letters **98** (5). DOI 10.1103/PhysRevLett.98.058001.

MAY, C., WILD, M., REHBERG, I. & HUANG, K. (2013) *Analog of surface melting in a macroscopic nonequilibrium system*. Physical Review E **88** (6), 062201. DOI 10.1103/PhysRevE.88.062201.

MERLIN, P. M. & FARBER, D. J. (1975) *A Parallel Mechanism for Detecting Curves in Pictures*. IEEE Transactions on Computers **C-24** (1), 96–98. DOI 10.1109/T-C.1975.224087.

MICKEL, W., KAPFER, S. C., SCHRÖDER-TURK, G. E. & MECKE, K. (2013) *Shortcomings of the bond orientational order parameters for the analysis of disordered particulate matter*. The Journal of Chemical Physics **138** (4), 044501. DOI 10.1063/1.4774084.

MITARAI, N. & NORI, F. (2006) *Wet granular materials*. Advances in Physics **55** (1-2), 1–45.

MOFFATT, H. K. (2000) *Euler's disk and its finite-time singularity*. Nature **404** (6780), 833–834. DOI 10.1038/35009017.

MORIN, D. (2008) *Introduction to Classical Mechanics*. Cambridge University Press. ISBN 0521876222, DOI 10.1017/cbo9780511808951.

MÜLLER, T. (2015) *Mesophases in Molecular and Granular Systems: From Liquid Crystalline Polymers to Granular Rods*. PhD thesis, Universität Bayreuth.

MÜLLER, T., DE LAS HERAS, D., REHBERG, I. & HUANG, K. (2015) *Ordering in granular-rod monolayers driven far from thermodynamic equilibrium*. Physical Review E **91** (6). DOI 10.1103/PhysRevE.91.062207.

NUTH, J. A., BERG, O., FARIS, J. & WASILEWSKI, P. (1994) *Magnetically Enhanced Coagulation of Very Small Iron Grains*. Icarus **107** (1), 155–163. DOI 10.1006/icar.1994.1013.

OLSSON, M. G. (1972) *Coin Spinning On a Table*. American Journal of Physics **40** (10), 1543–1545. DOI 10.1119/1.1986889.

PAKPOUR, M., HABIBI, M., MØLLER, P. & BONN, D. (2012) *How to construct the perfect sandcastle*. Scientific Reports **2** (1). DOI 10.1038/srep00549.

PAPELL, S. S. (1965) *Low Viscosity Magnetic Fluid Obtained by the Colloidal Suspension of Magnetic Particles*. US Patent 3215572.

PARK, B. U. & MARRON, J. S. (1990) *Comparison of Data-Driven Bandwidth Selectors*. Journal of the American Statistical Association **85** (409), 66–72. DOI 10.1080/01621459.1990.10475307.

PENHUNE, J. P. & MARTIN, L. R. (1965) *Determination of Doppler Velocity and Ballistic Coefficient from Coherent Radar Data*. ESD-TDR-65-41, Technical report 378, M.I.T. Lincoln Labs., Lexington, Mass., pp. 11–53. Unavailable.

QUINN, B. (1994) *Estimating frequency by interpolation using Fourier coefficients*. IEEE Transactions on Signal Processing **42** (5), 1264–1268. DOI 10.1109/78.295186.

QUINN, B. (1997) *Estimation of frequency, amplitude, and phase from the DFT of a time series*. IEEE Transactions on Signal Processing **45** (3), 814–817. DOI 10.1109/78.558515.

REHBERG, I. (1983) *Eine strömungsakustische Spitzenkatastrophe*. In Mitteilungen aus dem Max-Planck-Institut für Strömungsforschung, Nr. 75 (ed. E.-A. Müller).

RIFE, D. C. & VINCENT, G. A. (1970) *Use of the Discrete Fourier Transform in the Measurement of Frequencies and Levels of Tones*. Bell System Technical Journal **49** (2), 197–228. DOI 10.1002/j.1538-7305.1970.tb01766.x.

SCHALLER *et al.*, F. M. (2013) *Set Voronoi diagrams of 3D assemblies of aspherical particles*. Philosophical Magazine **93** (31-33), 3993–4017. DOI 10.1080/14786435.2013.834389.

SCHEEL, M., SEEMANN, R., BRINKMANN, M., MICHIEL, M. D., SHEPPARD, A., BREIDENBACH, B. & HERMINGHAUS, S. (2008) *Morphological clues to wet granular pile stability*. Nature Materials **7** (3), 189–193. DOI 10.1038/nmat2117.

SCHOLZ, C., ENGEL, M. & PÖSCHEL, T. (2018) *Publisher Correction: Rotating robots move collectively and self-organize*. Nature Communications **9** (1). DOI 10.1038/s41467-018-03873-x.

SCHOLZ, C. & PÖSCHEL, T. (2017) *Velocity Distribution of a Homogeneously Driven Two-Dimensional Granular Gas*. Physical Review Letters **118** (19). DOI 10.1103/PhysRevLett.118.198003.

SCHÖNKE, J., SCHNEIDER, T. M. & REHBERG, I. (2015) *Infinite geometric frustration in a cubic dipole cluster*. Physical Review B **91** (2). DOI 10.1103/physrevb.91.020410.

SCOTT (2015) *Multivariate Density Estimation*. John Wiley & Sons. ISBN 9780471697558, DOI 10.1002/9781118575574.

SEMPREBON, C., SCHEEL, M., HERMINGHAUS, S., SEEMANN, R. & BRINKMANN, M. (2016) *Liquid morphologies and capillary forces between three spherical beads*. Physical Review E **94** (1). DOI 10.1103/PhysRevE.94.012907.

SHEATHER, S. J. & JONES, M. C. (1991) *A Reliable Data-Based Bandwidth Selection Method for Kernel Density Estimation*. Journal of the Royal Statistical Society: Series B (Methodological) **53** (3), 683–690. DOI 10.1111/j.2517-6161.1991.tb01857.x.

SILVERMAN, B. W. (1986) *Density Estimation for Statistics and Data Analysis*, first edition. Taylor & Francis Ltd. ISBN 0412246201.

STEINHARDT, P. J., NELSON, D. R. & RONCHETTI, M. (1983) *Bond-orientational order in liquids and glasses*. Physical Review B **28** (2), 784–805. DOI 10.1103/physrevb.28.784.

STRASSBURGER, G. & REHBERG, I. (2000) *Crystallization in a horizontally vibrated monolayer of spheres*. Physical Review E **62** (2), 2517–2520. DOI 10.1103/physreve.62.2517.

TAHERI, S. M., MICHAELIS, M., FRIEDRICH, T., FÖRSTER, B., DRECHSLER, M., RÖMER, F. M., BÖSECKE, P., NARAYANAN, T., WEBER, B., REHBERG, I., ROSENFELDT, S. & FÖRSTER, S. (2015) *Self-assembly of smallest magnetic particles*. Proceedings of the National Academy of Sciences **112** (47), 14484–14489. DOI 10.1073/pnas.1511443112.

TANGE, O. (2011) *GNU Parallel - The Command-Line Power Tool*. ;login: The USENIX Magazine **36** (1), 42–47.

VÖLKEL, S. (2020) *setvoronoi2d: Calculate the Set Voronoi tessellation in two dimensions*. DOI 10.5281/zenodo.3531545.

VÖLKEL, S., BAUR, M. & HUANG, K. (2017, March 19–24) *Dancing screw nuts: collective behaviour under vertical vibrations* [Conference presentation]. DPG Spring Meeting of the Condensed Matter Section, Dresden, Germany. URL `https://www.dpg-verhandlungen.de/year/2017/conference/dresden/part/dy/session/31/contribution/8`.

VÖLKEL, S. & HUANG, K. (2018, March 11–16) *Rotator crystals in a granular monolayer* [Conference presentation]. 2018 Joint meeting of the DPG and EPS Condensed Matter Divisions, Berlin, Germany. URL `https://www.dpg-verhandlungen.de/year/2018/conference/berlin/part/dy/session/61/contribution/2`.

VÖLKEL, S. & HUANG, K. (2019, April 14–16) *Dancing screw-nuts: From individual spinners to rotator crystal* [Conference presentation]. Sino-German Symposium on Granular "Phase Transitions": From Fundamentals to Applications, Kloster Banz, Germany.

WEBER, A. (2019) *Untersuchung des frequenzabhängigen Rollverhaltens eines kugelförmig eingeschlossenen Dotriakontapols*. Bachelor's thesis, Universität Bayreuth.

ZHAO, K. & MASON, T. G. (2009) *Frustrated Rotator Crystals and Glasses of Brownian Pentagons*. Physical Review Letters **103** (20). DOI 10.1103/physrevlett.103.208302.

ZURIGUEL, I., GARCIMARTIN, A. & CRUZ, R. (eds.) (2020) *Traffic and Granular Flow 2019*. Springer International Publishing. ISBN 9783030559731, DOI 10.1007/978-3-030-55973-1.

List of Publications

Peer-reviewed

- KÖSTLER, S., ZHAO, J., LYU, C., VÖLKEL, S. & HUANG, K. (2021) *Embedded inertial sensor for tracking projectile impact on granular media*. EPJ Web of Conferences **249**, 15007. DOI 10.1051/epjconf/202124915007.
- VÖLKEL, S. & HUANG, K. (2020) *Coupling between rotational and translational motions of a vibrated polygonal disk*. New Journal of Physics **22**, 123018. DOI 10.1088/1367-2630/abcc9a.
- VÖLKEL, S. & HUANG, K. (2020) *Set Voronoi Tessellation for Particulate Systems in Two Dimensions*. In: Iker Zuriguel, Angel Garcimartín, Raúl Cruz Hidalgo (eds.) Traffic and Granular Flow 2019. Springer Proceedings in Physics, vol **252**. Springer, Cham, Switzerland. DOI 10.1007/978-3-030-55973-1_53.
- HARTUNG, S., SOMMER, F., VÖLKEL, S., SCHÖNKE, J. & REHBERG, I. (2018) *Assembly of eight spherical magnets into a dotriacontapole configuration*. Physical Review B **98**, 214424. DOI 10.1103/PhysRevB.98.214424.
- BORGERS, S., VÖLKEL, S., SCHÖPF, W. & REHBERG, I. (2018) *Exploring cogging free magnetic gears*. American Journal of Physics **86**(6), 460–469. DOI 10.1119/1.5029823.
- VÖLKEL, S. & HUANG, K. (2017) *Dynamics of wetting explored with inkjet printing*. EPJ Web of Conferences **140**, 09035. DOI 10.1051/epjconf/201714009035.
- BUTZHAMMER, L., VÖLKEL, S., REHBERG, I. & HUANG, K. (2015) *Pattern formation in wet granular matter under vertical vibrations*. Physical Review E **92**, 012202. DOI 10.1103/PhysRevE.92.012202.

Non-refereed

- KRAUSS, S., VÖLKEL, S., DOBNER, C., VÖLKEL, A. & HUANG, K. (2019) *Acoustics of Margravial Opera House Bayreuth*, Fortschritte der Akustik - DAGA 2019, 607–610.

Software

- Völkel, S. (2020) *setvoronoi2d: Calculate the Set Voronoi tessellation in two dimensions*. DOI 10.5281/zenodo.3531545.

Selected oral presentations

- VÖLKEL, S. & HUANG, K. (2021, March 22–24) *Coupling between rotational and translational motions of a vibrated polygonal disk* [Conference presentation]. Virtual DPG Spring Meeting BP-CPP-DY-SOE, online.
- VÖLKEL, S. & HUANG, K. (2019, July 2–5) *Two-dimensional set-voronoi tessellation for particulate systems* [Conference presentation]. Traffic and Granular Flow 2019, Pamplona, Spain.
- VÖLKEL, S. & HUANG, K. (2019, April 14–16) *Dancing screw-nuts: From individual spinners to rotator crystal* [Conference presentation]. Sino-German Symposium on Granular "Phase Transitions": From Fundamentals to Applications, Kloster Banz, Germany.
- VÖLKEL, S. & HUANG, K. (2019, March 31 – April 5) *Dynamics of polygonal disks under vertical vibrations* [Conference presentation]. DPG Spring Meeting of the Condensed Matter Section, Regensburg, Germany.
- VÖLKEL, S. & HUANG, K. (2018, July 13) *Rotator crystals in a monolayer of vertically vibrated discs* [Colloquium presentation]. Series of Academic Reports of the Key Laboratory of Soft Matter Physics, Chinese Academy of Sciences, Beijing, China.
- VÖLKEL, S., LANDGRAF, J. & HUANG, K. (2018, July 13) *Growing drops on an inclined plane: evolution of shape* [Colloquium presentation]. Series of Academic Reports of the Key Laboratory of Soft Matter Physics, Chinese Academy of Sciences, Beijing, China.
- VÖLKEL, S. & HUANG, K. (2018, March 11–16) *Rotator crystals in a granular monolayer* [Conference presentation]. 2018 Joint meeting of the DPG and EPS Condensed Matter Divisions, Berlin, Germany.
- VÖLKEL, S., LANDGRAF, J. & HUANG, K. (2018, June 29) *Growing drops on an inclined plane: onset of sliding* [Invited presentation]. CRC 1194 PhD colloquium, Darmstadt, Germany.
- VÖLKEL, S., LANDGRAF, J. & HUANG, K. (2017, November 19–21) *Experiments on the onset of motion of sliding drops* [Conference presentation]. 70th Annual Meeting of the APS Division of Fluid Dynamics, Denver, Colorado, USA.
- VÖLKEL, S. & HUANG, K. (2017, July 3–7) *Dynamics of wetting explored with inkjet printing* [Conference presentation]. Powders and Grains 2017, Montpellier, France.
- VÖLKEL, S., BAUR, M. & HUANG, K. (2017, March 19–24) *Dancing screw nuts: collective behaviour under vertical vibrations* [Conference presentation]. DPG Spring Meeting of the Condensed Matter Section, Dresden, Germany.
- VÖLKEL, S. (2016, September 4–9) *Onset of motion of sliding drops on a granular bed* [Conference presentation]. CMD26 – Condensed Matter Conference, Groningen, Netherlands.

Part II

Publications

Publication 1

Coupling between rotational and translational motions of a vibrated polygonal disk

Simeon Völkel and Kai Huang

New Journal of Physics **22**, 123018 (2020)
(DOI: 10.1088/1367-2630/abcc9a)

My contribution (70 %) consists in developing the software used for control and automation, designing, implementing and characterizing the automatic image analysis, conducting and analyzing all experiments, performing the kernel density estimation, preparing all but one figure and writing the first draft of the manuscript.

Kai Huang contributed (30 %) the analytical model and improved the manuscript substantially.

New Journal of Physics
The open access journal at the forefront of physics

Deutsche Physikalische Gesellschaft DPG
IOP Institute of Physics

Published in partnership with: Deutsche Physikalische Gesellschaft and the Institute of Physics

OPEN ACCESS

RECEIVED
23 September 2020

REVISED
16 November 2020

ACCEPTED FOR PUBLICATION
20 November 2020

PUBLISHED
21 December 2020

PAPER

Coupling between rotational and translational motions of a vibrated polygonal disk

Simeon Völkel[1,*] and Kai Huang[1,2]

[1] Experimentalphysik V, Universität Bayreuth, 95440 Bayreuth, Germany
[2] Division of Natural and Applied Sciences, Duke Kunshan University, 215306, Kunshan, Jiangsu, People's Republic of China
[*] Author to whom any correspondence should be addressed.

E-mail: simeon.voelkel@uni-bayreuth.de and kh380@duke.edu

Keywords: nonlinear dynamics, granular materials, granular monolayers, nonequilibrium systems

Abstract

We investigate experimentally the dynamics of a single polygonal disk (regular n-gon with $3 \leqslant n \leqslant 8$) confined in a closed container under vertical vibrations against gravity. The disks tend to precess continuously upon vibrations, transferring mechanical energy into rotational and lateral translational degrees of freedom (DoF). An analysis of the velocity distribution functions in both DoF suggests that the mobility in both DoF are coupled with each other, exhibiting a characteristic angular velocity that depends on confinement and disk shape. The characteristic angular velocity can be captured with an analytical model considering sustainable precession due to continuous driving. Depending on confinement, translational and rotational kinetic energy fluctuations within one vibration cycle can be synchronized with each other and there exists a regime where injected energy is equally distributed in different DoF. Depending on n, the tendency for the disk to precess varies and there exists a regime ($n \leqslant 6$) where persistent rotation of the disk rarely lasts longer than one vibration period. Our results suggest the possibility of tuning energy injection into different DoF in vibrated granular disk mono-layers via shape design and confinement.

1. Introduction

An object driven by mechanical vibrations (e.g., a ball bouncing on a vibrating plate) exhibits rich nonlinear and chaotic dynamics [1]. From spheres to dimers and trimers [2–5], from self-propelled rods and polar disks to 'vibrots' [6–12], from chiral wires to screw nuts and bolt-like particles [13–15], the collective behavior of vibrofluidized particles of various shapes has received a growing interest in the past decades. The dissipative feature characterizes driven granular particles as a model system for a better understanding of widespread nonequilibrium systems in nature, such as the collective dynamics of bacteria colonies, migration of birds, and pedestrian flow [16–18]. Depending on the object shape, driving and confining conditions, the dynamical behavior of a single particle differs, owing to distinct ways of re-distributing the injected kinetic energy into different DoF. Due to continuous in- and out-flux of energy, granular systems are driven far from thermodynamic equilibrium. Although fundamental concepts such as free energy minimization and equipartition cannot be taken as granted in such systems, recent investigations on the collective behavior of vibro-fluidized granular materials reveal the similarity between the stationary states in the nonequilibrium *model* system and the thermally driven atomic and colloidal systems, such as crystallization, surface melting, phase separation, and liquid-crystal mesophase [10, 19–24].

In a recent investigation [14], we showed that a monolayer of hexagonal disks sandwiched between two parallel plates under vertical vibrations against gravity tend to assemble themselves into a state with positional but without orientational order, reminiscent to plastic crystals composed of hard polyhedra (in three dimensions) or polygonal disks (in two dimensions) [25, 26]. As any 'macroscopic' collective behavior arises from the mobility of individual building blocks as well as the interactions between them, we focus here on the dynamics of a single polygonal disk under vertical vibrations. In particular, we investigate how a

change of particle shape and confinement influences its motion in both translational and rotational degrees of freedom as well as the coupling in between.

2. Methods

Side and top views of the experimental setup are sketched in figures 1(a) and (b) respectively. N regular n-gon disks ($3 \leqslant n \leqslant 8$ as shown in figure 1(d)) of incircle diameter D and height h are confined to a cylindrical container of height H and diameter $2R$. The horizontally aligned container is observed from above and vibrated against gravity g. It is driven sinusoidally using an electromagnetic vibrator (Tira TV50350). The dimensionless acceleration $\Gamma = (2\pi f)^2 z_0/g$ with frequency f and amplitude z_0 is controlled via a function generator (Agilent FG33220) and an accelerometer (Dytran 3035B2). The bottom and lid of the container are made from 1 cm thick polycarbonate (Bayer Makrolon) to provide uniform driving. The disks are cut from brass (CuZn39Pb5, density $\varrho = 8.5$ g cm^{-3}) and have a central circular hole of diameter d, to facilitate fast and precise detection of particle location even in the case of close packing. The triggering of the camera (Lumenera Lt425M and IDT MotionScope M3) is synchronized to the driving, as is the stroboscopic LED background illumination used to achieve high contrast (see [10, 27] for additional details).

The captured raw images are subjected to image analysis. Figure 1(c) shows a sample image after background removal with particle position and orientation marked. The image analysis procedure is split in two steps, finding the particle center (x- and y-coordinate) followed by determining its orientation Ψ. For the rest of this investigation we focus on single particle dynamics. Therefore we place in the container only a single disk ($N = 1$) or very few disks ($N = 8$ to 16) sufficiently apart from each other to avoid interactions, confine them horizontally to the field of view of the camera (5 cm $\times$ 5 cm) using black electrostatic discharge foam and make sure there is no influence from the boundary.

For finding the particle center, the rotational symmetry of the central drilling is exploited. For particles lying flat on the imaging plane, finding their centers translates to finding the centers of circles with diameter d in the image. While agitated, the particles can tilt slightly. In the background-illuminated image the hole's edges become two ellipse arcs, which are slightly shifted towards each other. As the particles have a finite height h, the vertical confinement H limits the maximum tilting angle, e.g. for a disk of circular or n-gon shape with even n, to

$$\theta_{\max} = 2 \cdot \arctan\left[\left(D - \sqrt{D^2 + h^2 - H^2}\right)/(h + H)\right]. \tag{1}$$

Consequently, the maximum distortion from a circle (in radial direction) is within 7% of its radius in the worst case of the experiments presented here and can be ignored. Finding the centers of circles can be achieved efficiently using the circle Hough transformation [28–30]. The required processing time can become independent of the input image complexity (e.g., number of particle edge pixels) if convolutional approaches are used [31].

The Canny edge filter [32] is used to detect particle contours. As it is a non-linear edge filter, it can not be combined with the radius search to a single convolution kernel as proposed in [31]. However, the advantage of the Canny edge filter is that it avoids cancellation of votes in the Hough accumulator[3], and thus enables accurate measurement of disk position with subpixel resolution.

The binary edge image is subsequently convolved with a truncated Hough cone consisting of blurred circles of different radii $\tilde{r}$ close to the expected value of $d/2$. In polar coordinates (r, φ), the density of Hough votes can be written as $W \cdot \frac{1}{r} \cdot \exp\left(-\frac{(r-\tilde{r})^2}{2\,\sigma^2}\right)$, where $\sigma = 0.5$px sets the amount of blurring to accomodate discrete sampling and $W = 3/[2 + \max(d/2 - 1\text{px}, \tilde{r})/\tilde{r}]$ is an empirical prefactor as a penalty to circles smaller than the expected ones.

The Hough accumulator resulting from the convolution is then searched for the N highest isolated peaks, where N is the known number of particles to be found. To speed up this search, values smaller than a dynamically adjusted limit are thresholded to zero, making the Hough accumulator sparse. After sorting, it is traversed descendingly and the locations of the N highest *isolated* peaks are found. The first entry of the sorted list (a global maximum) is called *isolated* by definition. Subsequently peaks are isolated by ignoring Hough space entries within a threshold distance r_p to *isolated* peaks, until N center locations are found.

As the last step of locating the particles, subpixel refinement is performed for each identified particle position. The subpixel shift Δ of the peak location along the x-, y- and r-axis of the Hough accumulator is estimated with $\Delta = 0.5\,\text{px} - \tilde{\sigma}^2/1\,\text{px} \cdot \ln(p/q)$, where p is the value of an isolated peak and q its highest

[3] Note that cancellation of votes in the Hough accumulator is a problem inherent to all linear edge filters, making *accurate* parameter estimation infeasible.

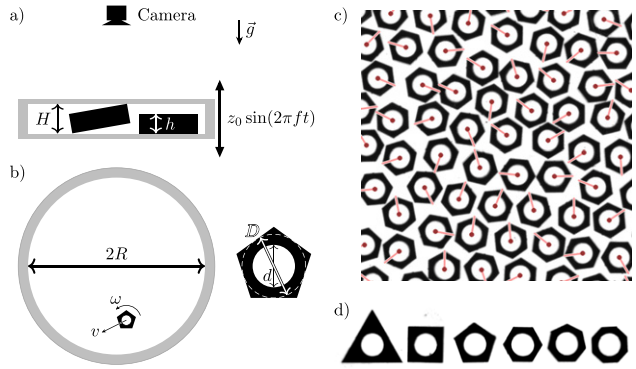

Figure 1. (a) Sketch of the set-up with various definitions (see text for details) in side and (b) top view. (c) Zoom-in view of an image after background removal with markers showing the position and orientation of individual disks, obtained with image analysis. (d) n-polygon particles with $3 \leqslant n \leqslant 8$ but the same incircle diameter $D = 6$ mm and height $h = 2$ mm.

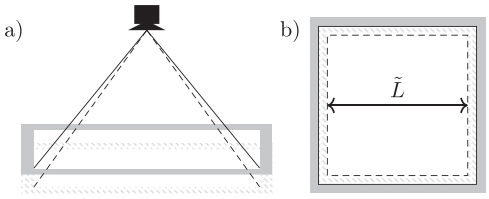

Figure 2. Determination of the vertical position of the container using a top view camera.

neighbor along the corresponding axis. The shape of the peak is assumed to be a Gaussian of width $\tilde{\sigma} = 2\sigma$ for x and y and $\tilde{\sigma} = 2\sqrt{2}\sigma$ for r respectively.

For determining the orientation of each particle, a Fourier analysis of its outer contour is performed. Here, the longest contour C of the binary edge image within a circular mask of inner radius r_i and outer radius r_o (with the particle center as origin) is transformed to polar coordinates (r, φ). $C(r, \varphi)$ is approximated using the 0th, 1st, 2nd and nth Fourier mode, corresponding to the mean radius of the contour, a shift of the detected center with respect to the outer contour, a tilting of the particle, and the corners or the particle respectively. The phase angle of the nth Fourier mode of $C(r, \varphi)$ indicates (modulo $2\pi/n$) the desired orientation Ψ of the regular n-gon.

As sketched in figure 2(a), the viewing angle of the container bottom varies with its vertical position. Stepping further than a previous investigation [33], we obtain the third-dimensional information quantitatively from the top view images. The apparent length $\tilde{L}$ in the top view image figure 2(b) changes slightly when using a conventional entocentric lens. By tracing the positions of two fixed segments of the container wall with subpixel resolution, we obtain the relative vertical position of the container, which is subsequently scaled to an absolute vertical displacement using the accelerometer reading. As illustrated below in section 5, a spatial resolution down to a few hundredths of a pixel can be achieved.

Finally, the particle motion is traced based on the image analysis results, assuming every particle moves to the closest position of a particle in the next frame. This assumption is checked for plausibility by verifying that the mapping between particles in two consequent frames is always bijective. After identifying the same particle in consequent frames, its orientation is traced, assuming that the sampling rate fulfills the Nyquist criterion. This assumption is reasonable as the change of orientation between two consequent frames is typically more than an order of magnitude smaller than $2\pi/n$.

3. Coupling between translational and rotational motion

Based on the tracing results, the average velocity between two consecutive frames is obtained. Figure 3 shows scatter plots of angular ω vs translational v velocities of the particle center for $n = 6$ and 5. These plots are representative for all results obtained with an even or odd number of corners explored here. For polygonal particles with even n, three clusters of points (cf figure 3(a)) whereas for odd n only two distinct clusters are found (cf figure 3(b)). We note that in both cases the position, shape and density of the clusters are symmetric with respect to zero on the ω axis. This suggests that the rotation mechanism has no

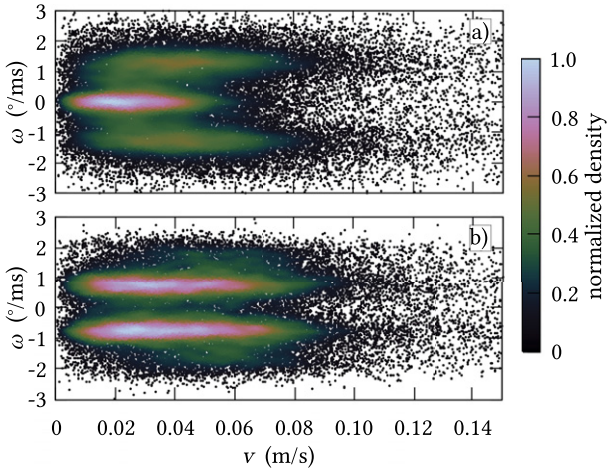

Figure 3. Scatter plot of the angular velocity ω with respect to the particle's center vs its horizontal velocity v obtained from consequent top view images sampled at a rate of 1000 Hz over 45 s for a single (a) hexagonal ($n = 6, N = 10$) and (b) pentagonal ($n = 5, N = 12$) disk. Parameters: $f = 50$ Hz, $\Gamma = 7$, $H = 3.9$ mm, $h = 2$ mm, $D = 6$ mm. The color code corresponds to the local area density of data-points obtained with a Gaussian kernel density estimator using the bandwidths 2.9 mm s^{-1} and 0.073° m s^{-1} in (a) and 2.4 mm s^{-1} and 0.06° m s^{-1} in (b).

preferential direction so that clockwise and counterclockwise rotation have equal likelihood. For even n (cf figure 3(a)), the central cluster around $\omega = 0$ is typically very prominent and represents a clapping motion (clattering mode) of the disk [34]. For off-centered clusters, the typical translational velocity lies significantly higher than for the clapping motion. This suggests that disks in different rotational modes, i.e. clattering or precessing, tends to have different v, indicating a coupling between rotational and translational DoF. For odd n (cf figure 3(b)), only the two off-centered clusters are found, meaning that polygons with odd n have a significantly higher tendency to precess than with even n. This can be easily understood, as for odd n each side of the polygon faces a corner on the opposite side, so that small perturbations due to roughness quickly make the clapping motion unstable.

The position of the clusters changes with the confinement and particle shape. The translational velocity distribution is investigated in detail in appendix A where we show that at timescales longer than half a vibration period the particle effectively diffuses in the lateral direction. In the following section we concentrate on the rotational motion for a quantitative analysis.

4. Characteristic angular velocities

Figure 4 shows the probability density P_ω of the angular velocity ω for the same parameters as in figure 3. For the hexagonal disk (cf figure 4(a)) the distribution shows three peaks and can be described fairly well by a sum of three Gaussian distributions $\mathcal{N}$ symmetrically arranged around $\omega = 0$:

$$\omega \sim \sum_{k=-1}^{1} \mathcal{N}(k\,\omega_\mathrm{r}, \sigma_k) \cdot p_k, \tag{2}$$

where ω_r is the characteristic angular velocity to be obtained. During fitting we fix $\sigma_{-1} = \sigma_{+1}$ as the variations in ω do not appear to depend on its sign. We allow $p_{-1} \neq p_{+1}$ due to the finite observation period. For the central peak around $\omega = 0$ only the standard deviation σ_0 is fitted as $p_0 = 1 - p_{-1} - p_{+1}$ is fixed due to the normalization of P_ω. By fitting the remaining five free parameters (ω_r, σ_0, σ_{+1}, p_{-1}, p_{+1}), the characteristic angular velocity ω_r is determined. Its dependence on the confinement is discussed below.

In the case of the pentagonal disk (cf figure 4(b)), two additional Gaussians around $\pm 2\omega_\mathrm{r}$ have to be added for a reasonable fit:

$$\omega \sim \sum_{k=-2}^{2} \mathcal{N}(k\,\omega_\mathrm{r}, \sigma_k) \cdot p_k. \tag{3}$$

Remarkably, we find that the peaks at $2\omega_\mathrm{r}$ have in good approximation the doubled width of the inner ones and appear to have the same relative probabilities. By exploiting this observation, we reduce the number of degrees of freedom without decreasing the quality of the fit visibly. More precisely, by fixing $p_{+2}/p_{-2} = p_{+1}/p_{-1}$ and prescribing $\sigma_{+2} = \sigma_{-2} = 2\sigma_{+1} = 2\sigma_{-1}$ only a single additional degree of freedom, p_{+2}, is added. The presence of two peaks per side suggests that there exist different ways of injecting energy

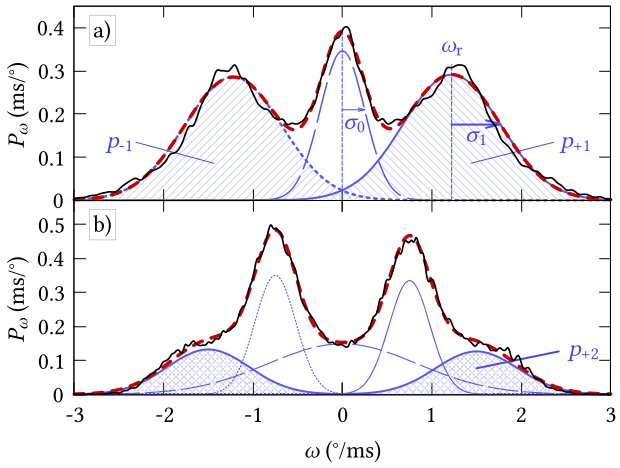

Figure 4. Kernel density estimate (black solid line) for the probability density P_ω of the angular velocity ω of the (a) hexagonal and (b) pentagonal disk shown in figure 3. Fit (red dashed line) with a summation of three (a) and five (b) symmetrically arranged normal distributions (see equation (2) and equation (3) for more details). Parameters used for fitting are sketched in blue. The Gaussian kernel's bandwidth is chosen optimally using the improved Sheather-Jones algorithm [35] to 0.030° m s^{-1} and 0.019° m s^{-1} respectively.

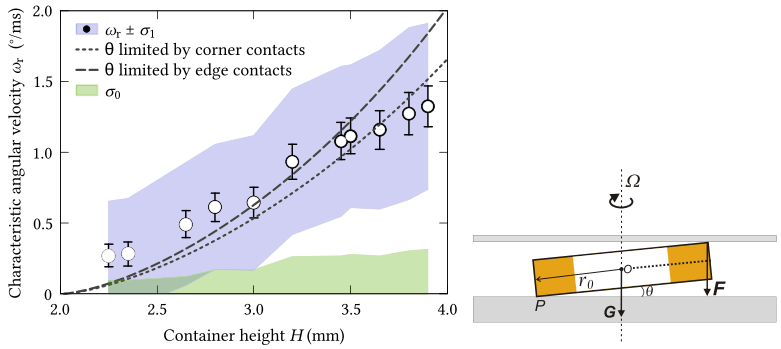

Figure 5. Left: dependency of a hexagonal particle's characteristic angular velocity ω_r on the vertical confinement H, compared to equation (5) with different restrictions for θ. $N = 1$, other experimental parameters are the same as in figure 3(a). Shaded regions indicate the standard deviation σ_i of the corresponding normal distributions of ω shown in figure 4(a) for rotating (blue) and clapping (green) motion. The uncertainty of ω_r is estimated from σ_1 assuming independent measurements after 100 vibration cycles. The ratio of the inner and outer radius of the data points, indicated by the thickness of the data points, corresponds to the probability for the particle to be classified as precessing according to the fit illustrated in figure 4. Right: side view of a polygonal disk with various definitions.

into the rotational DoF. Note that the second peak arises not only for disks with odd number of edges as it is also observed for $n = 4$. In general this feature appears to be more prominent for lower n. For instance, the ratio p_{+2}/p_{+1} for $n = 6$ is an order of magnitude smaller than in the case of $n = 5$.

Based on ω_r obtained in figure 4(a), we explore systematically the influence of confinement H on particle mobility. As shown in figure 5, the angular velocity increases monotonically with H. This is in agreement with a model considering that rotation arises predominately from the precession of the disk ([14], and references therein).

More specifically, the model considers a circular disk (i.e., the case of $n \to \infty$) with a radius of r_0 and height h. Similar to a coin spinning on a rigid surface, there exists a coupling between precession and rotation for the case of rolling without sliding. As the contact point of the disk draws a circle of radius $r_c < r_0$, the disk rolls actually over a distance larger than $2\pi r_c$ during one precession period $1/\Omega$. With a certain confinement H, the maximum tilting angle is limited by θ_{max} of equation (1) with $D = 2r_0$. The model assumes $\theta = \theta_{max}$ and therefore the angular velocity varies with confinement H. In addition to the influence of gravity, as considered in existing literature, see e.g. [36–38], here the additional influence from the vibrating plate (e.g., torque induced by the force F for the case of colliding with the container lid) has to be considered. Consequently, the precession rate can be estimated with [14]:

$$\Omega = \sqrt{\frac{Gr_0(1+2\Gamma)}{I_{r,P}\ \sin\ \theta}}, \tag{4}$$

where G is the gravity of the disk, Γ is the maximum dimensionless acceleration and $I_{\mathrm{r,P}}$ is the moment of inertia along the radial direction passing through contact point P. Here, the value for a regular n-gon disk is used, $I_{\mathrm{r,P}} = \varrho h \left[\frac{n}{64} D^4 \left(\cos\frac{\pi}{n}\right)^{-2} \left(1 - \frac{2}{3}\sin^2\frac{\pi}{n}\right) \tan\frac{\pi}{n} - \frac{\pi}{64} d^4 + \frac{h^2}{12}\left(nD^2 \tan\frac{\pi}{n} - \pi d^2\right)\right]$. It is calculated by considering n isosceles triangles, subtracting the circular hole, taking advantage of the perpendicular axis theorem and using the parallel axis theorem when integrating along the third dimension [39]. To match the experimental conditions, we use the parameters for the hexagonal disk ($n = 6$, $h = 2$ mm, $D = 6$ mm, $d = 2$ mm) to estimate the characteristic rotation speed of the disk viewed from top using

$$\omega_{\mathrm{r}} = (1/\cos\ \theta - 1)\Omega\,. \tag{5}$$

Figure 5 compares the experimental data to this precession model using the largest value of θ compatible with corner contacts (dotted line) and edge contacts (dashed line) at bottom and lid.

In reality, the rolling motion of the disk is always accompanied with energy dissipation arising from air drag, sliding, rolling friction, etc. The frequent collisions between the disk and the vibrating plates also lead to frequent detachment between the disk and the container. Although the simplified model does not consider the details described above, it provides nevertheless a reasonable estimation of the characteristic angular velocity ω_{r} and its dependence on H without any fit parameters, as shown in figure 5.

The fraction of time spent by the particle in different modes of motion is captured by the coefficients p_k in equations (2) and (3). The hexagonal particle is classified as precessing 98 [4] to 72 percent of the time as H grows (see figure 5). For $H < 2.8$ mm the shaded areas indicate that σ_0 and σ_1 overlap at least partially. This could give a hint why ω_{r} seems to be systematically overestimated for low confinement heights compared to the model: as ω_{r} is extracted from 'shoulders' of a central clattering mode, a lower signal-to-noise ratio has to be expected here than for high H where the modes are clearly separable.

5. Energy fluctuations within one vibration cycle

In order to investigate the dynamics within one vibration period $T_0 = f^{-1}$ we average the kinetic energy at fixed phase over more than 2200 vibration periods, which is shown in figure 6. Note that a sufficient sampling rate is needed for the following analysis, as the translational velocity distribution can be qualitatively different if the sampling rate is reduced, as shown in appendix A.

The upper panel of figure 6 compares the vertical position of the container during one vibration cycle to the induced sinusoidal vibration and shows an excellent agreement for all H. Even though the apparent container size varies only by less than 1.2px, the total harmonic distortion of the signal as defined in [40] is $\mathrm{THD_R} = 4(2)\%$.

The lower panel of figure 6 shows the fluctuations of the kinetic energy of a hexagonal disk within one vibration period for different vertical confinement H. Here, only the lateral movement and rotation in the container plane (as detected by the top view camera) are considered. The squares and filled circles break down the translational and rotational contributions to the kinetic energy, $E_{\mathrm{kin,lat}} = m\,v^2/2$ and $E_{\mathrm{kin,rot}} = I_n\omega^2/2$ respectively, where $I_n = \varrho h \left[\frac{n}{32} D^4 \tan\frac{\pi}{n}\left(\cos\frac{\pi}{n}\right)^{-2}\left(1 - \frac{2}{3}\sin^2\frac{\pi}{n}\right) - \frac{\pi}{32} d^4\right]$ denotes the moment of inertia of the $n-$gon particle with respect to its symmetry axis. The thickness of the solid lines indicates the respective standard error assuming statistical independence of the consecutive vibration periods used for averaging, which is justified according to the following analysis in section 6.

For all confinement heights H, $E_{\mathrm{kin,rot}}$ shows two peaks per vibration period, suggesting that both collisions with the lid and with the container bottom lead to a similar kinetic energy injection into the rotational DoF. The average value of $E_{\mathrm{kin,rot}}$ rises continuously with increasing H in agreement with the growth of ω_{r} predicted by the model, although the probability for the disk to precess decreases as H grows (see the change of data point thickness in figure 5).

In contrast, the lateral translational kinetic energy $E_{\mathrm{kin,lat}}$ shows a qualitatively different behavior: The peak in the second half of a vibration period is clearly suppressed as H decreases. In the case of $H < 3.2$ mm, only one peak can be clearly distinguished. This qualitative difference arises presumably from the way of energy injection: Torque induced precession always leads to rotation upon collisions with the container, while force applied vertically on the tips or edges of the disk will not necessarily lead to translational motion in the horizontal direction.

Remarkably, as H decreases, there is a tendency for $E_{\mathrm{kin,lat}}$ and $E_{\mathrm{kin,rot}}$ in the observed DoF (i. e., two translational DoF perpendicular to $\boldsymbol{g}$ and one rotational DoF around $\boldsymbol{g}$) to overlap with each other in the

[4] This corresponds to the two lowest confinement heights where the standard deviations of the clockwise and the counterclockwise precession mode overlap each other significantly, impacting the reliability of the classification.

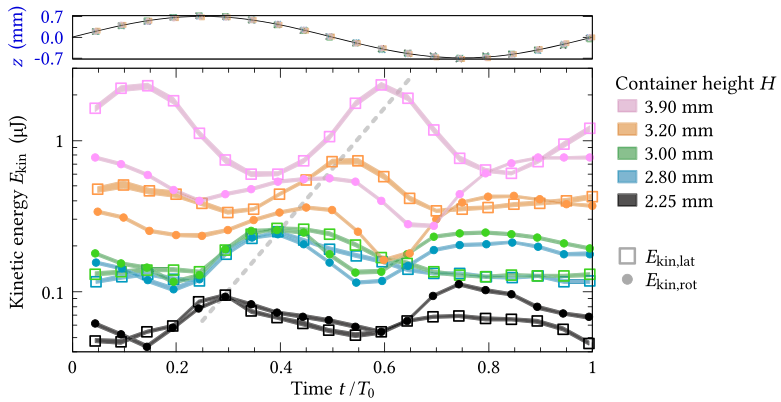

Figure 6. Top: vertical position z of the container within one vibration cycle obtained from top view images. Bottom: average lateral translational $E_{kin,lat}$ (□) and rotational kinetic energy $E_{kin,rot}$ (●) of the hexagonal disk of figure 5 within one vibration cycle for various confinement H. The gray dashed line is a guide to the eyes highlighting the phase-shift of the maximum kinetic energy.

first half of the vibration cycle. Note that this is different from a previous observation of vibrofluidized granular rods under microgravity condition [41], where the kinetic energy in one translational DoF and two observed rotational DoF was found to be equal with each other. The mechanism behind such apparent 'equipartition' deserves further investigation in the future as it helps constructing nonequilibrium model systems with granular particles. However, we find $E_{kin,lat} < E_{kin,rot}$ in the second vibration half period. Furthermore, these differences within one vibration period apparently disappear abruptly for larger H. For $H \geqslant 3.2$ mm, $E_{kin,lat}$ exceeds $E_{kin,rot}$ by more than a factor of two on average. Note that the relative amount of energy injection into the different DoF changes with H, as the vertical confinement drives rotation arising from precession and yet tends to hinder a horizontal translation of the vibrated particle.

Finally, the phase-shift of the maximum for each kinetic energy contribution when changing H constitutes another prominent feature in figure 6, as highlighted by the gray dashed line. With increasing H the maxima shift to later times. This trend is expected as the traveling distance of a disk from container bottom to the lid (and vice versa) increases. The phase-shift applies to both rotational and translational DoF, as they are coupled with each other. For small H, the first peak for the kinetic energy of either translational or rotational DoF overlaps with each other. For $H \geqslant 3.2$ mm, the peak of $E_{kin,lat}$ lags slightly behind $E_{kin,rot}$. Such a difference suggests that the coupling between different DoF as well as the distribution of energy injection can be tuned by confinement. This abrupt phase-shift tuned by H and the related transition between different coupling modes is further illustrated by means of the cross-correlation function in appendix B.

In short, the above analysis suggests that confinement plays an essential role in determining the distribution of energy injection in different DoF as well as coupling in between.

6. Shape tuned 'memory' effect

Finally, we address the influence of n on the 'memory' of the system, which is characterized by the autocorrelation function. After collision, the disk tends to keep its motion, i.e., retains a certain level of 'memory', while frequent collisions with the container lead to the loss of 'memory'. Using autocorrelation functions of the disk motion in both DoF, we analyze the influence of particle shape on this effect.

Figure 7 compares the autocorrelations $r_{v,v}$, $r_{\omega,\omega}$ and $r_{|\omega|,|\omega|}$ of the lateral velocity v, the angular velocity ω and its absolute value $|\omega|$ respectively for two different container heights H in the case of a pentagonal disk. In alignment with the periodicity of lateral velocity shown in figure 6 for a hexagonal disk, $r_{v,v}$ peaks at multiples of T_0 and $T_0/2$ for the case of $H = 3$ mm and 3.9 mm, respectively, suggesting the influence of collisions with container bottom and lid. For low H, the autocorrelation of the absolute angular velocity $r_{|\omega|,|\omega|}$ also oscillates around zero, showing clearly a periodic behavior. This is not surprising as both DoF are coupled with each other. As H increases, the magnitude of the peaks for $r_{v,v}$ drop dramatically, suggesting a stronger influence from the randomness due to strong impacts with the container. Note that different H leads to different modes. For the signed value of the angular velocity (instead of its absolute value), the autocorrelation function shows a clearly different trend. No clear periodicity can be found and $r_{\omega,\omega}$ decays exponentially, as shown in the insets of figure 7.

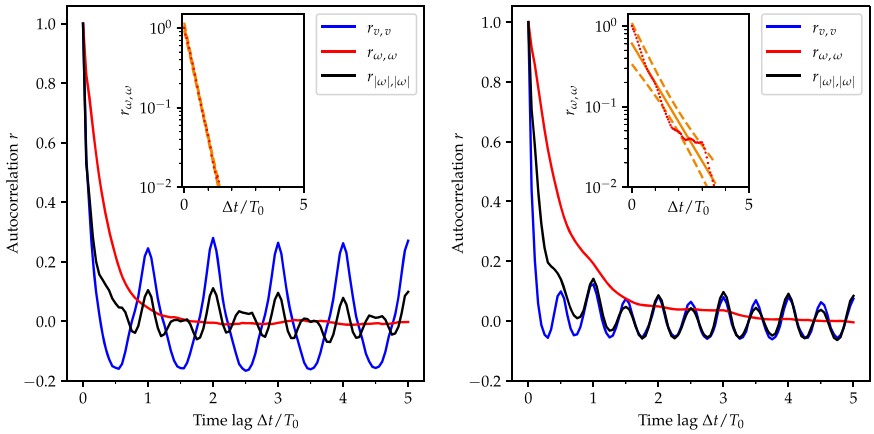

Figure 7. Normalized autocorrelation of velocity v (blue), angular velocity ω (red) and its absolute value $|\omega|$ (black) of a pentagonal disk ($n = 5$) for $H = 3$ mm (left) and $H = 3.9$ mm (right). Other experimental parameters are the same as in figure 3(b). The insets highlight the exponential decay of the autocorrelation function of ω. The decay time is extracted by fitting a straight line (orange), the dashed lines indicate the uncertainty.

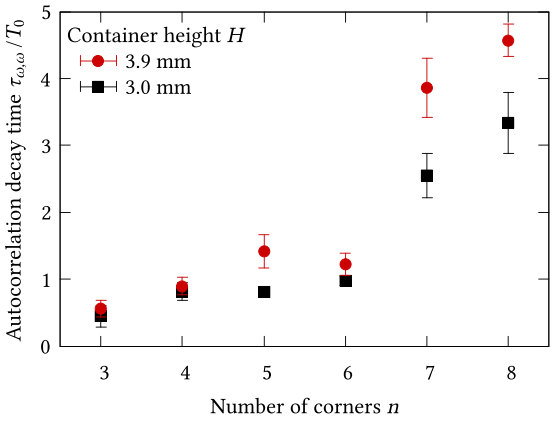

Figure 8. Decay time of the angular velocity autocorrelation function at various n for two container heights. $N = 8, 12, 12, 10, 16, 16$ for $n = 3, 4, 5, 6, 7, 8$ respectively. Other parameters are the same as in figure 7.

As shown in figure 4, the disk may rotate in either direction with the same probability. Qualitatively speaking, the change of r due to $|.|$ suggests a frequent change of rotations due to collision. The periodicity of driving becomes visible when considering the kinetic energy scale or absolute value of the angular velocity. The fact that $r_{\omega,\omega}$ does not show a clearly periodic behavior suggests that change of rotation speed (i.e., torque applied while colliding) itself tends to persist after collision. This provides an opportunity for us to quantitatively investigate the 'memory' carried by the agitated disk through the characteristic decay time $\tau_{\omega,\omega}$, which is defined as the time scale for $r_{\omega,\omega}$, to decay from 1 to e^{-1}.

Figure 8 plots the decay time for various n and two different H. In comparison to confinement, the number of corners has the more dramatic effect on the 'memory' of the disk: the closer the disk shape is to a circle, the longer the autocorrelation decay time. Qualitatively, this can be understood as the chance for a disk to keep its rotation increases as n increases, as the corresponding potential energy barrier is smaller. Quantitatively, the decay time tends to stay within one vibration period for $n \leqslant 6$, meaning that the 'memory' is lost after each vibration cycle, and the influence from H is weak. This suggests that samples collected at a rate lower than the driving frequency can be considered independent of each other. As $n = 7$ or higher (the disk shape getting closer to a circle), the decay time grows monotonically and the influence from H becomes prominent, suggesting a higher probability for persistent rotation.

7. Conclusions and outlook

To summarize, we characterize systematically the influence of confinement (i.e., height of the container) and shape on the motion of a single regular n-gon disk in both translational and rotational degrees of freedom under vibrations. Generally speaking, a vibrated polygonal disk tends to rotate due to precession

induced by gravity as well as collisions with the container and the rotation speed is tuned by the confinement height H. For a disk with even number of edges, there exists an additional clattering mode with zero angular velocity.

By means of circular Hough transformation and Fourier analysis of the contour, we analyze the coupling between rotational and translational degrees of freedom of the polygonal disk quantitatively and find that the probability for a disk to rotate can be decomposed into symmetrically arranged normal distributions peaked at a characteristic angular velocity.

In order to explore particle motion within one vibration cycle, we develop an algorithm that can successfully obtain the container position from tiny changes (1.2 pixel) of the container's width upon vibration along the viewing direction. Consequent analysis on the kinetic energy fluctuations within one vibration period shows a clear dependence on the confinement and a tendency of equal energy distribution in both observable DoF at small confinement.

The time scale associated with the dynamics of the disks is characterized by means of the autocorrelation function. We find that the decay time of $r_{\omega,\omega}$ increases monotonically with n. The fact that it becomes smaller than the vibration period for $n \leqslant 6$ indicates the loss of 'memory' in rotational DoF and consequently velocities sampled once per vibration period can be considered as independent of each other.

In the future, a more quantitative understanding of the critical confinement and influence of edge number is needed, as the two control parameters provide a pathway to design preferred trajectories of individual polygonal disks as well as the kinetic energy input into different DoF. Note that an assembly of granular 'walkers' with equipartition of energy injection could serve as a perfect model system for extending statistical mechanics tools to investigate widespread active matter.

Acknowledgments

We are grateful to Manuel Baur for his preliminary work on the experimental setup and to Klaus Ötter for technical support. Inspiring discussions with Ingo Rehberg and Valentin Dichtl are gratefully acknowledged. This work is supported by the Deutsche Forschungsgemeinschaft through Grant no HU1939/4-1. This publication was funded by the German Research Foundation (DFG) and the University of Bayreuth in the funding programme Open Access Publishing.

Appendix A. Translational velocity distribution

Figure A1 shows a comparison of the lateral velocity distribution obtained with different sampling rates; twice (black) or 20 times (red) per vibration period (the same as in figure 3).

The outer panels display the distributions as probability densities P_v, estimated using a Gaussian kernel density estimator of variable bandwith [42]. The limited support due to $v > 0$ is accounted for using the reflection method [43]. The hyperparameter is optimized using leave-one-out maximum-likelihood cross-validation [44, 45]. The shift towards lower velocities for the lower sampling rate is very prominent. When sampling ten times as often, the mean of the distribution differs by a factor of 2.2 for both the hexagonal (figure A1(a)) and the pentagonal (figure A1(b)) disk. The lower mean for rarer sampling confirms that the disks change the direction of their translational motion within the timeframe of half a vibration period.

The insets show the corresponding cumulative distribution function $F(x) = \int_{-\infty}^{x} P(x')\mathrm{d}x'$ to avoid any visualization parameters. Here, the tail of the distribution is highlighted by plotting the empirical complementary cumulative distribution function $1 - F_{v^2}$ on a logarithmic axis. As the black curve is close to a straight line, the coarser sampled lateral velocity distribution is close to the Maxwell–Boltzmann distribution in two dimensions. The particle thus effectively diffuses in the lateral direction at long timescales. This is reminiscent of the rotational random walk found in [14] and raises the question to which extend random motion in the rotational and translational DoF are coupled. The velocity fluctuations within one vibration cycle are discussed in more detail in section 5.

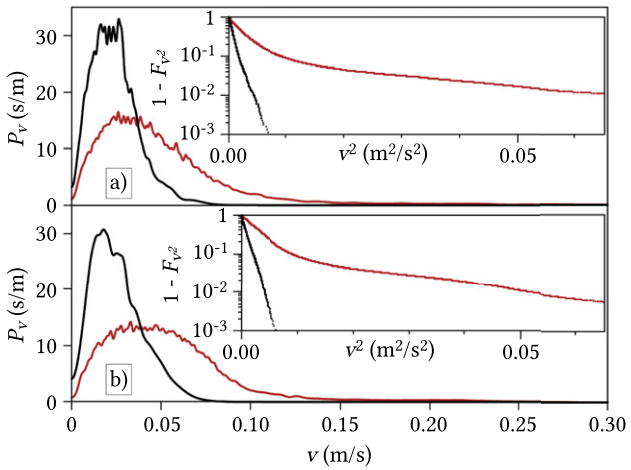

Figure A1. Horizontal velocity distribution for the (a) hexagonal and (b) pentagonal disk when sampling the particle position 20 times per vibration cycle (red), or two times per vibration cycle (black). Other parameters are the same as in figure 3. Note that sampling 20 times per vibration cycle corresponds to 1000 Hz as previously. Outer panels: probability density P_v estimated using the optimal Gaussian kernel density estimator of variable bandwith (see text for details). Insets: complementary cumulative distribution function of the squared velocity.

Appendix B. Confinement controlled coupling

The coupling between translational and rotational DoF is characterized using the zero mean normalized cross-correlation of v^2 and ω^2, shown in figure B1 for different H with the time lag Δt in units of T_0. For better visibility of the underlying structure, bilinear interpolation is used between the sampling points.

For all container heights H, the cross-correlation peaks at zero time lag and shows a regular pattern otherwise. The global maximum at $\Delta t = 0$ indicates an overall in phase coupling between rotation and translation. However, as all aperiodic contributions accumulate in this central peak (similarly to the noise-polluted zero time lag peak in autocorrelations), the periodic response of the system should be instead inferred from the off-center maxima. Their distance of $T_0/2$ indicates collisions with both lid and bottom in a similar manner (for at least one of v or ω), as also indicated in figure 6. For $H < 3.0$ mm, the off-center maxima occur at integer multiples of $T_0/2$, indicating zero phase-shift between rotation and translation for the periodic response of the system, which we call synchronous mode. For $H > 3.0$ mm, the off-center maxima are shifted. Here, rotation precedes the translation by roughly $T_0/8$, giving rise to the asynchronous mode. Taking into account that, according to figure 6, v^2 and ω^2 peak twice per vibration period T_0 we observe a phase-shift close to 90° between the two contributions to the total kinetic energy here.

For the case of rolling without sliding, rotation of an Euler's disk is expected to be coupled to the center of mass movement and consequently the kinetic energy in the translational DoF. This expectation is compatible with our observations for small container heights. At $H \approx 3.0$ mm however, the coupling between rotation and translation changes fundamentally, leading to the transition into the asynchronous mode. Note that the phase lag between v^2 and ω^2 as a function of H exhibits a stepwise dependence, reminiscent of the scenario of forced oscillation with a driving dependent phase-shift.

The characterization of the cross-correlation function r_{v^2,ω^2} indicates that, depending on confinement, there exists an abrupt transition from the 'synchronous' mode where the energy peaks of the translational and rotational motion are at the same phase to the 'asynchronous' mode where a phase-shift between different DoF arises.

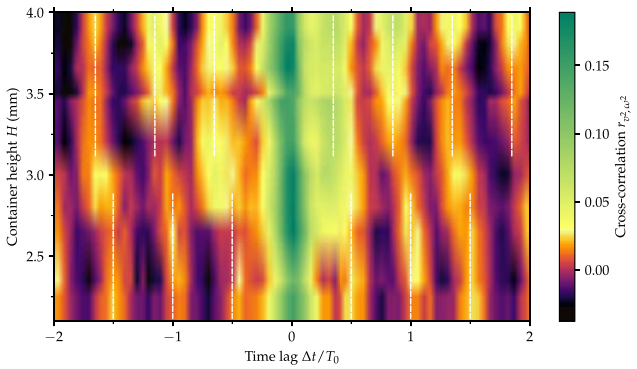

Figure B1. Normalized cross-correlation of lateral translational and rotational contributions to the kinetic energy for the same experimental parameters as in figure 5. The white dashed lines are guides to the eyes highlighting the location of off-center maxima of the cross-correlation for low and high container heights H.

ORCID iDs

Simeon Völkel https://orcid.org/0000-0002-0036-0394
Kai Huang https://orcid.org/0000-0003-0652-713X

References

[1] Tufillaro N and Abbott T 1992 *An Experimental Approach to Nonlinear Dynamics and Chaos* (Reading MA: Addison-Wesley)
[2] Tufillaro N B and Albano A M 1986 Chaotic dynamics of a bouncing ball *Am. J. Phys.* **54** 939–44
[3] Dorbolo S, Volfson D, Tsimring L and Kudrolli A 2005 Dynamics of a bouncing dimer *Phys. Rev. Lett.* **95** 044101
[4] Dorbolo S, Ludewig F and Vandewalle N 2009 Bouncing trimer: a random self-propelled particle, chaos and periodical motions *New J. Phys.* **11** 033016
[5] Wang J, Liu C, Jia Y B and Ma D 2014 Ratchet rotation of a 3D dimer on a vibrating plate *Eur. Phys. J.* E **37** 1
[6] Kudrolli A, Lumay G, Volfson D and Tsimring L S 2008 Swarming and swirling in self-propelled polar granular rods *Phys. Rev. Lett.* **100** 058001
[7] Deseigne J, Dauchot O and Chaté H 2010 Collective motion of vibrated polar disks *Phys. Rev. Lett.* **105** 098001
[8] Yadav V, Chastaing J Y and Kudrolli A 2013 Effect of aspect ratio on the development of order in vibrated granular rods *Phys. Rev.* E **88** 052203
[9] Altshuler E, Pastor J M, Garcimartín A, Zuriguel I and Maza D 2013 Vibrot, a simple device for the conversion of vibration into rotation mediated by friction: preliminary evaluation *PLoS One* **8** e67838
[10] Müller T, de las Heras D, Rehberg I and Huang K 2015 Ordering in granular-rod monolayers driven far from thermodynamic equilibrium *Phys. Rev.* E **91** 062207
[11] Walsh L and Menon N 2016 Ordering and dynamics of vibrated hard squares *J. Stat. Mech.* **2016** 083302
[12] Scholz C, D'Silva S and Pöschel T 2016 Ratcheting and tumbling motion of vibrots *New J. Phys.* **18** 123001
[13] Tsai J C, Ye F, Rodriguez J, Gollub J P and Lubensky T C 2005 A chiral granular gas *Phys. Rev. Lett.* **94** 214301
[14] Baur M and Huang K 2017 Dynamics of wet granular hexagons *Phys. Rev.* E **95** 030901
[15] Takatori S, Baba H, Ichino T, Shew C Y and Yoshikawa K 2018 Cooperative standing-horizontal-standing reentrant transition for numerous solid particles under external vibration *Sci. Rep.* **8** 437
[16] Ramaswamy S 2010 The mechanics and statistics of active matter *Annu. Rev. Condens. Matter Phys.* **1** 323–45
[17] Vicsek T and Zafeiris A 2012 Collective motion *Phys. Rep.* **517** 71–140
[18] Marchetti M C, Joanny J F, Ramaswamy S, Liverpool T B, Prost J, Rao M and Simha R A 2013 Hydrodynamics of soft active matter *Rev. Mod. Phys.* **85** 1143–89
[19] Olafsen J S and Urbach J S 2005 Two-dimensional melting far from equilibrium in a granular monolayer *Phys. Rev. Lett.* **95** 098002
[20] Reis P M, Ingale R A and Shattuck M D 2006 Crystallization of a quasi-two-dimensional granular fluid *Phys. Rev. Lett.* **96** 258001
[21] Eshuis P, van der Weele K, van der Meer D, Bos R and Lohse D 2007 Phase diagram of vertically shaken granular matter *Phys. Fluids* **19** 123301
[22] Huang K, Roeller K and Herminghaus S 2009 Universal and non-universal aspects of wet granular matter under vertical vibrations *Eur. Phys. J. Spec. Top.* **179** 25–32
[23] May C, Wild M, Rehberg I and Huang K 2013 Analog of surface melting in a macroscopic nonequilibrium system *Phys. Rev.* E **88** 062201
[24] Huang K 2015 $1/f$ noise on the brink of wet granular melting *New J. Phys.* **17** 083055
[25] Damasceno P F, Engel M and Glotzer S C 2012 Predictive self-assembly of polyhedra into complex structures *Science* **337** 453–7
[26] Anderson J A, Antonaglia J, Millan J A, Engel M and Glotzer S C 2017 Shape and symmetry determine two-dimensional melting transitions of hard regular polygons *Phys. Rev.* X **7** 021001
[27] Butzhammer L, Völkel S, Rehberg I and Huang K 2015 Pattern formation in wet granular matter under vertical vibrations *Phys. Rev.* E **92** 012202
[28] Hough P V C 1962 Method and means for recognizing complex patterns *US Patent Specification* 3069654 inventor; United States Atomic Energy Commission, assignee
[29] Duda R O and Hart P E 1972 Use of the Hough transformation to detect lines and curves in pictures *Commun. ACM* **15** 11–5

[30] Kimme C, Ballard D and Sklansky J 1975 Finding circles by an array of accumulators *Commun. ACM* **18** 120–2
[31] Hollitt C 2012 A convolution approach to the circle Hough transform for arbitrary radius *Mach. Vis. Appl.* **24** 683–94
[32] Canny J 1986 A computational approach to edge detection *IEEE Trans. Pattern Anal. Mach. Intell.* **8** 679–98
[33] Ramming P and Huang K 2017 Clustering and melting in a wet granular monolayer *EPJ Web Conf.* **140** 08003
[34] Goyal S, Papadopoulos J M and Sullivan P A 1998 The dynamics of clattering: I. Equation of motion and examples *J. Dyn. Syst.* **120** 83
[35] Botev Z I, Grotowski J F and Kroese D P 2010 Kernel density estimation via diffusion *Ann. Stat.* **38** 2916–57
[36] McDonald A J and McDonald K T 2000 The rolling motion of a disk on a horizontal plane arXiv:physics/0008227
[37] Kessler P and O'Reilly O M 2002 The ringing of Euler's disk *Reg. Chaot. Dyn.* **7** 49–60
[38] Ma D, Liu C, Zhao Z and Zhang H 2014 Rolling friction and energy dissipation in a spinning disc *Proc. R. Soc.* A **470** 20140191
[39] Morin D 2008 *Introduction to Classical Mechanics* (Cambridge: Cambridge University Press)
[40] Shmilovitz D 2005 On the definition of total harmonic distortion and its effect on measurement interpretation *IEEE Trans. Power Deliv.* **20** 526–8
[41] Harth K, Kornek U, Trittel T, Strachauer U, Höme S and Will K 2013 Granular gases of rod-shaped grains in microgravity *Phys. Rev. Lett.* **110** 144102
[42] Abramson I S 1982 On bandwidth variation in kernel estimates-a square root law *Ann. Stat.* **10** 1217–23
[43] Silverman B W 1986 *Density Estimation for Statistics and Data Analysis* 1st edn (London: Taylor and Francis)
[44] Duin R P W 1976 On the choice of smoothing parameters for parzen estimators of probability density functions *IEEE Trans. Comput.* **25** 1175–9
[45] Agarwal N and Aluru N R 2010 A data-driven stochastic collocation approach for uncertainty quantification in MEMS *Int. J. Numer. Methods Eng.* **83** 575–97

Publication 2

Set Voronoi Tessellation for Particulate Systems in Two Dimensions

Simeon Völkel and Kai Huang

In: Iker Zuriguel, Angel Garcimartín, Raúl Cruz Hidalgo (eds.)
Traffic and Granular Flow 2019
Springer Proceedings in Physics, vol **252**. Springer, Cham, Switzerland (2020)
(DOI: 10.1007/978-3-030-55973-1_53)

My contribution (80 %) consists in analytically deriving the limits of the over- and underestimation of the local packing fraction when using classical Voronoi tessellation in dense packings of rectangles, implementing the Set Voronoi algorithm in two dimensions, performing and analyzing the tessellations and the quantities derived therefrom, preparing all figures and writing the majority of the manuscript.

Kai Huang contributed (20 %) to the manuscript and supervised the research, for which I'm very grateful.

Set Voronoi Tessellation for Particulate Systems in Two Dimensions

Simeon Völkel and Kai Huang

Abstract Given a countable set of points in a continuous space, Voronoi tessellation is an intuitive way of partitioning the space according to the distance to the individual points. As a powerful approach to obtain structural information, it has a long history and widespread applications in diverse disciplines, from astronomy to urban planning. For particulate systems in real life, such as a pile of sand or a crowd of pedestrians, the realization of Voronoi tessellation needs to be modified to accommodate the fact that the particles cannot be simply treated as points. Here, we elucidate the use of Set Voronoi tessellation (i. e., considering for a non-spherical particle a *set of points* on its surface) to extract meaningful local information in a quasi-two-dimensional system of granular rods. In addition, we illustrate how it can be applied to arbitrarily shaped particles such as an assembly of honey bees or pedestrians for obtaining structural information. Details on the implementation of this algorithm with the strategy of balancing computational cost and accuracy are discussed. Furthermore, we provide our python code as open source in order to facilitate Set Voronoi calculations in two dimensions for arbitrarily shaped objects.

1 Introduction

Particulate systems are ubiquitous in nature, industry and our daily lives, ranging from active ones like pedestrians or animals, as in Fig. 1, to passive ones such as athermal granules. They all share the characteristics that the macroscopic behavior

Simeon Völkel
University of Bayreuth, Experimental Physics V, Universitätsstraße 30, 95447 Bayreuth, Germany, e-mail: simeon.voelkel@uni-bayreuth.de

Kai Huang
Duke Kunshan University, Division of Natural and Applied Sciences, No. 8 Duke Avenue, Kunshan, Jiangsu, China 215316, e-mail: kai.huang186@dukekunshan.edu.cn &
University of Bayreuth, Experimental Physics V, Universitätsstraße 30, 95447 Bayreuth, Germany

Fig. 1 Carniolan honey bees on a partially sealed honeycomb. The Set Voronoi tessellation (black) is based on multiple points (white) per bee.

depends on the arrangement of individual particles relative to each other. Prominent collective effects regarding the dynamics of granular materials, such as the solid-liquid-like transition [1, 2, 3, 4, 5, 6, 7, 8] and pattern formation [9, 10, 11], are typically triggered by the mobility of individual particles. Moreover, there also exists evidence showing that the strain field associated with local rearrangement of particles can be used to obtain the local stress field, which in turn can provide indispensable hints on the establishment of local force networks during jamming transition [12, 13, 14]. Investigations on granular systems thus often rely on accurate measurements of properties such as local volume fraction, neighborhood, etc. For defining these quantities, it is expedient to attribute to every particle a portion of the available space, that "belongs to" or "is occupied" by a single particle.

2 Limitations of the classical Voronoi tessellation

The honeycomb in Fig. 1 can be seen as an example of a naturally formed tessellation, optimized to have a fair distribution of space for individual larvae of bees to grow inside. Motivated by such self-organized processes in nature, the concept of spatial tessellation was established long time ago [15, 16, 17, 18] in order to analyze structures of various systems in diverse disciplines, from the structure of the universe in astronomy [15] through positioning public schools or post offices in urban planning [19] to characterizing topological aspects of molecular structures [20, 21, 22].

A generic, parameterless approach to attribute space based on a single point per object (typically its center) is the Voronoi tessellation (VT), also known as Dirichlet tessellation, Thiessen polygons or Wigner-Seitz cells [16, 17, 23, 24].

For mono-disperse spherical particles (as well as point-like particles), classical VT based on the particle centers is applicable and delivers intuitive results (see Fig. 2a). This, however, is not the case for polydisperse packings (see Fig. 2b)

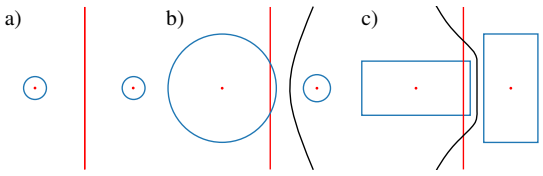

Fig. 2 Comparison of classical VT based on the center (red) of particles and Set VT (black) considering the border of the two particles (blue).

or non-spherical particles (see Fig. 2c). Here, part of the particle on the left lies outside of the Voronoi cell, contributing to an obvious source of error. To overcome this, various weighted Voronoi diagrams have been proposed (see, e. g., [18] for an overview) and implemented in physics and material science [25, 26].

Problems due to applying classical VT to a glass composed of *differently sized* (but spherical) atoms have already been discussed [26]. Here, we highlight the problems arising from applying classical VT to equally sized, but *elongated* particles.

3 Set Voronoi algorithm and implementations

A generic way to attribute space to both differently sized particles and non-spherical particles is to tessellate space according to the distance to the closest *surface* (as opposed to center). This can be seen as the limiting case of a classical VT, when considering for each particle the *set of points* marking its surface. Therefore it is also referred to as *Set Voronoi* diagram [27]. The resulting, intuitive cell-borders of the examples in Fig. 2 are depicted in black. Note that the Set Voronoi border for nonoverlapping monodisperse spheres (or circular discs in two dimensions) like in Fig. 2a coincides with the classical Voronoi cell border. Voronoi diagrams with lines and arcs as generators have been studied systematically since the late 1970s [18]. Nevertheless, their importance in the realm of granular physics was rarely realized until the past decade [28, 27, 29, 30].

Recently, Weis & Schönhöfer [31] provided a program based on the Voro++ library [32] to calculate the Set VT, targeting reconstructed CT-scans of three-dimensional (3D) packings of non-spherical granular particles [30]. However, an urgent demand for a solution in two dimensions remained, as it is computationally not economic to apply the 3D algorithm directly to two-dimensional (2D) systems [33]: Adding dimensions to the problem inevitably increases the computational cost for obtaining the tessellation, letting aside the efforts now required to treat the borders in the added dimension(s). Considering as well the fact that many particulate problems of practical interest (e. g., dynamics of pedestrians, flocks or monolayers of granulates) can be treated (quasi-) two-dimensionally and very often data is acquired using 2D imaging techniques, we implemented the Set VT strategy based on discrete points put forward by Schaller et al. [27] in 2D. Our implementation uses the python scripting language together with scipy/numpy libraries [34], relying on VT routines provided by the Qhull library [35]. It is available as free open source software [36].

4 Granular rod monolayer as a test case

As an example, we demonstrate the advantages of Set VT using a monolayer of monodisperse granular rods of length $l = 15\,\mathrm{mm}$ and diameter $d = 3\,\mathrm{mm}$. They are confined in a horizontal cylindrical container of diameter $D = 19\,\mathrm{cm}$, which is

subjected to sinusoidal vibrations against gravity with oscillation frequency f and dimensionless acceleration Γ as two control parameters to keep the rods mobilized. More details on the experimental set-up and image analysis procedure can be found in [37]. Depending on the packing density, the rods may organize themselves into an uniaxial nematic state with two-fold rotational symmetry or tetratic state with 4-fold symmetry. For analyzing the disorder-order transition quantitatively, an accurate determination of the local packing density is desired. For amorphous media, such as a random packing of granular particles, (Set) VT provides a direct route to the local area or volume fractions of individual grains [38, 39, 27].

Fig. 3 compares the outcome of classical and Set VT based on a snapshot reconstructed from the positions and orientations obtained experimentally in [37]. This particular snapshot is chosen, as it consists of both dense and dilute regions. The classical VT does not include walls and leads to cells cutting the walls of a container (red solid lines crossing the gray area in Fig. 3a) or even extending to infinity (red dashed lines in Fig. 3a). These problems can be easily and consistently avoided using Set VT, as the container can be included as an additional 'particle', naturally limiting the cells of all contained particles (see Fig. 3b). Additionally Set VT delivers a much more reasonable tiling in the sense that no particle cuts its cell's border, as the container lid prohibits the 'hard' rods from overlapping. Quantitatively, the local packing density $\phi = A_\mathrm{p}/A_\mathrm{c}$ derived from the projected area of the particles $A_\mathrm{p} = l \cdot d$ and the area of the corresponding cell A_c obtained from the space tiling also demonstrates the difference clearly: Cells with 'impossible' $\phi > 1$ (see color code) disappear and large fluctuations of ϕ for rods aligned with each other in a similar local configuration diminish as Set VT is implemented.

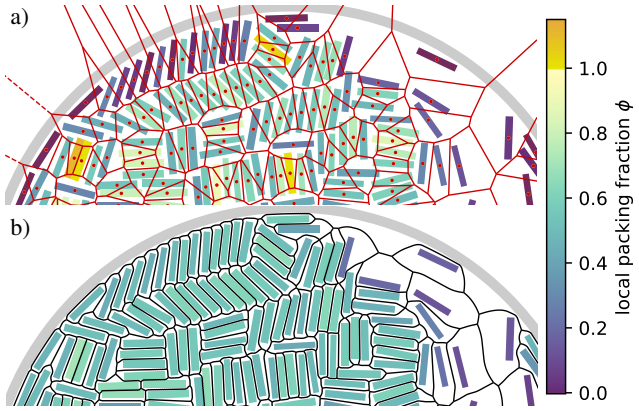

Fig. 3 VT (a) and Set VT (b) of partly ordered granular rods in quasi-two-dimensions. The parameters are: particle number $N = 400$, driving frequency $f = 50\,\mathrm{Hz}$ and dimensionless acceleration $\Gamma = 6.26$. The color code indicates the local packing fraction ϕ according to the different tessellations: classical VT considering the particle centers (red, upper panel) vs. Set VT (black, lower panel) including the container rim as additional particle.

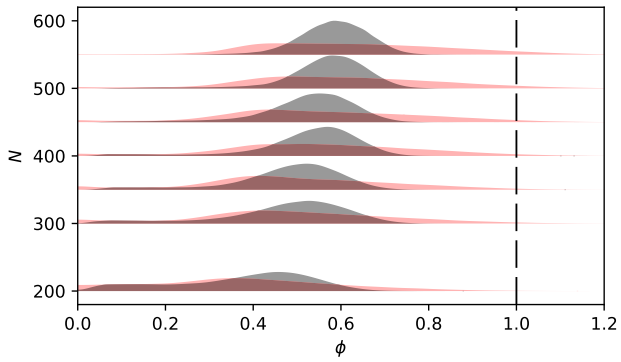

Fig. 4 Probability density P_ϕ of the local packing fraction ϕ for different numbers of particles N in the container, obtained from kernel density estimation. Light red and dark gray curves correspond to classical and Set VT, respectively. The peak acceleration is kept in the range $\Gamma \in [1.94; 20.59]$ and $f = 50\,\mathrm{Hz}$ is fixed. Other experimental parameters are the same as in Fig. 3. The reflection method [41, 42] has been used to correct for ϕ being non-negative by definition, and the bandwidth of the Gaussian kernel is chosen according to Scotts rule [43] as $\sigma \cdot n^{-1/5}$ proportional to the standard deviation σ of the distribution and dependent on the number of rods n (here 1.7×10^5 to 5.3×10^5 per stacked plot). Captured frames with detection problems (particles (partially) outside of the container, overlapping or of zero size) were skipped to avoid bias.

Fig. 4 compares the local packing density distribution obtained from VT (red) and Set VT (black) for different global packing densities. For Set VT, the probability density P_ϕ shows a clear trend of an increasing local packing density with the global one. This feature is much less obvious for the classical VT. There, the most striking observation is the tail of the distribution towards large ϕ becoming more prominent. The dashed line at $\phi = 1$ marks the upper bound for hard particles and a reasonable tiling. All red curves clearly exceed this limit. This manifests again the importance of observing the applicability of each tessellation technique.

5 Why Set Voronoi is essential for elongated particles

To analyze quantitatively the maximal error introduced by applying the classical VT to elongated particles, we consider a perfect, dense packing of identical “hard” rectangles. With no space left between the non-overlapping rectangles, a constant local packing fraction equal to the global packing fraction of unity is expected.

Fig. 5 gives an example for such a dense packing of rectangles with width-to-length ratio ε. Classical VT (red lines) gives the expected value for the local packing fraction, as indicated by the color code, if all neighboring particles are aligned in the same direction (cf. particles a and a’ in Fig. 5) but fluctuates significantly where rectangles of different orientation come together. Here, local packing fractions up to $\phi_{\mathrm{VT,max}} = 2/(1+\varepsilon)$ are obtained, e. g., for particle b in Fig. 5. This overestimation is thus a

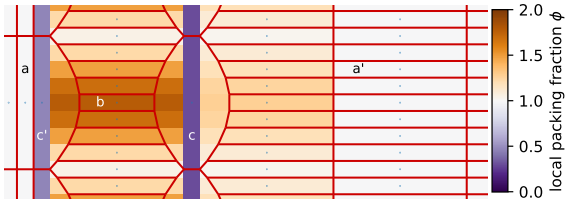

Fig. 5 Local packing fraction (see color code) according to classical VT (red lines, based on particle centers) in a dense packing of rectangles with $\varepsilon = 1/8$ exhibiting tetratic ordering.

first order effect in terms of ε. It can reach a remarkable error of 100 % for vanishing width-to-length ratio, even when letting aside any experimental inaccuracies or elasticity of the particles. At the same time, the local packing fraction for neighboring particles c and c' in Fig. 5 is underestimated, up to an equally dramatic extent as $\varepsilon \to 0$. Even for a *dense* packing of hard particles (global packing fraction of unity) and without boundary effects, classical VT can indicate *vanishing* local packing fraction, deviating disastrously from the expected value!

On the contrary, Set VT gives consistent local packing fractions. It delivers a value of $\phi_{\mathrm{Set\,VT}} = 1$ for every rectangle in Fig. 5 within the numerical uncertainty arising from the approximation of the surface through a finite number of points.

6 Performance vs. quality trade-off via erosion

For closely spaced particles special care is required to identify their surface properly before applying the Set VT. For rounded particles with a finite minimal curvature radius r_c, Schaller et al. [27] show that it is highly beneficial to consider the maximally eroded surfaces, having the constant minimal distance r_c to the original ones: Using the eroded surface, dramatically fewer points suffice for obtaining the same Set VT and accuracy. In addition, erosion can resolve slight particle overlap. This is particularly helpful for densely packed particles close to jamming [44] and is expected to make investigations of deformable particles feasible [27].

For the granular rods discussed above, the rectangles seen by the camera have sharp corners. In other words, $r_c = 0$, preventing a 'lossless' erosion. Accurately capturing the sharp corners commands a vanishing erosion depth, which in turn dictates a very close spacing of the discretization points on the eroded surface. As describing a surface with a larger number of points inevitably increases the computational costs, a compromise between accuracy and speed has to be found. Here, we erode the rods by one pixel to remove slight overlap due to finite experimental resolution, detection accuracy and finite elasticity of the particles. Setting the maximum distance between discretization points to the erosion depth delivers satisfactory results and we recommend this as a rule of thumb.

For many systems, however, the situation is more pleasant, especially if the most important property is the elongation, while the dimensions along the other direction(s) are equal and the exact shape of each particle only plays a tangential role, like in the case of the bees shown in Fig. 1. In such a case, it is typically acceptable

to approximate the particle as spherocylinder. This approximation paves the way to a very efficient representation of the particle when using Set VT: The maximally eroded 'surface' of each particle is then just its medial axis, a one-dimensional line segment. Furthermore, according to the rule of thumb, one discretization point per radius of the spherocylinder r suffices for satisfactory results even at high packing densities. For the bees on the honeycomb, this translates to a single digit number of discretization points, each depicted as a white dot in Fig. 1. Nevertheless, this is sufficient for resolving the most prominent and important effects due to the elongated shape of the individual bee, as the black Set Voronoi cell borders illustrate.

As similarly sized rod-shaped particles represent a diverse class of systems, from liquid crystal molecules at a microscopic scale to pedestrians viewed from the top (i. e., when taking their shoulders into account), the above analysis demonstrates that it is essential to employ Set VT for elongated particles.

7 Conclusion

Using dynamics of a granular rod monolayer as an example, we demonstrate that Set VT provides a more meaningful tiling of space in comparison to the classical VT that relies on the center of particles. From polydisperse systems to irregularly shaped or even deformable particles, the Set VT algorithm is expected to be substantially more consistent in characterizing the geometric and topological features of particulate systems, many of which can be approximated as elongated particles.

Note that in addition to obtaining the local packing density, VT can also be used to extract other order parameters, such as determining neighbors of individual particles. The Delaunay triangulation, which connects particle centers to their neighbors, follows the natural definition that neighbors share a part of a Voronoi cell border and is a typical approach after classical VT. The extension of this definition to Set VT is straightforward and can be used in further characterizations, for instance, using the bond orientational order parameter [5]. How to extract more meaningful information from Set VT in addition to the local packing density and the improvements against the classical VT will be a focus of future investigations.

Acknowledgements We gratefully acknowledge helpful discussions with Simon Weis, Matthias Schröter, Ingo Rehberg, Stefan Hartung and Wolfgang Schöpf. We thank Alexander and Valentin Dichtl for the possibility of taking the picture of the bees in Fig. 1 during an inspection of the hive. This work is supported by the German Research Foundation (DFG) under Grant No. HU1939/4-1.

References

1. K. Huang, C. Krülle, I. Rehberg, J. Appl. Math. Mech. **90**(12), 911 (2010). DOI 10.1002/zamm.201000110
2. K. Huang *et al.*, Phys. Rev. E **79**(1), 010301 (2009). DOI 10.1103/PhysRevE.79.010301

3. K. Huang, K. Röller, S. Herminghaus, Eur. Phys. J. Special Topics **179**(1), 25 (2009). DOI 10.1140/epjst/e2010-01191-5
4. B. Andreotti, Y. Forterre, O. Pouliquen, *Granular Media: Between Fluid and Solid* (Cambridge University Press, 2013)
5. C. May *et al.*, Phys. Rev. E **88**(6), 062201 (2013). DOI 10.1103/PhysRevE.88.062201
6. S.C. Zhao, M. Schröter, Soft Matter **10**(23), 4208 (2014). DOI 10.1039/C3SM53176G
7. P. Ramming, K. Huang, EPJ Web Conf. **140**, 08003 (2017). DOI 10.1051/epjconf/201714008003
8. M. Baur, K. Huang, Phys. Rev. E **95**(3), 030901 (2017). DOI 10.1103/PhysRevE.95.030901
9. G.H. Ristow, *Pattern Formation in Granular Materials* (Springer, 2000)
10. A. Fortini, K. Huang, Phys. Rev. E **91**(3), 032206 (2015). DOI 10.1103/PhysRevE.91.032206
11. A. Zippelius, K. Huang, Sci. Rep. **7**(1) (2017). DOI 10.1038/s41598-017-03844-0
12. A.J. Liu, S.R. Nagel, Nature **396**(6706), 21 (1998). DOI 10.1038/23819
13. D. Bi *et al.*, Nature **480**(7377), 355 (2011). DOI 10.1038/nature10667
14. Y. Zhao *et al.*, Phys. Rev. Lett. **123**, 158001 (2019). DOI 10.1103/PhysRevLett.123.158001
15. R. Descartes, *Principles of Philosophy* (Amsterdam, 1644). 3-7873-1697-3
16. G. Dirichlet, Journal fur die reine und angewandte Mathematik (40), 209 (1850)
17. G. Voronoi, Journal fur die reine und angewandte Mathematik (133), 97 (1907)
18. A. Okabe *et al.*, *Spatial Tessellations: Concepts and Applications of Voronoi Diagrams*, 2nd edn. (John Wiley & Sons, Ltd, 2000). DOI 10.1002/9780470317013
19. M. McAllister, D. Kirkpatrick, J. Snoeyink, Discrete Comput. Geom. **15**(1), 73 (1996)
20. A.L. Mackay, J. Molec. Struct. **336**(2), 293 (1995). DOI 10.1016/0166-1280(95)04172-3
21. F. Aurenhammer, ACM Comput. Surv. **23**(3), 345 (1991). DOI 10.1145/116873.116880
22. J. Bernauer *et al.*, Bioinformatics **24**(5), 652 (2008). DOI 10.1093/bioinformatics/btn022
23. A.H. Thiessen, Mon. Weather Rev. **39**(7), 1082 (1911). DOI 10.1175/1520-0493(1911)39<1082b:PAFLA>2.0.CO;2
24. E. Wigner, F. Seitz, Phys. Rev. **43**, 804 (1933). DOI 10.1103/PhysRev.43.804
25. J. Park, Y. Shibutani, Intermetallics **15**(2), 187 (2007). DOI 10.1016/j.intermet.2006.05.005
26. J. Park, Y. Shibutani, Intermetallics **23**, 91 (2012). DOI 10.1016/j.intermet.2011.12.019
27. F.M. Schaller *et al.*, Philos. Mag. **93**(31-33), 3993 (2013). DOI 10.1080/14786435.2013.834389
28. A. Baule *et al.*, Nat. Commun. **4**(1), 2194 (2013). DOI 10.1038/ncomms3194
29. A. Baule, H. A. Makse, Soft Matter **10**(25), 4423 (2014). DOI 10.1039/C3SM52783B
30. S. Weis *et al.*, EPJ Web Conf. **140**, 06007 (2017). DOI 10.1051/epjconf/201714006007
31. S. Weis, P. Schönhöfer. Pomelo: calculate generic set voronoi diagrams with c++11 (2017). URL http://theorie1.physik.fau.de/research/pomelo/index.html
32. C. Rycroft, Voro++: a three-dimensional Voronoi cell library in C++. Tech. Rep. LBNL-1432E, 946741 (2009). DOI 10.2172/946741
33. S. Weis. private communication
34. P. Virtanen *et al.*, Nat. Methods **17**(3), 261 (2020). DOI 10.1038/s41592-019-0686-2
35. C.B. Barber *et al.*, ACM Trans. Math. Softw. **22**(4), 469 (1996). DOI 10.1145/235815.235821
36. S. Völkel. setvoronoi2d: Calculate the Set Voronoi tessellation in two dimensions. online. DOI 10.5281/zenodo.3531546
37. T. Müller *et al.*, Phys. Rev. E **91**(6), 062207 (2015). DOI 10.1103/PhysRevE.91.062207
38. C. Song, P. Wang, H.A. Makse, Nature **453**(7195), 629 (2008). DOI 10.1038/nature06981
39. S. Torquato, F.H. Stillinger, Rev. Mod. Phys. **82**(3), 2633 (2010). DOI 10.1103/RevModPhys.82.2633
40. O. Tange, *GNU Parallel 2018* (Ole Tange, 2018). DOI 10.5281/zenodo.1146014
41. B. Silverman, *Density Estimation for Statistics and Data Analysis*. Monographs on Statistics & Applied Probability (Chapman & Hall, 1986)
42. L.I. Boneva, D. Kendall, I. Stefanov, J. Royal Stat. Soc. B **33**(1), 1 (1971). DOI 10.1111/j.2517-6161.1971.tb00855.x
43. D.W. Scott, *Multivariate density estimation: theory, practice, and visualization*, 2nd edn. (Wiley, Hoboken NJ, 2015). DOI 10.1002/9781118575574
44. I. Zuriguel *et al.*, Sci. Rep. **4**, 7324 (2014). DOI 10.1038/srep07324

Publication 3

Dynamics of wetting explored with inkjet printing

Simeon Völkel and Kai Huang

EPJ Web of Conferences **140**, 09035 (2017)
(DOI: 10.1051/epjconf/201714009035)

My contribution (80 %) consists in designing and implementing the experimental setup including the microcontroller firmware and software used for control, automation and image analysis, conducting and analyzing all experiments, preparing all figures and writing parts of the manuscript.

Kai Huang contributed (20 %) substantially to the manuscript and supervised the research, for which I'm very grateful.

EPJ Web of Conferences **140**, 09035 (2017) DOI: 10.1051/epjconf/201714009035
Powders & Grains 2017

Dynamics of wetting explored with inkjet printing

Simeon Völkel[1,⋆] and *Kai* Huang[1,⋆⋆]

[1] *Experimentalphysik V, University of Bayreuth, 95440 Bayreuth, Germany*

Abstract. An inkjet printer head, which is capable of depositing liquid droplets with a resolution of 22 picoliters and high repeatability, is employed to investigate the wetting dynamics of drops printed on a horizontal plane as well as on a granular monolayer. For a sessile drop on a horizontal plane, we characterize the contact angle hysteresis, drop volume and contact line dynamics from side view images. We show that the evaporation rate scales with the dimension of the contact line instead of the surface area of the drop. We demonstrate that the system evolves into a closed cycle upon repeating the depositing-evaporating process, owing to the high repeatability of the printing facility. Finally, we extend the investigation to a granular monolayer in order to explore the interplay between liquid deposition and granular particles.

1 Introduction

Granular materials are ubiquitous in nature, industry and daily lives [1]. Despite intense investigations motivated by applications in geoscience, chemical and civil engineering, the physics of granular materials, are still far from being understood, particularly when they are partially wet [2–4]. The mechanical properties of a granular material change dramatically as a tiny amount wetting liquid is added, representing the formation of capillary bridges between adjacent particles [5, 6]. The enhancement of rigidity leads to an easily moldable material such as wet sand on the beach for sculpturing [7, 8]. In the pendular regime [3] with capillary bridges formed between adjacent particles, previous investigations showed that the collective behaviors of partially wet granular materials, such as clustering, phase transitions and pattern formation, are related to the capillary force induced by the wetting liquid [9–13]. However, as more liquid is added, it is still challenging to understand how a wetting liquid film advances inside a geometrically heterogeneous granular packing, as well as how the particles respond to the capillary interactions induced by the additional wetting liquid.

Wetting is also an ubiquitous phenomenon that has attracted interest from physics, chemistry and engineering communities over the past decades [14, 15]. More recently, there has been a growing interest in understanding the wetting dynamics on patterned and heterogeneous surfaces, motivated by a better control of wettability and liquid transport [16, 17]. Nevertheless, there are still open questions (e. g. contact angle hysteresis, contact line dynamics at the onset of the pinning-depinning transition, etc.) [18–20].

Here, we use a commercial inkjet printer head (HP 51645A) to explore the dynamics of wetting, because it enables a fine control of the drop volume with high repeatability. For both a horizontal plane and a granular monolayer, repeating the print-evaporate process leads to reproducible contact line dynamics.

2 Setup

Figure 1 shows a sketch of the experimental setup. An empty print catridge (HP C6125A) is filled with purified water (LaborStar TWF, surface tension $\gamma = 0.072\,\mathrm{N\,m^{-1}}$). Its printhead is pointing downwards in order to deposit droplets vertically onto the horizontal substrate [polytetrafluoroethylene (PTFE), and a monolayer of glass beads (SiLiBeads Type S)]. In order to control all nozzles (printing frequency 2.8 kHz) individually, we use a custom microcontroller board (Microchip PIC18F6722). Two types

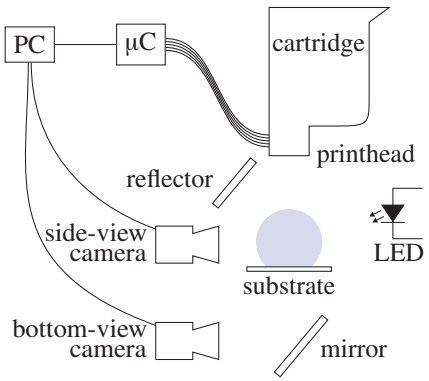

Figure 1: Schematic diagram of the experimental setup. μC stands for microcontroller. A reflector is used to provide back-light illumination for the bottom view camera.

⋆ e-mail: simeon.voelkel@uni-bayreuth.de
⋆⋆ e-mail: kai.huang@uni-bayreuth.de

of cameras (Lumenera LU135M, Nikon D7000) are used to take side view and bottom view images.

A computer program (PC) triggers the image acquisition for one experimental cycle N_{print} times during the printing phase, each time after a specific volume V_{step} has been deposited, and N_{evap} times during evaporation phase, at a fixed interval T_{evap}. The ambient temperature is regulated to 20 °C. The relative humidity is in the range from 20 % to 40 %. The average droplet volume is determined to be 22.4(11) pL by image analysis of side view images.

3 Image analysis

Figure 2 summarizes the image analysis procedure to obtain the geometric properties of the sessile drop. The side view images are cropped such that the bottom of the rectangular region of interest (ROI) separates the drop from the substrate, and binarized to segment the image.

Figure 2a defines the quantities of the drop. The volume V is estimated assuming rotational symmetry along the vertical axis of the drop in each line of the image, as shown in Fig. 2b. The left and right contact angles ϕ_l and ϕ_r as well as the (horizontal) x-coordinates of the associated contact points $x_{c,l}$, $x_{c,r}$ are determined with subpixel resolution by fitting locally a parabola using the standard least square method to the drop contour. Short[1], adjacent segments of the contour are used, as indicated by Fig. 2c. As shown in Fig. 2d, the fit is not performed in the laboratory frame (x, y), but in the rotated (x', y') coordinate system set by the first (1) and last point (n) of the contour segment. This is to circumvent ambiguity problems with contact angles close to 90° as sketched in Fig. 2c and increase both robustness and accuracy. The diameter of the contact line d_c is estimated as the distance between the two contact points (cf. Fig. 2a).

[1]For estimating the (vertical) radius of curvature of a sessile drop close to the contact points, its contour in the side view can be approximated as a part of an ellipse. The short main axis gives a good estimate independent of the drop volume and contact angle. Here, a contour segment one order of magnitude shorter is used. Fig. 2c is not to scale.

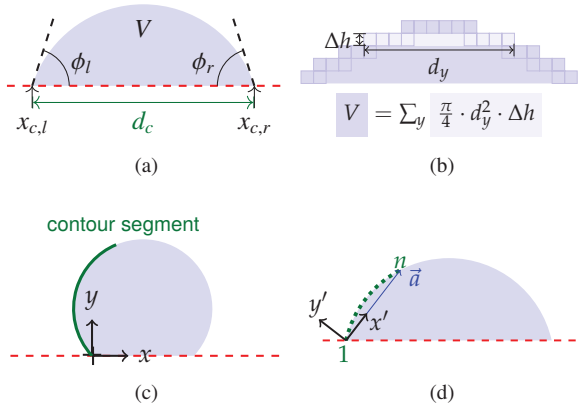

Figure 2: Image analysis procedure and definitions of drop quantities. The red dashed lines indicate the substrate.

4 Results and discussion

Figure 3 shows the development of d_c as a function of $V^{\frac{1}{3}}$ for six print-evaporate cycles. Starting with an initial drop (1), its volume is increased by adding water droplets from above using the inkjet printhead. At first, d_c remains constant until the advancing contact angle is reached (2). As further liquid is added, the drop expands laterally (3), (4). During evaporation, the drop again first keeps d_c constant until the receding contact angle is reached (5). Further evaporation lets the drop shrink laterally (6). When adding some liquid again, the same behaviour recurs. The overlapping curves for cycles 4–6 illustrate the excellent repeatability of the experimental setup and that the deposition-evaporation process can be driven into a closed cycle by just periodically adding a fixed volume with high precision.

In the limit of small drops (i. e. small Bond-number $\text{Bo} = \rho g V^{\frac{2}{3}} \gamma^{-1}$, where ρ: fluid density, g: gravitational acceleration), interfacial tension determines the equilibrium shape of a drop and all linear dimensions of the drop scale with $V^{\frac{1}{3}}$. With growing volume, the relative influence of gravity increases and finally flattens the drop [21]. The drops (2), (3) and (4) as well as (1), (5) and (6) have consistent shapes. It is worth noting that both lateral expansion and shrinking of the drop follow a sloped straight line in Fig. 3: The sessile drops (Bo < 1.65) are thus small. However, due to contact angle hysteresis, the shapes of an expanding and contracting drop differ, which results in two distinct slopes in Fig. 3.

Figure 4 shows the contact angle at the right edge ϕ_r plotted over d_c during the last three print-evaporate cycles. While the contact line is advancing or receding, the contact angle remains approximately constant. As the contact angle for the two directions of movement differs, contact angle hysteresis is clearly visible. In the inset images (1)–(6) of Fig. 3, the drop expands to his right side, keeping

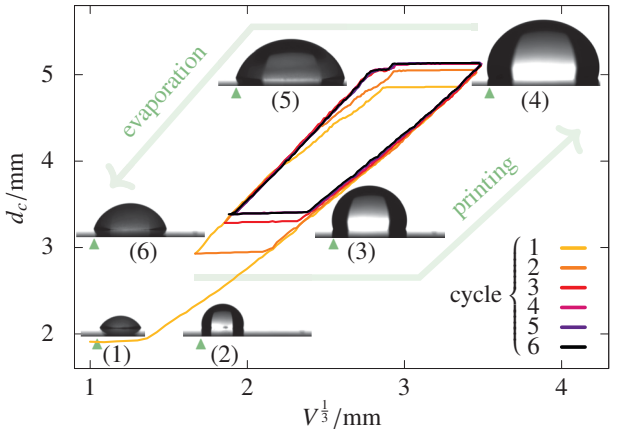

Figure 3: Scaling of the contact line diameter d_c with the drop volume V for water on PTFE. Six cycles of $N_{\text{print}} = 120$, $V_{\text{step}} = 0.34(2)\,\mu\text{L}$, $N_{\text{evap}} = 120$, $T_{\text{evap}} = 60\,\text{s}$ are shown. The triangles mark the same position on the substrate. See text for details.

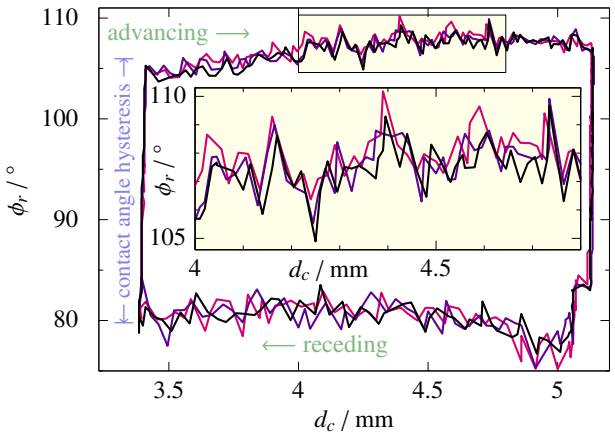

Figure 4: Contact angle ϕ_r of water on PTFE measured from side view images at the freely moving edge. Coloring corresponds to Fig. 3.

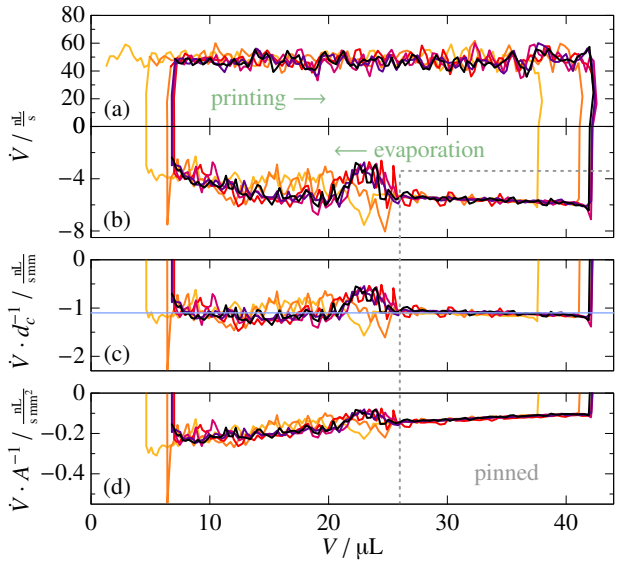

Figure 5: (a) and (b): Effective printing and evaporation rate estimated from side view images. (c) and (d): Comparison of two scaling laws for the evaporation rate. The blue line corresponds to $-1.1\,\mathrm{nL\,s^{-1}\,mm^{-1}}$ and is a guide to the eye. See text for details. Coloring corresponds to Fig. 3.

his left edge at a fixed position. This is due to inhomogenities on the substrate, resulting in a slightly larger contact angle hysteresis there than for the rest of the contact line. Thanks to the pinned left side in the experiments shown in Fig. 4, equal d_c results in coincident positions $x_{c,r}$ of the right edge of the drop. The inset in Fig. 4 magnifies and highlights a part of the graph. The strong correlation between subsequent runs reveals that the fluctuations in the measured contact angles come from the drop's exploration of the surface heterogenities. Figure 5 shows that the average deposition rate of the used printing-protocol exceeds the evaporation rate by an order of magnitude. While evaporation drives the recedence of the contact line, its influence on the advance is marginal. As a result, the advancing contact angle in Fig. 4 exhibits a more prominent correlation than the measurements during the receding phase.

As the blue horizontal line in Fig. 5c illustrates, the evaporation rate scales with the contact line diameter. Thus we conclude that the drop evaporates mainly through its three phase line (see [22]) instead of its surface area (see Fig. 5d for a comparison). The scaling of the evaporation with the drop geometry reveals that our sessile drop is also small in this regard.

Having illustrated the repeatability provided by the setup when using a flat substrate, we now extend our investigation to a granular monolayer. Concerning wetting in a granular system, one of the most important challenges is to understand the interplay between wetting liquid and granules. The particles are subject to capillary forces if they are not immersed in liquid. In a loose packing, a movement of the liquid interface can therefore lead to a movement of granules, if they are not fully constrained by their neighbours. The details of the advancing and receding of the liquid interface, the involved wetting and dewetting, as well as rupture events of capillary bridges are strongly dependend on the the configuration of neighboring particles [23].

For the following experiments, spherical glass beads of 0.3 mm to 0.4 mm diameter are put on top of a horizontal glass slide. By tapping they are brought into a two-dimensional random packing. Further beads are added until the bottom of a 25×25.5 mm rectangular enclosure is filled. After initial reorganization of some particles, the system again can apparently be driven into a closed cycle by periodically adding and evaporating water.

Figure 6 compares two subsequent printing-cycles on this three-dimensionally patterned substrate. After removing the background by division, the overlaid images are obtained by putting into their red and blue channels the image of one cycle and in their green channels the image of the subsequent one. Qualitatively, Fig. 6 provides the following features: (i) The contour of a sessile drop on a granular layer does not exhibit a circular contact line due to the prominent structure of the substrate. (ii) The deviation from a circle is more than the particle size, especially if the wettability of the substrate is high. This is partially due to the fact that the wetting of a neighbouring particle is a discrete event which leads to an abrupt change of the liquid interface position. (iii) While for drops on an inclined homogeneous plane the aspect ratio of the bottom view is a suitable parameter for describing, e. g., the onset of sliding [20], the irregularly jagged contact line shown here raises the question: Which shape descriptors are suitable for the case of a partially wetted granular layer? Finally, the tiny difference in the shape of the wetted area (see colored regions in Fig. 6) clearly illustrates that, even in this complex system, this setup offers a high repeability.

5 Summary

In this work, we use a commercial inkjet printer head, which provides a fine volume control of liquid deposition

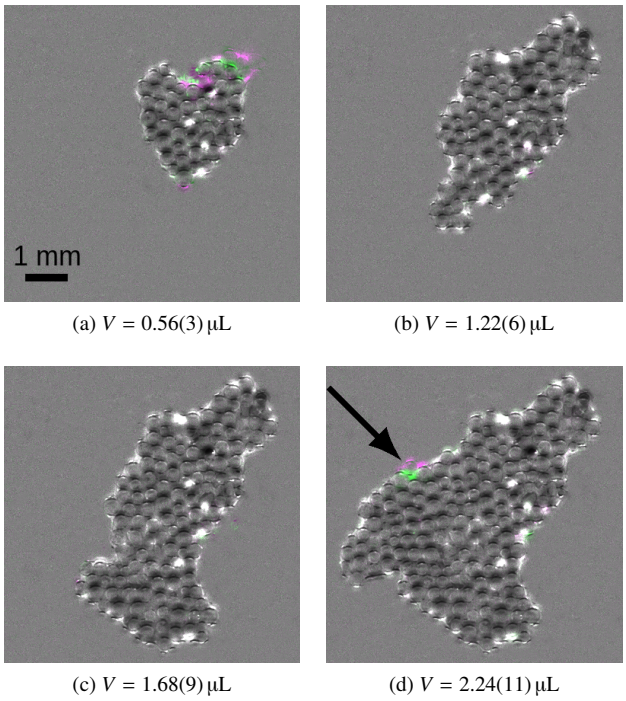

(a) $V = 0.56(3)\,\mu L$ (b) $V = 1.22(6)\,\mu L$

(c) $V = 1.68(9)\,\mu L$ (d) $V = 2.24(11)\,\mu L$

Figure 6: Overlay of typical bottom view images taken in two subsequent printing cycles ($N_{print} = 100$, $V_{step} = 22.4(11)\,nL$, $N_{evap} = 40$, $T_{evap} = 30\,s$). Unsaturated pixels show regions of identical wetting while green and purple regions highlight the differences of the wetted area. See, for example, the region marked by the arrow in (d).

in a well controlled and cost-effective way, to explore the wetting dynamics of liquid drops on a plane and a granular monolayer.

For a sessile drop on a plane, we demonstrate the excellent repeatability of the setup through applying print-evaporate cycles and monitoring the drop geometry. Contact angle hyteresis is observed. The evaporation rate is found to scale with the diameter of the drop contact line, which is in agreement with a previous investigation [22]. Thanks to the high and adjustable printing rate ($63(3)\,nL\,s^{-1}$ per nozzle), water evaporation can be easily compensated by printing in typical experimental conditions.

Remarkably, we find that, even on a discrete substrate like a granular layer, this print-evaporate protocol leads to reproducible contour line dynamics. This feature facilitates further investigations on the interactions between a wetting liquid and a granular bed, in order to shed light on the advance of additive manufacturing as well as other drop-on-demand applications [24, 25].

References

[1] J. Duran, *Sands, Powders and Grains (An Introduction to the Physics of Granular Materials)*, 1st edn. (Springer-Verlag, New York, Inc., 2000)
[2] S. Herminghaus, Adv. Phys. **54**, 221 (2005)
[3] N. Mitarai, F. Nori, Adv. Phys. **55**, 1–45 (2006)
[4] K. Huang, Habilitation thesis, University of Bayreuth (2014)
[5] T. Halsey, A. Levine, Phys. Rev. Lett. **80**, 3141 (1998)
[6] K. Huang, M. Sohaili, M. Schröter, S. Herminghaus, Phys. Rev. E **79**, 010301 (2009)
[7] M. Scheel, R. Seemann, M. Brinkmann, M. Di Michiel, A. Sheppard, B. Breidenbach, S. Herminghaus, Nat. Mater. **7**, 189 (2008)
[8] M. Pakpour, M. Habibi, P. Møller, D. Bonn, Sci. Rep. **2** (2012)
[9] K. Huang, K. Roeller, S. Herminghaus, Eur. Phys. J. Spec. Top. **179**, 25 (2009)
[10] K. Huang, I. Rehberg, Phys. Rev. Lett. **107**, 028001 (2011)
[11] K. Huang, M. Brinkmann, S. Herminghaus, Soft Matter **8**, 11939 (2012)
[12] C. May, M. Wild, I. Rehberg, K. Huang, Phys. Rev. E **88**, 062201 (2013)
[13] L. Butzhammer, S. Völkel, I. Rehberg, K. Huang, Phys. Rev. E **92**, 012202 (2015)
[14] P.G. de Gennes, Rev. Mod. Phys. **57**, 827 (1985)
[15] D. Bonn, J. Eggers, J. Indekeu, J. Meunier, E. Rolley, Rev. Mod. Phys. **81**, 739 (2009)
[16] C. Semprebon, P. Forsberg, C. Priest, M. Brinkmann, Soft Matter **10**, 5739 (2014)
[17] M. Sbragaglia, L. Biferale, G. Amati, S. Varagnolo, D. Ferraro, G. Mistura, M. Pierno, Phys. Rev. E **89**, 012406 (2014)
[18] U. Thiele, E. Knobloch, Phys. Rev. Lett. **97** (2006)
[19] H.B. Eral, D.J.C.M. 't Mannetje, J.M. Oh, Colloid Polym. Sci. **291**, 247 (2013)
[20] C. Semprebon, M. Brinkmann, Soft Matter **10**, 3325 (2014)
[21] C.W. Extrand, S.I. Moon, Langmuir **26**, 11815 (2010)
[22] H. Hu, R.G. Larson, J. Phys. Chem. B **106**, 1334 (2002)
[23] C. Semprebon, M. Scheel, S. Herminghaus, R. Seemann, M. Brinkmann, Phys. Rev. E **94**, 012907 (2016)
[24] A. Yarin, Ann. Rev. Fluid Mech. **38**, 159 (2006)
[25] B. Derby, Ann. Rev. Mat. Res. **40**, 395 (2010)

Publication 4

Assembly of eight spherical magnets into a dotriacontapole configuration

Stefan Hartung, Felix Sommer, Simeon Völkel,
Johannes Schönke, Ingo Rehberg

Physical Review B **98**, 214424 (2018)
(DOI: 10.1103/PhysRevB.98.214424)

Stefan Hartung contributed (50 %) the program for controlling the magnetic-flux density scanner setup, designed and conducted the vast majority of experiments, supervised the characterization of the magnets, analyzed the data, prepared all figures and tables and wrote the manuscript.

Felix Sommer characterized the magnets **(5 %)**.

My contribution (20 %) consists in developing a prototype of the setup and fitting program for quantifying the magnetic moment as well as deviations from a point dipole approximation based on two dimensional scans and discussing the results.

Johannes Schönke contributed (20 %) the analytical theory.

Ingo Rehberg contributed (5 %) the assembly time estimation and supervised the research as well as the writing of the manuscript.

Assembly of eight spherical magnets into a dotriacontapole configuration

Stefan Hartung,[1,*] Felix Sommer,[1] Simeon Völkel,[1] Johannes Schönke,[2,†] and Ingo Rehberg[1,‡]
[1]*Experimentalphysik V, Universität Bayreuth, D-95440 Bayreuth, Germany*
[2]*Okinawa Institute of Science and Technology Graduate University, Onna, Okinawa 904-0495, Japan*

(Received 30 August 2018; revised manuscript received 31 October 2018; published 13 December 2018)

The magnetic field of a cuboidal cluster of eight magnetic spheres is measured. It decays with the inverse seventh power of the distance. This corresponds formally to a multipole named a dotriacontapole. This strong decay is explained on the basis of dipole-dipole interaction and the symmetry of the ensuing ground state of the cuboidal cluster. A method to build such dotriacontapoles is provided.

DOI: 10.1103/PhysRevB.98.214424

I. INTRODUCTION

Within the forces determining the interplay of condensed matter, the dipole-dipole interaction can be considered as the most important one, because monopoles do not exist for neutral matter, and pure quadrupole, octopole, or hexadecapol interaction tends to be masked by induced dipole moments. While the interaction of quadrupoles is not too exotic [1] and includes examples from continuum mechanics [2], pure octopole or even higher order interaction is different. Here we demonstrate that the combination of eight dipoles in a simple cubic arrangement leads to a 32-pole or dotriacontapole.

The exploration of the cuboidal dipole arrangement discussed here is triggered by the investigation of magnetic nanoparticles, which have been reported to self-assemble into such configurations [3,4]. The most elementary cluster of this type contains only eight particles. It can also be assembled macroscopically as a cubic cluster from eight magnetic spheres, as indicated by the left-hand side inset of Fig. 1, and described previously [5,6]. The ground state of this arrangement is stable, and an interesting continuum [5,7]. In this state, the spheres attract each other by the magnetic interaction. The cuboidal arrangement is an attractor, provided that the spheres are brought sufficiently close to that configuration and are allowed to adjust their orientation towards the ground state, i.e., their mutual friction must not be too large. That is the reason why the arrangement shown by the left-hand side inset of Fig. 1 can be assembled without needing a tremendous amount of dexterity, and in that sense the arrangement can be considered as almost self-assembled.

While the hallmark of a dipole is its field decay with the third power of the distance, the combination of eight dipoles could be expected to form a 16-pole or hexadecapole with a decay according to the sixth power. Amazingly enough, it turns out that the ground state of a cuboidal cluster of eight dipoles shows a field decay with the seventh power. This is explained by the symmetry of the ensuing ground state which make all lower-order terms vanish.

II. EXPERIMENTAL RESULTS

For reaching the ground state of the cluster, the eight spheres should be allowed to rotate freely. For that purpose it is useful to provide a Teflon® spacer to reduce the friction of the spheres, as shown in the right-hand side inset of Fig. 1. Here, the eight neodymium magnets of diameter $d = (19 \pm 0.05)$ mm are arranged in a cuboidal configuration by the holes at the corners of the white Teflon® cube, and kept at an edge length $L = (39.5 \pm 0.05)$ mm by means of the nonmagnetic Teflon® spacer. A hole is drilled into that spacer along the face diagonal, the (1,1,0) direction of the cube. This allows us to move the Hall probe (the black tip) into the cuboid, down to its center, by means of a stepper motor, using 0.1-mm steps. We adjust the spheres within their continuous ground state to maximize the measured magnetic-flux density. This is achieved by manually turning just one sphere around the space diagonal as rotation axis; the other ones follow accordingly due to the magnetic interaction.

The measured magnetic-flux density along the (1,1,0) direction is shown in Fig. 1. It has a maximum at about $r = 28$ mm—where the Hall probe is closest to the spheres—and decays to zero both when approaching the center, and when increasing the distance from the cube. The solid line corresponds to a fit of the numerical superposition of the flux densities of eight accordingly arranged point dipoles, as given by (1) discussed below.

The most important feature of this cuboidal arrangement of dipoles is the unusually steep decrease of the magnetic-flux density outside the cube. To quantify this decrease, Fig. 2 shows the data from Fig. 1 in a logarithmic plot. It becomes obvious that the magnetic-flux density decays with the inverse seventh power of the distance. To characterize this magnetic cluster with an appropriate name, it must be recalled that the field of dipoles decays with the third power, quadrupoles with the fourth power, and so on. In that sense, the seventh power corresponds to a dotriacontapole.

The fact that the field is expected to be zero at that center of the arrangement is caused by the symmetry of the

*Stefan.Hartung@uni-bayreuth.de
†Johannes.Schoenke@oist.jp
‡Ingo.Rehberg@uni-bayreuth.de

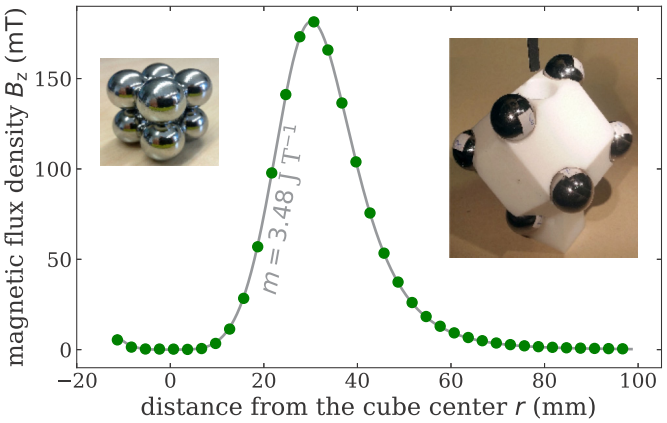

FIG. 1. Magnetic-flux density as measured along a straight path through the center of the cuboid. Only every 30th data point is shown. The solid line corresponds to the numerical superposition of the flux densities of eight accordingly arranged point dipoles with a magnetic moment $m = 3.48\ \mathrm{J\,T^{-1}}$. The left-hand side inset shows the principal cuboidal arrangement of the eight magnetic spheres, and the right-hand side inset a geometrically similar arrangement, but here with a white Teflon® spacer. The hole in that spacer allows us to take data inside the cuboid by means of the Hall probe, which is visible as the black part above the hole.

ground state. The measured deviations from that value can be attributed to geometrical and experimental imperfections: The dipole moments are not mathematically identical; they might not have reached their ground state due to the finite amount of friction, and the Hall probe can reach the center of the arrangement only with a mm precision.

The increase of the flux density with the fourth power is in agreement with the numerical evaluation of the ground state. According to that simulation, it even seems to be universal, i.e., independent of the direction along which the field is calculated. Compared to the seventh power of the decay this fourth power seems less exotic. It is somehow reminiscent of the field near the center of a Helmholtz pair of coils, where

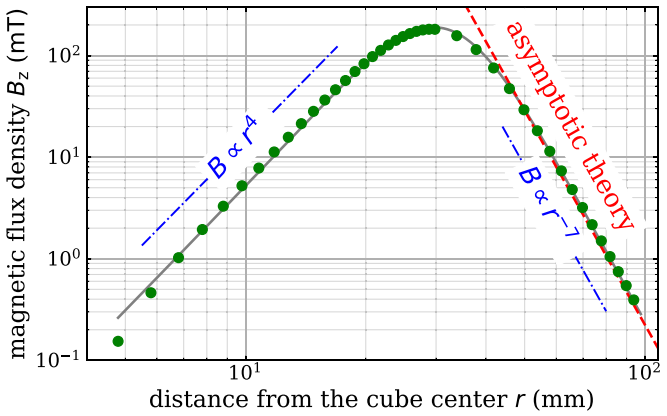

FIG. 2. The magnetic-flux density measured along a path starting from the center of the cuboid is represented by the circles. Only every tenth data point is shown at the left-hand side of the maximum, and every 40th data point at the right-hand side. The solid line is the same numerically obtained curve as in Fig. 1. The dash-dotted lines are for comparison with the expected asymptotic slopes. The dashed line depicts the analytical solution (7) for the far field.

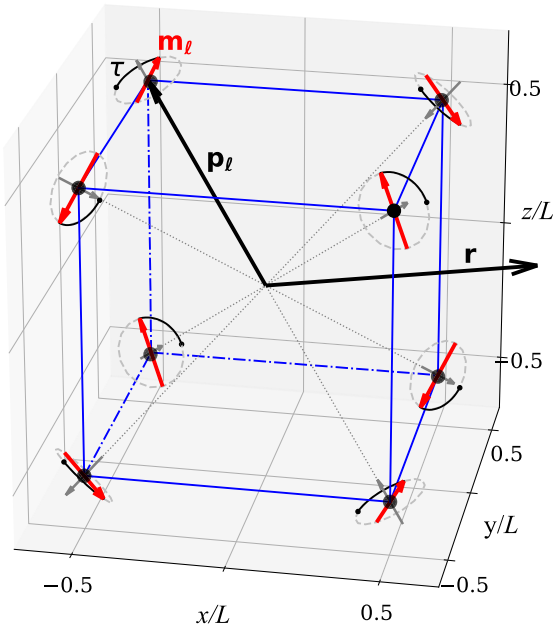

FIG. 3. The position $\mathbf{r}$ and the position vectors $\mathbf{p}_\ell$ of the dipole moments $\mathbf{m}_\ell$ are taken from the center of the cluster. The orientations of the dipoles in the continuous ground state are determined by the angle τ. The dipole configuration is sketched here for $\tau = 90°$, which corresponds to the largest negative value of B_z along the (1,1,0) direction.

the second-order terms vanish at a singular value of the coil distance.

III. THEORY

The scalar potential ϕ at position $\mathbf{r}$ for a distribution of N dipoles with position vectors $\mathbf{p}_\ell$ and dipole moments $\mathbf{m}_\ell$ (see Fig. 3) is given by

$$\phi = \sum_{\ell=1}^{N} \frac{\mathbf{m}_\ell \cdot (\mathbf{r} - \mathbf{p}_\ell)}{4\pi\,|\mathbf{r} - \mathbf{p}_\ell|^3}. \tag{1}$$

This equation is expected to describe the cluster field, because the individual spheres have a pure dipole field, in agreement with the theoretical expectation for homogeneously magnetized spheres [8] and our measurements presented in Appendix A. The numerical results of this equation correspond to the gray lines in Figs. 1 and 2.

To explain the behavior of the magnetic-flux density $\mathbf{B}$ in the far field, we perform a *multidipole* expansion, where the potential is expanded in a series for $|\mathbf{p}_\ell| \ll |\mathbf{r}|$,

$$\phi = \sum_{\nu=0}^{\infty} \frac{1}{\nu!} \sum_{\ell=1}^{N} \left.\frac{\partial^\nu \phi}{\partial \mathbf{p}_\ell^\nu}\right|_{\mathbf{p}_\ell=0} \cdot \underbrace{(\mathbf{p}_\ell \otimes \cdots \otimes \mathbf{p}_\ell)}_{\nu \text{ times}}.$$

As an example, the quadrupole (second term in the expansion) reads

$$\phi^{(2)} = \frac{1}{4\pi\,|\mathbf{r}|^5} \sum_{\ell=1}^{N} [3(\mathbf{m}_\ell \cdot \mathbf{r})\mathbf{r} - |\mathbf{r}|^2 \mathbf{m}_\ell] \cdot \mathbf{p}_\ell$$

$$= \frac{1}{4\pi\,|\mathbf{r}|^5} \sum_{\ell=1}^{N} [\underbrace{3\,\mathbf{m}_\ell \otimes \mathbf{p}_\ell - (\mathbf{m}_\ell \cdot \mathbf{p}_\ell)\mathbf{I}}_{\mathcal{M}^2}] \cdot (\mathbf{r} \otimes \mathbf{r}),$$

with the second-order unit tensor $\mathbf{I}$. The second-order tensor $\boldsymbol{\mathcal{M}}^2$ is the quadrupole moment. Using Cartesian coordinates $\mathbf{p}_\ell = (p_\ell^x, p_\ell^y, p_\ell^z)$, $\mathbf{m}_\ell = (m_\ell^x, m_\ell^y, m_\ell^z)$ and $\mathbf{r} = (x, y, z)$, we obtain

$$\phi^{(2)} = \frac{1}{4\pi|\mathbf{r}|^5}\Bigg[\underbrace{\sum_{\ell=1}^{N}\left(2p_\ell^x m_\ell^x - p_\ell^y m_\ell^y - p_\ell^z m_\ell^z\right)x^2}_{\mathcal{M}^2_{200}} + \underbrace{3\sum_{\ell=1}^{N}\left(p_\ell^x m_\ell^y + p_\ell^y m_\ell^x\right)xy}_{\mathcal{M}^2_{110}} + \cdots\Bigg].$$

$\mathcal{M}^2_{ijk}$ are the Cartesian components of the moment $\boldsymbol{\mathcal{M}}^2$ with $i + j + k = 2$. Using the moments, the potential can be written as

$$\phi = \sum_{\alpha=1}^{\infty}\phi^{(\alpha)} = \sum_{\alpha=1}^{\infty}\frac{1}{4\pi|\mathbf{r}|^{2\alpha+1}}\sum_{i+j+k=\alpha}\mathcal{M}^\alpha_{ijk}\,x^i y^j z^k. \quad (2)$$

The cube ground state [5,9] is a highly shielded structure. For a cube with edge length L and dipole moment magnitudes $|\mathbf{m}_\ell| = m$ we have

$$\begin{aligned}
&\text{(dipole)} && \mathcal{M}^1_{ijk} = 0,\\
&\text{(quadrupole)} && \mathcal{M}^2_{ijk} = 0,\\
&\text{(octopole)} && \mathcal{M}^3_{ijk} = 0, \quad (3)\\
&\text{(hexadecapole)} && \mathcal{M}^4_{ijk} = 0,\\
&\text{(dotriacontapole)} && \mathcal{M}^5_{311} = C\,\sin(\tau + \pi/3),
\end{aligned}$$

$$\mathcal{M}^5_{131} = C\,\sin(\tau + 5\pi/3), \quad (4)$$

$$\mathcal{M}^5_{113} = C\,\sin(\tau + 9\pi/3), \quad (5)$$

where $\tau = 0\ldots 2\pi$ is the current phase angle [5,9] of the continuous ground state as indicated in Fig. 3 and Appendix B, and $C = 105\sqrt{3/2}\,L^4 m$. There are restrictions for the cube moments following from the symmetries of the ground state [5]. The potential ϕ has to be zero in the three planes, $x = 0$, $y = 0$, $z = 0$, as well as on the four volume diagonals, $|x| = |y| = |z|$. Together with (2) this leads to conditions for the nonzero moments $\mathcal{M}^\alpha_{ijk}$:

$$i, j, k \text{ positive, odd} \Rightarrow \alpha \text{ odd, and } \sum_{i+j+k=\alpha}\mathcal{M}^\alpha_{ijk} = 0.$$

This explains why the first nonzero moments appear in the dotriacontapole,

$$\phi^{(5)} = \frac{\mathcal{M}^5_{311}\,x^3yz + \mathcal{M}^5_{131}\,xy^3z + \mathcal{M}^5_{113}\,xyz^3}{4\pi|\mathbf{r}|^{11}}. \quad (6)$$

The magnetic-flux density is related to the potential through $\mathbf{B} = -\mu_0\partial\phi/\partial\mathbf{r}$. We parametrize the measurement along the direction (1,1,0) with the radius parameter s through $(x, y, z) = (s, s, 0)/\sqrt{2}$ and obtain the following expression for the z component of the magnetic-flux density from (3)–(6):

$$B_z(s,\tau) = -\mu_0\frac{\partial\phi}{\partial z}\bigg|_{x=y=s/\sqrt{2},\,z=0} = -\frac{105\sqrt{3/2}\,\mu_0 L^4 m\,\sin\tau}{16\pi s^7} + \mathcal{O}\left(\frac{1}{s^9}\right). \quad (7)$$

The next order decays with $|\mathbf{B}| \propto 1/s^9$ because all moments with even α are zero.

Equation (7) is displayed in Fig. 2 by the dashed line. The solid lines in Figs. 1 and 2 are obtained numerically from the exact (1), with $\tau = 90^\circ$ taken as the phase angle of the continuous ground state (see Appendix C). It is amazing that this asymptotic prediction reaches the exact solution already at a distance of about 50 mm, which can be considered as sheer luck from an experimental point of view, because the field is hardly detectable for our equipment at distances larger than 100 mm. For the measurements shown there, the angle τ was adjusted manually to obtain the largest signal of the Hall probe to achieve an optimal signal-to-noise ratio. This corresponds either to $\tau = 90^\circ$ or to $\tau = 270^\circ$.

Note that the shape of the $B(r)$ curve shown in Figs. 1 and 2 is not universal, it rather depends on the direction of the line along which the flux density is measured. The $1/r^7$ decay, however, is a universal feature for all directions in the far-field limit, $|\mathbf{p}_\ell| \ll |\mathbf{r}|$.

IV. CONCLUSION AND OUTLOOK

In summary, we have demonstrated that eight spherical permanent magnets assemble into a configuration which behaves like a dotriacontapole. This can be explained by a model based on pure dipole-dipole interaction. This model is based on symmetry considerations which are an idealization of the experimental situation. The measurements make it clear that the conclusions drawn from the idealization are robust against (small) distortions, in particular the decay of the magnetic-flux density with $1/r^7$—a hallmark for a highly shielded structure—survives.

This finding implies that storing strong magnets in a cubic packing might be the optimal way for suppressing their field in the outer surrounding. Moreover, the extremely steep field decay has remarkable consequences for the clustering dynamics: If two dipole spheres, initially separated by say ten diameters, needed one second to collide due to their attractive force, for dotriacontapoles of comparable strength, this process would take more than one year (see Appendix B). Thus, dipoles which manage to arrange themselves in this configuration are fairly robust against further clustering. This argument is scale invariant. It applies to macroscopic granules in the early stages of planet formation [10], but could also shed some light on the self-assembly dynamics of colloidal nanomagnets [3,4] used for medical applications [11].

The plastic spheres shown in Fig. 4 demonstrate an attempt to build a handful of such dotriacontapoles with the help of a three-dimensional (3D) printer. Each sphere contains eight magnetic dipoles in a cubic arrangement. This is provided by three perpendicular walls inside these spheres, indicated in the left-hand side inset, and eight holes along the space

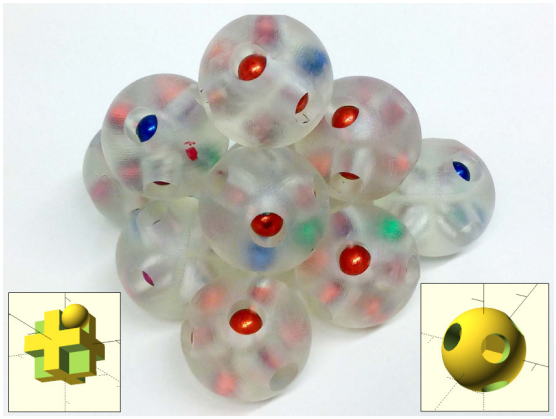

FIG. 4. A cluster of 3D-printed dotriacontapoles. The inner part of these spheres contains three perpendicular walls as indicated by the left-hand side inset. The colored magnetic spheres of 5 mm diameter are placed inside these plastic spheres by the eight holes along the space diagonals, as indicated by the right-hand side inset.

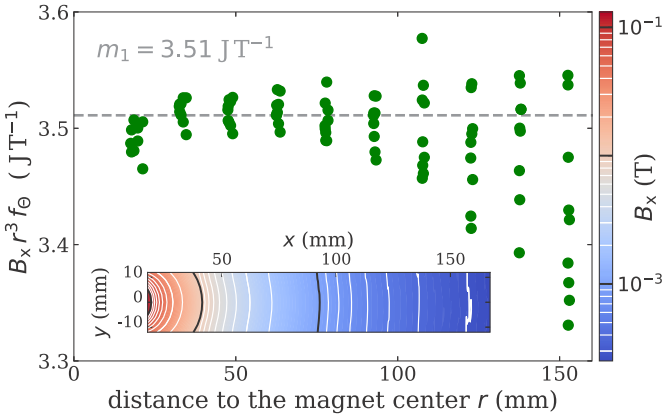

FIG. 5. The inset shows $B_x(x, y)$ measured in a plane, color coded in red for strong fields to blue for weak ones. The direction of the x coordinate is chosen to be parallel to the dipole moment **m** and forms a horizontal plane with the perpendicular coordinate y. An estimator for the magnetic moment is obtained from these data with (A2). The result is displayed as a function of r by the circles. The dashed line represents the mean value m_1 of these data.

diagonals, as indicated by the right-hand side inset. These plastic spheres should thus interact with an extremely short-ranged interaction force, which should asymptotically decay with the inverse 12th power of the mutual distance—provided that the magnetic dipoles inside a sphere are in their ground state. Measuring such a short-range interaction between dipole clusters provides a challenge left to be faced in future work.

ACKNOWLEDGMENTS

It is a pleasure to thank F. Braun, K. Huang, R. Richter, W. Schöpf, and A. Weber for valuable hints and discussions. This work has been supported by the Deutsche Forschungsgemeinschaft (DFG) - Project No. 389197450.

APPENDIX A: MAGNETIC SPHERES AS DIPOLES

The magnetic spheres (MK-19-C from magnets4you GmbH) have a diameter of $d = (19 \pm 0.05)$ mm. For explaining the experimental findings with a theoretical model based on pure dipole-dipole interaction, it is crucial to demonstrate that these spheres can be described as magnetically hard point dipoles. Thus, we have measured the axial component of the magnetic-flux density B_x of a single sphere along the x direction in a 170-mm × 20-mm xy plane, as shown in the inset of Fig. 5. The flux density is measured by a Hall probe (HU-ST1-184605, MAGNET-PHYSIK Dr. Steingroever GmbH). The 3D positioning of this probe is done with a stepper motor (High-Z S-400T, with Zero-3 controller from CNC-STEP), the interface (CNCPod) is programmable in G-Code, DIN/ISO 66025. A single-board microcontroller (Leonardo, Arduino) is additionally used for interfacing it to a PC.

To emphasize deviations from the point dipole approximation, and to extract the underlying magnetic moment, we make use of the theoretically expected flux density of a point dipole [8],

$$B_x = \frac{\mu_0}{4\pi} \frac{m\,(3\cos^2\Theta - 1)}{r^3}, \tag{A1}$$

with $\Theta = \arctan(y/x)$, $r = \sqrt{x^2 + y^2}$ measuring the angle between the dipole moment and the position vector, and the magnetic constant μ_0. With the shorthand notation $\frac{4\pi}{\mu_0(3\cos^2\Theta - 1)} = f_\Theta$, this provides the magnitude of the magnetic moment,

$$m = B_x r^3 f_\Theta. \tag{A2}$$

The resulting m as a function of the measured value of $B_x(x, y)$ is plotted in Fig. 5 as a function of the distance of the Hall probe from the center of the sphere. The increasing

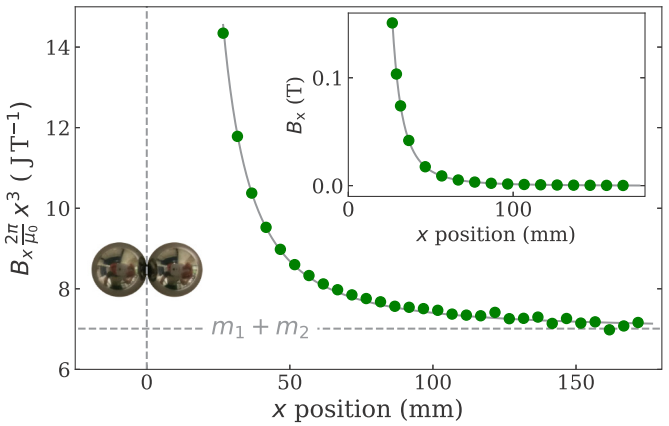

FIG. 6. Data obtained from the measurements of the magnetic-flux density B_x of two spheres in contact. The raw data are shown in the inset, and the solid line shows the calculated superposition of two dipole fields. B_x scaled with $x^3 2\pi/\mu_0$ is shown in the larger plot. The horizontal dashed line represents the sum of the magnetic moments of the isolated spheres. The dashed vertical line represents the origin at the contact point of the spheres.

scatter at larger distances r is caused by the fast decay of the magnetic-flux density. Based on these data, it seems safe to conclude that the point dipole approximation for the magnetic-flux density of the sphere is reliable within $\pm 2\,\%$. The mean value is $(3.51 \pm 0.18)\,\mathrm{J\,T^{-1}}$, which is well within the $(3.54 \pm 0.11)\,\mathrm{J\,T^{-1}}$ claimed by the manufacturer. We have measured all eight dipoles used in the experiments described here in a similar way, they differ by an amount of $\pm 3\%$.

To measure the mutual influence of such magnetic spheres, we brought them in direct contact as shown in the left-hand side inset of Fig. 6. The measured flux density along the axis of the resulting two-dipole cluster is shown as the right-hand side inset in Fig. 6. The position of the Hall probe is measured as the distance from the center between the spheres. The data reveal roughly the typical $1/x^3$ descent of a dipole, but deviations from that scaling are hard to judge from this inset plot. To get a better resolution for the deviations from the overall $1/x^3$ decay, the data were multiplied with x^3. After scaling with $2\pi/\mu_0$ one gets an estimate for the magnetic moment, which is displayed on the vertical axis of Fig. 6. These scaled data decay monotonically with the position x and reach the value of the sum of the two magnetic moments asymptotically, which is indicated by the dashed line. The solid line is the theoretical estimation, based on the superposition of the fields of the individually measured moments $m_1 = 3.51\,\mathrm{J\,T^{-1}}$ and $m_2 = 3.50\,\mathrm{J\,T^{-1}}$, with their mutual distance given by the diameter of the spheres. The good agreement between this curve and the data indicates that the magnets are hard ones: Their magnetic moment stays constant even under the influence of the immediately adjacent other magnet, at least within the experimental resolution on a percentage level.

APPENDIX B: DIPOLE ORIENTATION IN THE CUBE GROUND STATE

The dipole orientation within the ground state of the cuboidal cluster can be parametrized by a single parameter, namely the phase angle $\tau = 0^\circ \ldots 360^\circ$ [5,9]. The configuration for the angle $\tau = 90^\circ$ is illustrated in Fig. 3. The source code of a Python script animating this state together with the corresponding fields for adjustable values of τ is available [12]. The exact positions and orientations of the dipoles with respect to τ are provided by Table I.

TABLE I. Description of $\mathbf{p}_i$ and $\mathbf{m}_i$ in the cube ground state.

i	$\mathbf{p}_i$	$\mathbf{m}_i \cdot \sqrt{3/2}/m$
1	$\begin{pmatrix} 0.5 \\ 0.5 \\ 0.5 \end{pmatrix}$	$\begin{pmatrix} -\sin(\tau - 240^\circ) \\ -\sin(\tau - 120^\circ) \\ -\sin(\tau) \end{pmatrix}$
2	$\begin{pmatrix} 0.5 \\ 0.5 \\ -0.5 \end{pmatrix}$	$\begin{pmatrix} +\sin(\tau - 240^\circ) \\ +\sin(\tau - 120^\circ) \\ -\sin(\tau) \end{pmatrix}$
3	$\begin{pmatrix} 0.5 \\ -0.5 \\ 0.5 \end{pmatrix}$	$\begin{pmatrix} +\sin(\tau - 240^\circ) \\ -\sin(\tau - 120^\circ) \\ +\sin(\tau) \end{pmatrix}$
4	$\begin{pmatrix} 0.5 \\ -0.5 \\ -0.5 \end{pmatrix}$	$\begin{pmatrix} -\sin(\tau - 240^\circ) \\ +\sin(\tau - 120^\circ) \\ +\sin(\tau) \end{pmatrix}$
5	$\begin{pmatrix} -0.5 \\ 0.5 \\ 0.5 \end{pmatrix}$	$\begin{pmatrix} -\sin(\tau - 240^\circ) \\ +\sin(\tau - 120^\circ) \\ +\sin(\tau) \end{pmatrix}$
6	$\begin{pmatrix} -0.5 \\ 0.5 \\ -0.5 \end{pmatrix}$	$\begin{pmatrix} +\sin(\tau - 240^\circ) \\ -\sin(\tau - 120^\circ) \\ +\sin(\tau) \end{pmatrix}$
7	$\begin{pmatrix} -0.5 \\ -0.5 \\ 0.5 \end{pmatrix}$	$\begin{pmatrix} +\sin(\tau - 240^\circ) \\ +\sin(\tau - 120^\circ) \\ -\sin(\tau) \end{pmatrix}$
8	$\begin{pmatrix} -0.5 \\ -0.5 \\ -0.5 \end{pmatrix}$	$\begin{pmatrix} -\sin(\tau - 240^\circ) \\ -\sin(\tau - 120^\circ) \\ -\sin(\tau) \end{pmatrix}$

APPENDIX C: ASSEMBLY TIME FOR DIPOLES VERSUS THAT FOR DOTRIACONTAPOLES

The time T_m for two multipoles of diameter d starting at a distance of $10d$ to come into contact under the influence of their mutual attraction—a characteristic time for the dynamics of the self-assembly of magnetic clusters [3,4]—is obtained by integrating over their inverse velocity. When assuming that these particles are suspended in a viscous fluid, that velocity is proportional to the attractive force (Stokes's law). T_2 denotes the pair of dipoles, T_{32} denotes the pair of dotriacontapoles. The attracting force of these multipole pairs is assumed to be the same when they are in contact at the distance of $1d$,

$$\frac{T_{32}}{T_2} = \frac{\int_{5d}^{d/2} \frac{1}{v_{32}}\,dr}{\int_{5d}^{d/2} \frac{1}{v_2}\,dr} \overset{v \propto F}{=} \frac{\int_{5d}^{d/2} -\left(\frac{2r}{d}\right)^{12} dr}{\int_{5d}^{d/2} -\left(\frac{2r}{d}\right)^{4} dr} = \frac{5}{13}\,\frac{10^{13}-1}{10^5-1} \approx 0.4 \times 10^8.$$

This ratio turns, e.g., $1s$ for a dipole pair into $1a$ for the corresponding pair of dotriacontapoles: They are fairly robust against further clustering.

[1] A. D. Buckingham, Q. Rev., Chem. Soc. **13**, 183 (1959).

[2] D. Stamou, C. Duschl, and D. Johannsmann, Phys. Rev. E **62**, 5263 (2000).

[3] S. Mehdizadeh Taheri, M. Michaelis, T. Friedrich, B. Förster, M. Drechsler, F. M. Römer, P. Bösecke, T. Narayanan, B. Weber, I. Rehberg, S. Rosenfeldt, and S. Förster, Proc. Natl. Acad. Sci. USA **112**, 14484 (2015).

[4] S. Rosenfeldt, S. Förster, T. Friedrich, I. Rehberg, and B. Weber, in *Novel Magnetic Nanostructures*, Advanced Nanomaterials, edited by N. Domracheva, M. Caporali, and

E. Rentschler (Elsevier, Amsterdam, Netherlands, 2018), pp. 165–189.

[5] J. Schönke, T. M. Schneider, and I. Rehberg, Phys. Rev. B **91**, 020410 (2015).

[6] S. Borgers, S. Völkel, W. Schöpf, and I. Rehberg, Am. J. Phys. **86**, 460 (2018).

[7] P. I. Belobrov, R. S. Gekht, and V. A. Ignatchenko, Zh. Eksp. Teor. Fiz. **84**, 1097 (1983) [Sov. Phys. JETP **57**, 636 (1983)].

[8] J. D. Jackson, *Classical Electrodynamics*, 3rd ed. (Wiley, New York, 1999).

[9] J. Schönke, An interactive gallery of the dipole cube, http://ecps.ds.mpg.de/people/cube_gallery/cube_gallery.html (2015).

[10] J. Blum, Adv. Phys. **55**, 881 (2006).

[11] T. M. Buzug, J. Borgert, T. Knopp, S. Biederer, T. F. Sattel, M. Erbe, and K. Lüdtke-Buzug, *Magnetic Nanoparticles* (World Scientific, Singapore, 2010).

[12] I. Rehberg, Ground state of the dipole cube, http://www.staff.uni-bayreuth.de/~bt180034/dotriacontapole.html (2018).

Acknowledgments

This work would not have been possible without the indispensable support from my supervisors, colleagues and family. Especially, I thank

- Prof. Dr. Ingo Rehberg for the kind admission to EPV, his highly valuable comments and constructive criticism in the regular meetings, as well as all academic guidance.
- Prof. Dr. Kai Huang for introducing me to the physics of granular matter, giving me the opportunity to conduct research in this field, and enabling me to present the results at various international conferences and at the Chinese Academy of Sciences.
- Prof. Dr. Thorsten Pöschel and Dr. Matthias Schröter for pointing me to Set Voronoi tessellations, and Dr. Simon Weis for discussing the suitability of the Pomelo software.
- Dr. Thomas John for calling my attention to kernel density estimators and Dr. Zdravko Botev for his advise on how to apply state of the art techniques in practice.
- Dr. Wolfgang Schöpf, PD Dr. Reinhard Richter, and all students at EPV for their valuable feedback in the weekly seminar.
- Stephan Messlinger for sharing his unparalleled knowledge on electronics in the measurement coffee seminars.
- Stefan Hartung for his friendship in the lab and his encouragements during writing.
- all staff of the EPV chair for their constant support, especially Christine Linser, Klaus Oetter, and Andreas Forstner for their great help on any administrative, mechanical or electronic problems.
- my parents Angela and Werner and my brother Josia for their relentless support.
- my wife Alexandra for her unconditional love, assurance and patience.

Last but not least, I want to thank the creator of this fascinating world for the opportunity to explore it, his son for the confidence extending beyond and his spirit for all insight.

Eidesstattliche Versicherung

Hiermit versichere ich an Eides statt, dass ich die vorliegende Arbeit selbstständig verfasst und keine anderen als die von mir angegebenen Quellen und Hilfsmittel verwendet habe.

Weiterhin erkläre ich, dass ich die Hilfe von gewerblichen Promotionsberatern bzw. -vermittlern oder ähnlichen Dienstleistern weder bisher in Anspruch genommen habe, noch künftig in Anspruch nehmen werde.

Zusätzlich erkläre ich hiermit, dass ich keinerlei frühere Promotionsversuche unternommen habe.

Bayreuth, den 7. September 2021 .....

Simeon Völkel